INTERNAL HEAT TRANSFER AND EXTERNAL EFFECTIVENESS MEASUREMENTS FOR A NOVEL TURBINE BLADE COOLING DESIGN

Erin N. Elder

Thesis submitted to the Faculty
of the Virginia Polytechnic Institute and State University
in partial fulfillment of the requirements for the degree of

Master of Science
in
Mechanical Engineering

Dr. K.A. Thole, Chair
Dr. W.F. Ng
Dr. C.L. Dancey

May 5, 2005
Blacksburg, VA

Keywords: gas turbines, film cooling, internal cooling, microcircuit, heat transfer augmentation, friction factor augmentation

Internal Heat Transfer and External Effectiveness Measurements for a Novel Turbine Blade Cooling Design

Erin N. Elder

Abstract

Efficiency and power output of gas turbines improve with an increase in turbine inlet temperatures, and blade designers continually seek out new methods of increasing these temperatures. Increases in turbine inlet temperatures are achieved by utilizing a combination of internal convective cooling and external film-cooling. This study will evaluate several novel cooling schemes for turbine airfoils, called microcircuits. Microcircuits are placed inside the turbine blade wall, and the features turbulate the air and increase heat transfer surface area, thereby augmenting convective cooling. The coolant flow then exits internal cooling passages to the external side of the blade. Here the coolant forms a protective layer along the external surface of the blade to protect the blade from the heated mainstream flow.

In the current study, a low-speed large-scale wind tunnel facility was developed to measure internal heat transfer coefficients and external adiabatic effectiveness, using thermal liquid crystallography and infrared thermography. This test facility is unique in that it can be used to test the effects of internal cooling features on external film cooling. Results show that the highest augmentations in internal heat transfer were seen at the lowest Reynolds numbers. Internal features affected the shapes of external film-cooling contours, but the magnitudes of the spanwise averaged values did not change significantly with changes in internal geometry.

Acknowledgements

My time at Virginia Tech has taught me so much more than Mechanical Engineering. This has been a lesson in life with many struggles and many triumphs. I think the most important lesson I have learned is one of resolve and determination. I have grown during this time and would like to thank the people who encouraged me and supported me, as I would not have made it through without them.

I want to thank my family for being the best family that a girl could have. Mom and Dad, I have led an incredibly blessed life. You have given so much to make me into the person that I am today, and I want to thank you for that. Allison you are such a wonderful sister, and I am so lucky to have such a good friend as a part of my family.

I have enjoyed my time here in Blacksburg because of all the friends that I have made. Sarah, it has been wonderful to have such a great friend to come home to. Sharon, your sense of humor has kept me laughing even when I did not want to. XingXi, I have enjoyed every moment of getting to know you, what a blessing that you were the first person I met in this town! I would like to thank Amber, Ben, Jenni, Kate, and Omar for making my time here so much fun. I would also like to mention all of the fellow members of VTExCCL, including Angela, Scott, Nick, Joe, Sundar, Will, Mike, Scott B., Eric, and Paul who have made the daily work so much more enjoyable. I would especially like to thank Jeff Prausa, my collaborator on the microcircuit work. Thank you for your patience as I learned to build starting from zero. I thoroughly enjoyed working with you.

My advisor, Dr. Karen Thole has provided guidance and encouragement throughout my time here. From setting aside time to help me out when I was struggling in classes, or giving a hug when I really needed it, you have become a wonderful friend, and I appreciate all that you have done.

I would like to thank everyone back at Georgia Tech. Go Jackets!

I would also like to acknowledge Pratt and Whitney and the Virginia Space Grant Consortium for funding my work on this project.

Contents

Nomenclature

A	= area
B	= blue
d	= streamwise slot length, standard pin fin diameter
D_h	= hydraulic diameter;
f	= friction factor
F_M	= PinFin predicted Friction Multiplier
G	= green
h	= heat transfer coefficient
I	= momentum flux ratio;
k	= thermal conductivity
L	= fin efficiency channel height
M	= mass flux ratio; blowing ratio;
NHFR	= net heat flux reduction;
Nu	= Nusselt Number;
P	= pressure or spanwise slot spacing
p	= perimeter
q''	= heat flux
Q	= heat transfer
R	= red
Re	= Reynolds Number;
s	= cooling feature geometry normalization factor
s_n	= streamwise pin fin spacing
s_p	= pitchwise pin fin spacing
t	= thickness
T	= temperature
TC	= thermocouple
u	= uncertainty
U	= Velocity

w	= spanwise slot width
X	= streamwise distance
Y	= spanwise distance
Z	= pitchwise distance

Greek:

δ	= partial derivative
ΔP	= static pressure differential
ε	= surface emissivity
η	= adiabatic effectiveness;
η_f	= fin efficiency;
η_{GT}	= Brayton Cycle gas turbine efficiency;
Ω	= electrical resistance in Ohms
ρ	= density
σ	= Boltzman Constant;

Subscripts:

$\overline{\text{variable}}$	= spanwise averaged value
$\overline{\overline{\text{variable}}}$	= area averaged value
o, ∞	= upstream with no blowing
∞	= mainstream
∞,corrected	= mainstream adjusted for boundary layer cooling
1	= engine air inlet
2	= compressor exit
3	= turbine inlet
4	= turbine exit
avg	= average
AW	= adiabatic wall

bg	= background
bulk	= unobstructed channel
c	= coolant
conduction	= due to conduction heat transfer
const	= constant
convection	= due to convection heat transfer
cs	= cross section
dynamic	= due to fluid motion
e	= effective
exit	= evaluated at the exit plane
f	= fin
freeconv	= natural convection
heater	= describing the inconel strip heater
inlet	= inlet location
j	= jet
line	= along a specified line
m	= mean
max	= maximum possible value
MC	= microcircuit
o	= unobstructed baseline (with film cooling for NHFR)
PW	= Pratt & Whitney
removed	= taken away
static	= fluid at rest
surf	= surface
surr	= ambient
total	= sum of all portions
TS	= mainstream test section
VT	= Virginia Tech (current study)
w	= wall

List of Tables

List of Figures

Chapter 1

Introduction

Gas turbine engines are commonly used in aircraft engines and power generation. Other applications include microturbines used to provide power and heat to individual buildings and to power submarines.

In aircraft engines thrust is the force used to propel the airplanes. The working fluid, air, is accelerated by the system. By Newton's Third Law, this acceleration causes a force, which results in forward motion. The amount of mass flow through the system and the exit velocity of the air determine the amount of thrust. Gas turbine engines power most modern passenger and military aircraft. A wide range of engines exists to accommodate the specifications of each airplane. Military aircraft often require high acceleration while this capability is not necessary in commercial airliners. These commercial airliners must have a high weight capacity and the capability to travel long distances at high speeds.

Gas turbine engines run according to the theoretical cycle called the Brayton Cycle. In the Brayton Cycle compressor work is extracted in the form of shaft work. Combustion increases the amount of energy available from the working fluid. In aircraft engines, some of the work extracted in the turbine is used to turn the compressor, but the useful work is in the form of thrust to provide forward momentum for the airplane.

Efficiency and power output of gas turbines improve with an increase in turbine rotor inlet temperatures. Equation 1.1 presents the efficiency of the Brayton Cycle for a gas turbine engine.

$$\eta_{GT} = 1 - \frac{T_4 - T_1}{T_3 - T_2} \tag{1.1}$$

where T_1 is the temperature of the air entering the engine, T_2 is the temperature of the air exiting the compressor, T_3 is the turbine inlet temperature, and T_4 is the temperature of the gas exiting the turbine. One method of increasing the efficiency of the engine is to

increase T_3, the turbine inlet temperature. Engine designers are pushing the envelope when it comes to increasing turbine inlet temperatures. Thermal barrier coatings and cooling methods have allowed for these temperature increases, this document will discuss next-generation cooling methods for turbine blades.

Innovative cooling methods allow blade designers to raise turbine inlet temperatures to levels higher than the melting temperatures of the blade material as shown in Figure 1-1. Also seen in Figure 1-1, it is critical to fully characterize the temperatures in an engine because an increase in blade metal temperature drastically reduces the part life. An increase in the metal temperature of around 15°C will halve the part life. If a part deteriorates to the point that the engine must be overhauled, this equates to a revenue loss of around one million dollars for a commercial airline.

The goal of engine designers is to achieve increased turbine inlet temperatures without significant blade deterioration. Internal convective cooling and external film-cooling are two methods that have been successful in protecting the blade material as it is exposed to high mainstream temperatures. Internal convective cooling, flowing air through the internal passages of the blade, can be further augmented by the use of pin fin arrays. These pin fins serve to turbulate the air and to increase the heat transfer surface area thereby augmenting convective cooling. The coolant flow exits internal cooling passages to the external side of the blade and forms a protective layer along the external surface of the blade further cooling the blade.

Figure 1-2 is a schematic of coolant entering the coolant supply, flowing through the convection cooling channels, exiting the blade through cooling holes, and finally flowing along the outside surface of the blade to protect the surface from the hot mainstream flow. Hot mainstream flow is on the order of 1300°C at the turbine inlet in today's jet engine designs [Gritsch et al., 2001].

1.1 Internal Convective Cooling with Microcircuits

Internal cooling is essentially flowing air along internal side of the blade surface to remove heat. The equation below is used to calculate the heat transfer coefficient in the channel

$$Q = h \cdot A(T_W - T_C) \tag{1.2}$$

where Q is the heat removed from the channel wall, A is the area of the channel wall, T_w is the wall temperature, and T_C is the coolant temperature, and h is the heat transfer coefficient. Heat transfer coefficient is dependant on both the channel geometry and flow characteristics of the coolant.

This increase in heat transfer is achieved using pin fin configurations, dimples along the enwalls of the channels, or ribbed turbulators. These internal channel features promote turbulence and increase the heat transfer surface area thereby increasing the heat transfer coefficients in internal cooling channels. These cooling configurations are effective, and Pratt and Whitney, the sponsor of this project, is currently examining more advanced cooling methods based on similar cooling concepts.

These more advanced cooling configurations, called microcircuits, are designed for placement in the thin blade wall as shown in Figure 1-3. The implementation of passages internal to the blade wall has structural implications. To guarantee structural soundness of these hollow walls, it is necessary that the amount of wall surface supported by pinfin-like features cover at least 50% of the wall surface. The flow blockage caused by the presence of the features has severe implications on pressure losses. In standard pin fin configurations, pin fins are generally spaced so that the optimal heat transfer benefits are gained for the smallest possible pressure losses.

Based on CFD testing completed by Pratt and Whitney, the microcircuit designs were arranged as follows: an impingement cooling region was followed by a pin fin bank, which was followed by a feature that constricts the flow into paths with small metering areas. The flow leaving these constricted areas was then diffused as it approached the slot exit. The directionality of the jet-like flow diffusing from the small metering areas dictated the shape and extent of cooling exhibited on the external wall in the form of film-cooling.

1.2 External Film Cooling

External cooling is a means of cooling the surface by injecting a layer of coolant along the surface. This coolant flow remains close to the surface and separates the heated mainstream flow from the wall. The film cooling adiabatic effectiveness, eta, is shown below

$$\eta_{AW} = \frac{T_\infty - T_{AW}}{T_\infty - T_C} \tag{1.3}$$

where T_∞ is the mainstream gas temperature, T_{AW} is the adiabatic wall or the temperature of the wall with no heat transfer through the wall surface, and T_C is the coolant temperature. In values of eta close to one T_{AW} is approaching T_C, meaning that the coolant is successfully lowering the wall temperature. In values of eta close to zero, T_{AW} is near T_∞ meaning that the wall temperature remains similar to the mainstream temperature. In this case the coolant is not effectively cooling the wall.

1.3 Research Objectives

The need existed for a facility to test advanced cooling designs of the above described microcircuits. A novel low-speed large-scale wind tunnel facility was developed with the capability to measure internal heat transfer coefficients, using thermal liquid crystallography, and external adiabatic effectiveness, using infrared thermography. The test facility has been used to characterize several proprietary cooling configurations, and is currently in use for the testing of public pin fin designs.

The heat transfer coefficient contours and adiabatic effectiveness contours were collected for characterization of the internal and external cooling in a blade. Contours are useful for indicating “hot-spots” on the blade, as obtaining uniform surface temperatures is necessary for minimizing the thermal stresses experienced by a blade. The contour values can be non-dimensionalized and scaled to heated engine conditions to provide further insight for blade design.

The uniqueness of this experimentation lies in the fact that the effect of internal cooling features on external slot flow film-cooling has not been previously examined. The internal and external flow paths are coupled in this test facility such that the effects of internal features on external flow can be examined.

The large scale of the test facility was selected because large scale testing allows experimenters to measure temperature contours at a higher resolution and allows for testing at temperatures and pressures significantly lower than those measured in actual turbines. The scaling factor of the current test facility, 25 times the microcircuit scale, was chosen to allow for measurement of both internal heat transfer and external film-cooling efficiency using compressed air supply capabilities.

The friction factor values were also measured in this test to determine whether the cooling effects observed in the microcircuit are justifiable due to the high pressure loss penalties incurred due to the extensive flow blockage.

This document will discuss the design and construction of a novel wind tunnel test facility as well as the testing of three microcircuit designs. Chapter 2 contains a review of literature relevant to internal heat transfer, friction factors, and external film cooling. Chapter 3 provides a detailed description of the test facility as well as benchmark data to validate the test facility. Chapter 4 details the methods of data analysis. Chapter 5 documents the experimental results, and provides a comparative analysis of the three microcircuit designs. Conclusions and recommendation for further work are presented in Chapter 6.

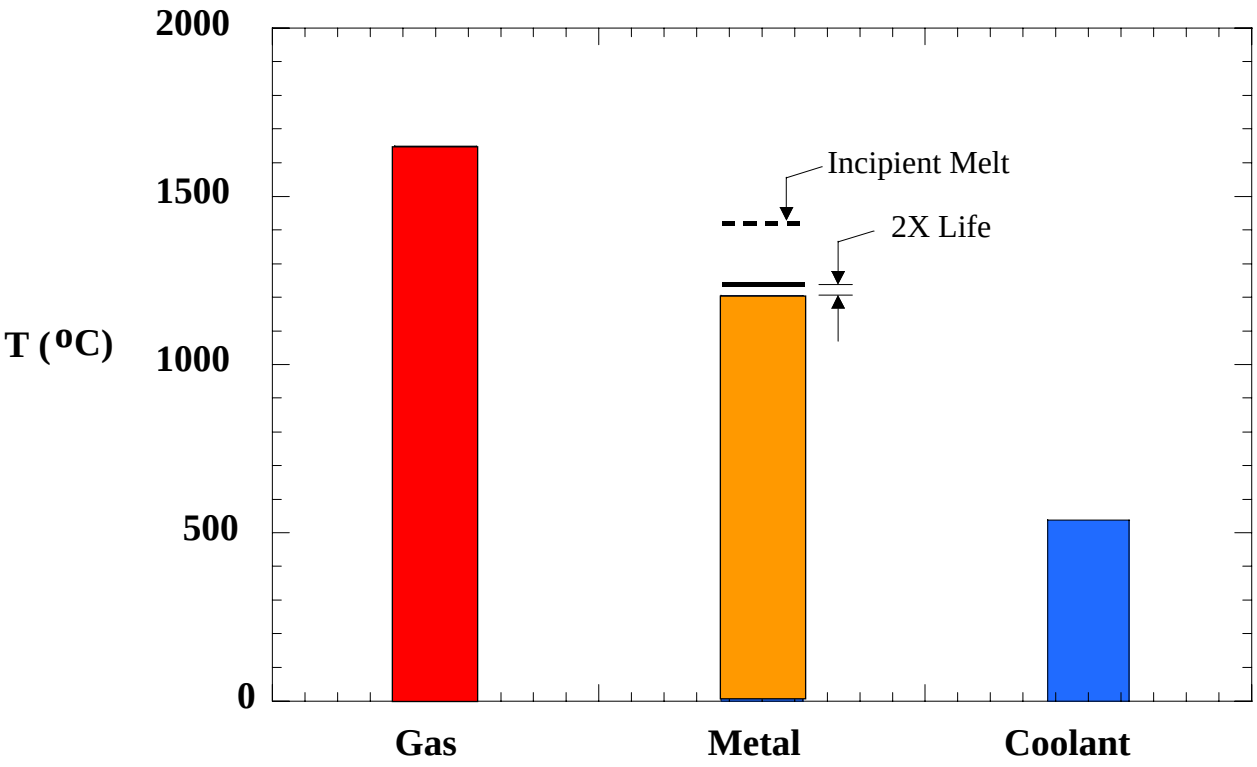

Figure 1-1. Comparison of gas and metal temperatures at the first stage turbine blade of a gas turbine engine.

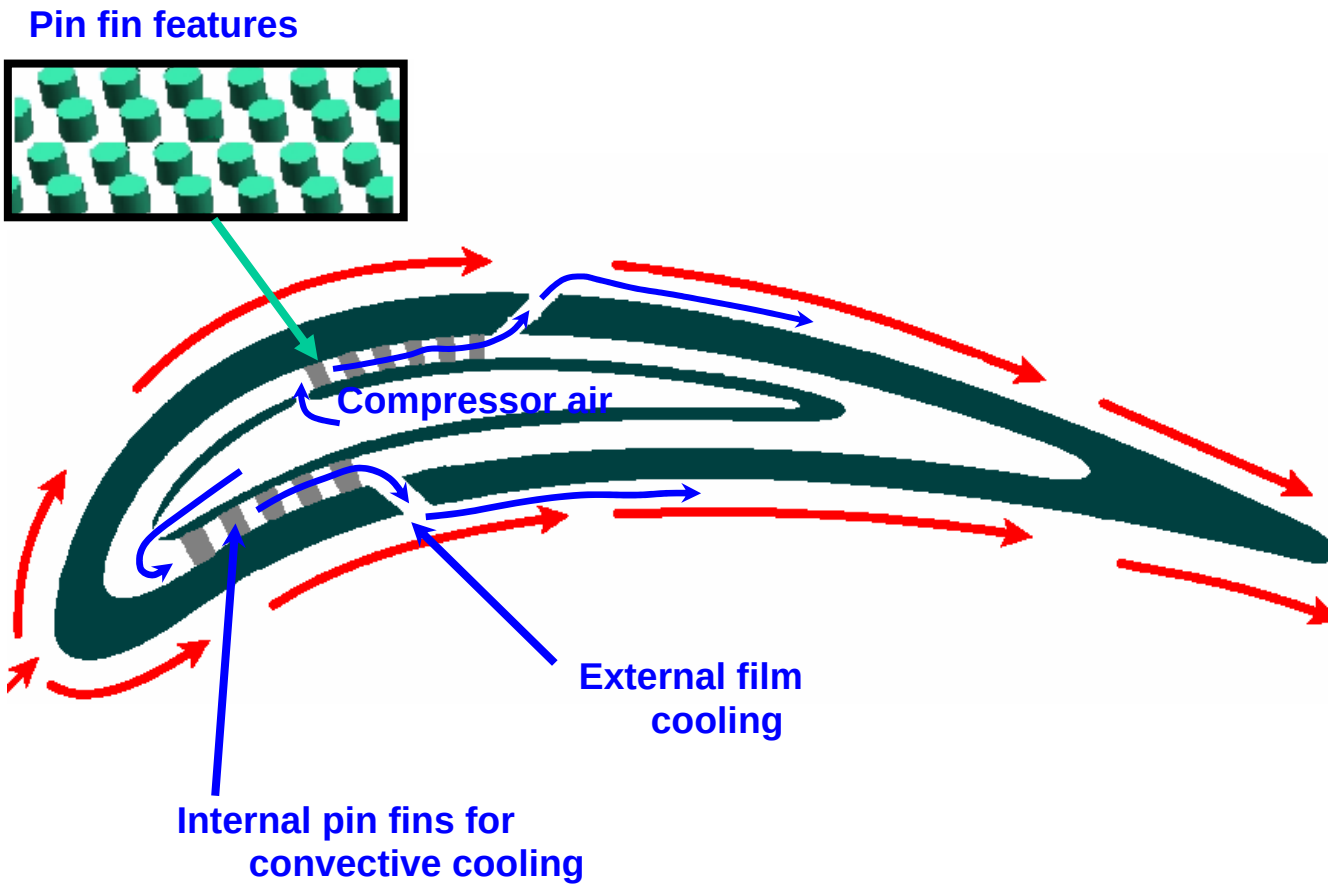

Figure 1-2. Schematic of combined internal and external blade cooling in a blade cooled using a pin fin bank.

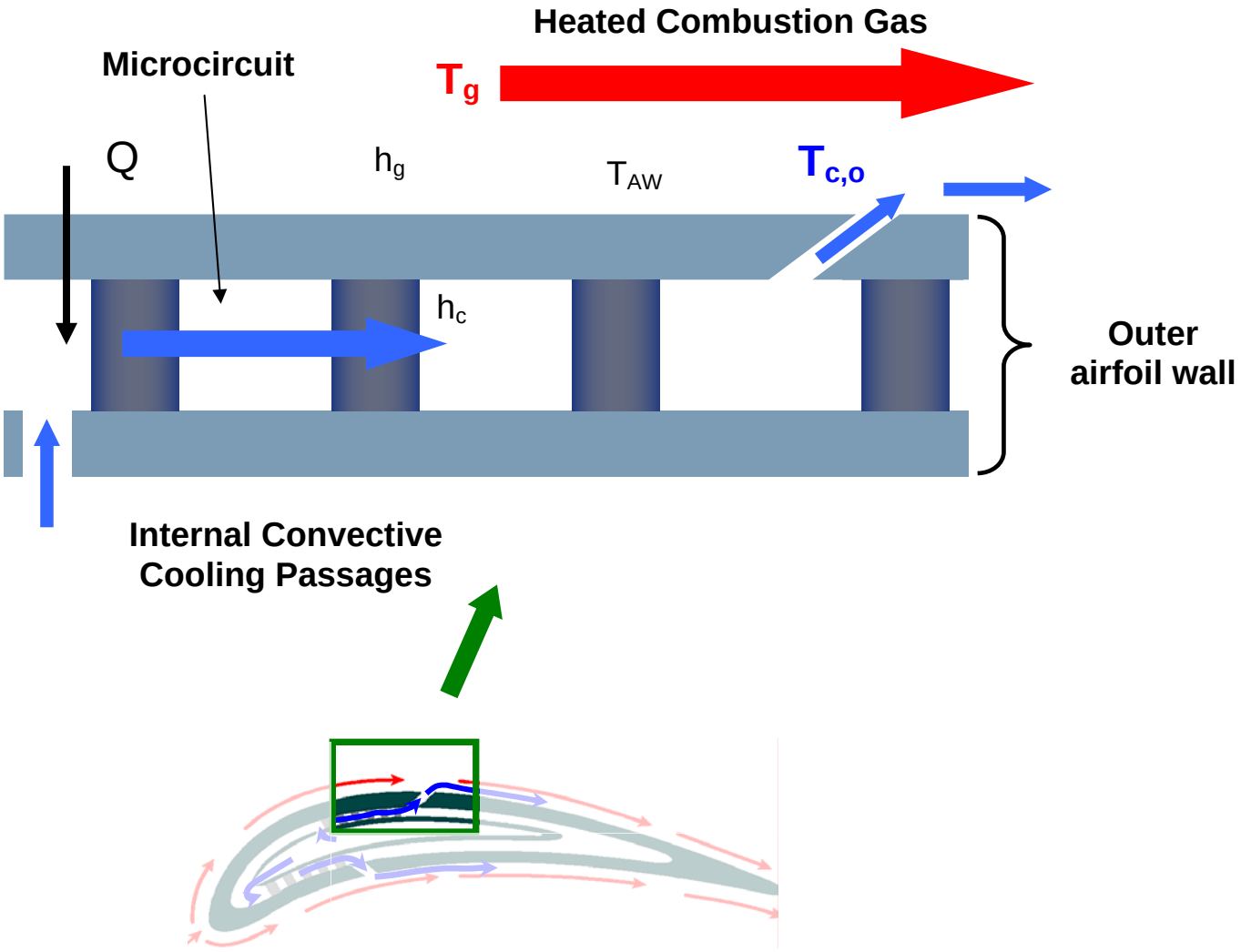

Figure 1-3. Cross section of internal cooling passage.

Chapter 2
Review of Relevant Literature

In a gas turbine engine, coolant flow is typically extracted from the compressor air and bypasses the combustor directly into the turbine. The reduction in system efficiency due to the extraction of coolant flow provides incentive to minimize the amount air used in cooling. A tradeoff exists between the amount of air necessary to cool the blade and the penalty incurred in the specific thrust and the specific fuel consumption (SFC).

The current test facility provides insight into combined internal and external cooling in order to optimize turbine cooling. While no literature exists in the area of combined internal and external cooling, significant research has been done on internal pin fin arrays and also on external film cooling. This chapter will discuss previously tested cooling methods in the context of cooling turbine blades with microcircuit designs. The first section focuses on internal cooling methods including impingement cooling and internal pin fin configurations. The second section discusses film cooling implemented through hole and slot cooling.

2.1 Internal Cooling Methods

The current microcircuit designs use a combination of impingement and pin fin cooling to increase heat transfer coefficients internal to the microcircuit. Impingement cooling, used at the microcircuit entrances, is the act of directing a jet of coolant air directly at the surface to be cooled. Impingement can be characterized by significant increases in the heat transfer caused by high turbulence at the point of the impingement. The point of impingement is inherently unstable, resulting in the movement of the jet impact location [Han, 2000]. The heat transfer in the region increases as the impingement point is moved closer to the jet inlet, as shown in Figure 2-1, where H is the distance from inlet to impingement point, D is the jet diameter, and Nu is dimensionless

heat transfer [Viskanta, 1993]. Also visible in Figure 2-1 is the fact that after impingement heat transfer rapidly decreases. Another parameter that impacts the heat transfer is the lateral jet spacing. The overall heat transfer for an array of jets increases with a decrease in jet-to-jet spacing due to the interaction between the jets [Obot and Trabold, 1987]. Cross-flow typically serves to increase the heat transfer coefficient, but in the case of impingement, the cross-flow often causes deflection of the impingement jet from its target decreasing the heat transfer coefficient. Florschuetz and Su [1987] have shown that cross flow less than 10% of the jet flow velocity causes an overall increase in cooling due to both cross flow and impingement cooling. Huang et al. [1998] determined that the exit flow orientations dictate the Nusselt magnitude of the local heat transfer coefficients for multiple jet impingements. Bunker and Metzger [1990] found an increase in heat transfer with approximately 0.6^{th} power of jet Reynolds number. A summary of the effects of geometry, temperature, interference and crossflow, turbulence levels, surface curvature, and non-uniformity of jet array on jet impingement heat and mass transfer can be found in Downs and James [1987].

The heat transfer in internal convective cooling passages can be augmented using dimpled walls, ribbed walls, and/or a section composed of a bank of staggered pin fins. The focus here will be staggered pin fin banks because two rows of pin fins make up a portion of the microcircuit designs. Pin fins are protrusions into the flow path that serve to increase the forced convective cooling of the flow by increasing the heat transfer surface area. The pins also increase the turbulence of the flow by causing flow disturbances and shedding wakes in the regions downstream of the pin. The conductivity of the material used to form the pins affects the amount of heat transfer seen by the pin fin bank, as shown in Figure 2-2 [Metzger and Haley, 1982]. The Nusselt number values are shown at a streamwise distance X/D = 2.5. X/D is a ratio of the streamwise distance to the pin diameter. Yeh and Chyu [1999] found that the heat transfer coefficient through the pins is approximately 0 to 10% higher than the endwalls for H/D = 1.0 pins and 10 to 20% higher than the endwall for H/D = 2.8 pins (H is the height of the pin fin and D is the diameter of the pin fin). Metzger [1984] and VanFossen [1982] found the contribution to heat transfer of the pin fins to be more significant with pin fin values being 35% and 100% higher than endwall conduction, respectively.

Nusselt numbers in a channel of staggered pin fins with unheated entrance with a height to diameter ratio (H/D) of 1.0, streamwise spacing (X/D) of 1.5, and a spanwise spacing (S/D) of 2.5 were measured at four Reynolds numbers by Metzger et al. [1982] and is shown in Figure 2-3. The test shows that there is an increase in Nusselt number over the first three rows of pins, and at this point the Nusselt number maintains a fairly constant value over the remainder of the channel. Ames et al. [2004] obtained similar results [2004]. The increase in heat transfer augmentation over the first three rows occurs because of the interaction between the pin fins and the wakes of previous pin fin rows. The highest turbulence intensity of the channel is measured before row 4. Armstrong and Winstanley [1988] compiled a review of the effects of various parameters on heat transfer in a pin fin array. The current windtunnel facility has the capability to further characterize Nusselt numbers values in pin fin arrays.

Friction factor values are often the driving design parameter in internal convective cooling configurations. As a result an attempt is made to optimize internal configuration to provide the highest heat transfer values and the lowest friction penalty. Yeh and Chyu [1999] found Fanning friction factors on the order 0.30-0.26 for a straight staggered array of pin fins over a range of Reynolds numbers from 10000 to 20000 for H/D =1. Chyu found slightly higher friction factors for the same pin fins after the addition of fillets (0.33- 0.26) at the same Reynolds numbers. Chyu [1990] also tested circular pin fins in comparison to cubes and diamonds. An increase in Fanning friction factor was seen for cubes and diamonds from 0.3 for circular pin fins to 0.4 and 0.45, respectively. Elliptical pin fins with the longer axis placed in the streamwise direction have a heat transfer capability of 25-30% less than the circular pin fin array with the same axis length. The circular pin fins cause 100-200% higher values of pressure loss than the elliptical pin fin arrays [Uzol and Camci, 2001].

Microcircuit cooling channels, which are internal to the blade must be designed with the maximum heat transfer capability while still providing adequate structural stability for the blade. Thin walls inside the channels require that the pin fins cover a significant portion of the surface area (over 50% in the case of the microcircuit designs). Due to the large blockage area, the friction penalties that are measured are significant. Bunker et al. [2004] completed research in the area of investment cast mesh cooling

configurations, classified as mesh due to the small height to pin diameter ratios and the small spacing distances in the streamwise and spanwise directions. These mesh configurations with H/D of of 0.2 and 0.3 and S/D of 1.5 and 2.14 differ from conventional pin fin arrays with H/D $\geq$ 1 and S/D ratios typically about 2.5. These results show 3 times the average channel heat transfer coefficients over a smooth channel. The friction coefficient enhancements measured in these tests were between 6 and 20.

Favre-Marinet et al. [2004] showed no scale effects exist in ducts formed between two flat plates, so that the classical laws of friction in two-dimensional ducts apply in tests that tested to a minimum height of 0.1 mm. Testing completed at low Reynolds numbers (20 – 7500) showed that conventional heat transfer laws are also applicable down to a minimum channel height of 0.5 mm. At a channel height smaller than 0.5 mm the heat transfer departs from the classical heat transfer law, which grows with a reduction in channel height. At this point the reduction in Nu is very strong for the narrowest microchannels at roughly 60% smaller than the conventional value measured in large-scale channels. The microcircuit channels tested in the current test are approximately 0.4 mm in height at engine scale, so the results of this test are significant in relation to the current test.

The application of tree-like microchannel nets has also been applied to the cooling of polymer electrolyte fuel cells [Senn and Poulikakos, 2004]. A tree net with six branching levels of decreasing channel diameter, generates almost half the pressure drop than the corresponding serpentine flow pattern having the same surface area and inlet Reynolds number. Although the number of bifurcations in the tree net is larger than the number of turns in the serpentine flow pattern, counterintuitively, the tree net causes a smaller pressure drop.

2.2 External Film Cooling Methods

Film cooling is the injection of coolant flow along the surface of the blade, forming a protective coating between the heated mainstream flow and the blade surface downstream of the injection location. Extensive film coolant testing has been completed on flat surfaces with variations in hole shape, size, and spacing, but most testing has been

completed on 35° inclined holes, an angle not applicable to microcircuits due to manufacturing constraints. Inclination angles around 35° are often selected because by injecting the coolant along the surface, mixing of the coolant with the mainstream flow is reduced. High heat transfer coefficients are undesirable in film cooling, and high coolant momentum enhances the heat transfer coefficients by forcing the coolant into the mainstream flow path producing local turbulence. Mixing raises the temperature of the coolant flow decreasing its cooling potential. Goldstein et al. [1974], Thole et al.[1996], and Sen et al. [1996] examined this effect on different coolant hole geometries. Shaped cooling holes, which decrease the coolant momentum, provide the most effective cooling. The cooling configurations used by Sen et al. are shown in Figure 2-4, and those used by Thole et al. are shown in Figure 2-5. The results also show an increase in the heat transfer coefficient due to mixing at the highest momentum flux ratios. Momentum flux ratio is defined as a ratio of the momentum of the coolant air to the momentum of the mainstream air.

The minimum microcircuit slot width/channel height allowed by the proprietary manufacturing method developed by Pratt and Whitney is 0.4 mm, much smaller than the channel height allowed by other manufacturing methods. The tradeoff for the micro-scale microcircuit passages is that the coolant flow must leave the cooling slots at an angle perpendicular to mainstream flow. The slot geometry, rather than the standard cooling hole, is also necessary due to the manufacturing method.

Testing of slots in film cooling have shown improved performance in terms of cooling effectiveness and heat transfer coefficient for 35° inclined slots with slot shaping [Farmer et al., 1997]. The effects are particularly visible far downstream of the slot as shown in Figure 2-6.

Wieghardt (1946) first correlated adiabatic effectiveness with X/Ms, normalizing the observed cooling effectiveness by the mass flow and the coolant feature shape. Gritsch and Schulz (2001) showed that internal cross-flows affect external adiabatic effectiveness.

Testing by Rhee et al. [2002] on a rectangular film cooling hole shows better performance for traditional round cooling holes at low blowing ratios, but the rectangular holes outperform the circular holes at high blowing ratios. These holes were inclined at

35°. The differences between this test and current testing are that the square cooling hole did not have a curved inner radius and were not affected by microcircuit features.

Smith et al. [2004] tests on the same slot shape for realistic Mach numbers of between 0.65 and 1.3. Results showed an increase in film-cooling effectiveness of as much as 25% as compared to the subsonic case. These tests were completed on a flat surface and heat flux measurements were made at discrete surface locations. Two plenum feeds were used in Smith's testing, and the slot was divided in half. Each half of the slot was fed by a separate plenum. Testing was completed on a normal and angled slot with significantly better cooling effectiveness measured with the angled slot.

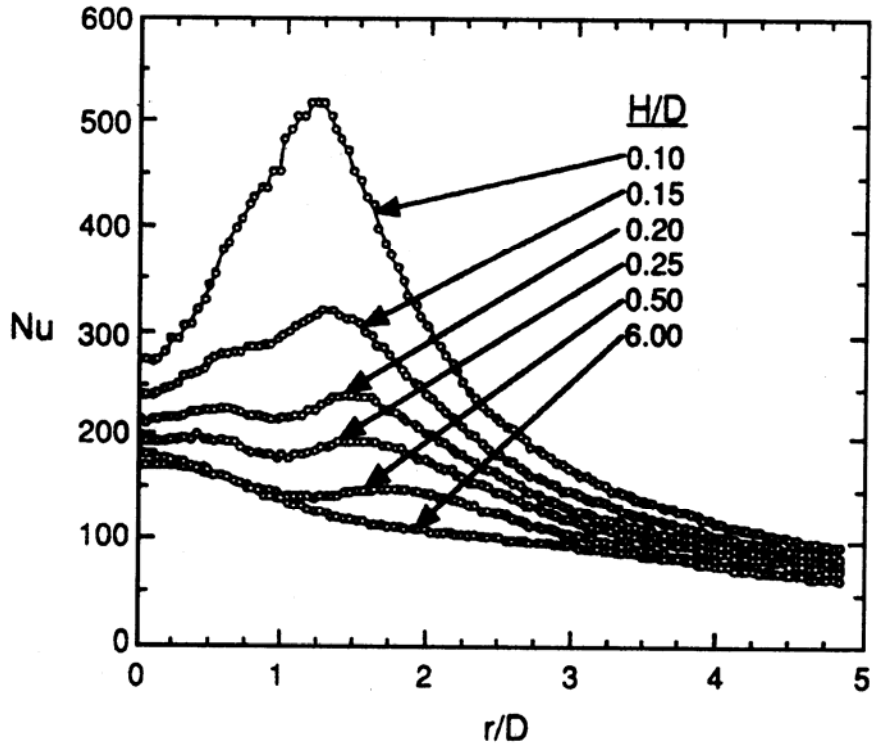

Figure 2-1. Effect of jet-to-target plate spacing on the Nusselt number distribution for Re = 23,000 for an impinging jet [Viskanta, 1993].

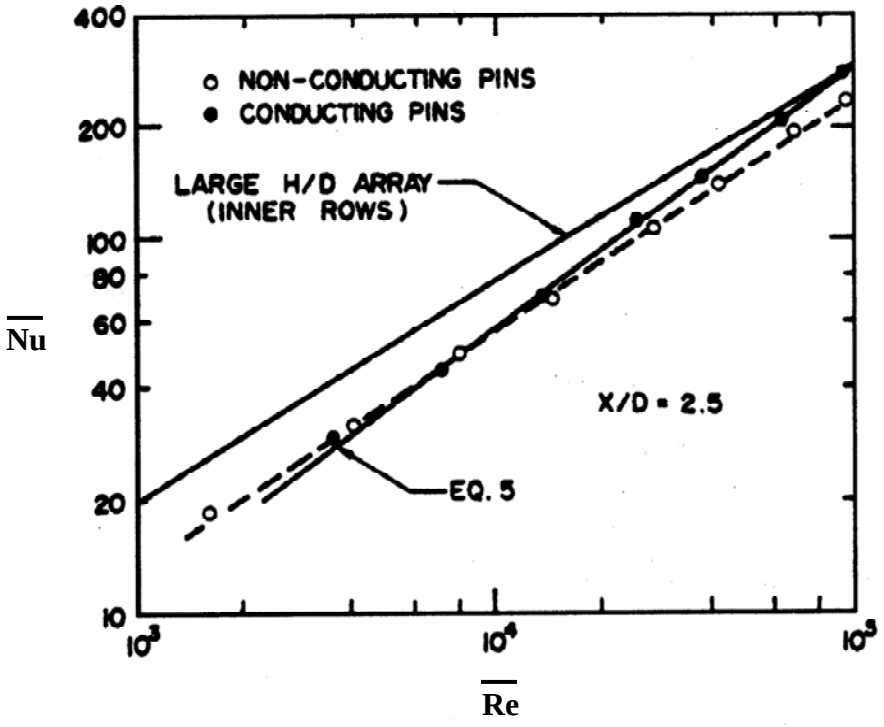

Figure 2-2. Effect of pin conductivity on average Nusselt number at different Reynolds numbers [Metzger and Haley, 1982].

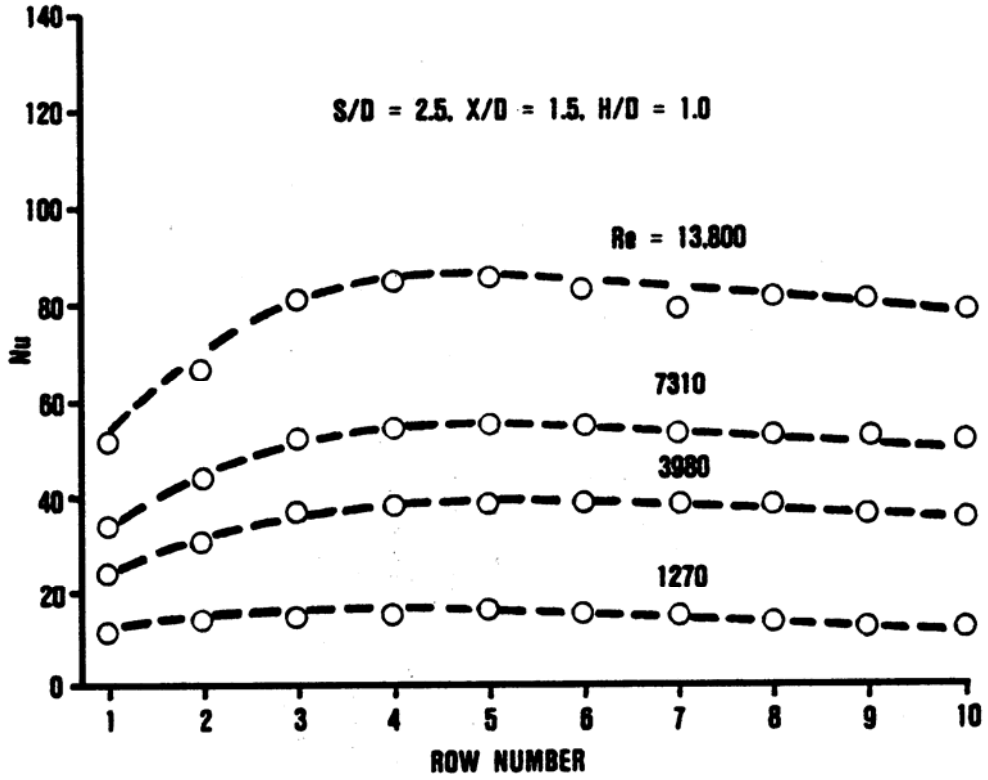

Figure 2-3. Nusselt number profile for an array of staggered pin fins [Metzger et al., 1982].

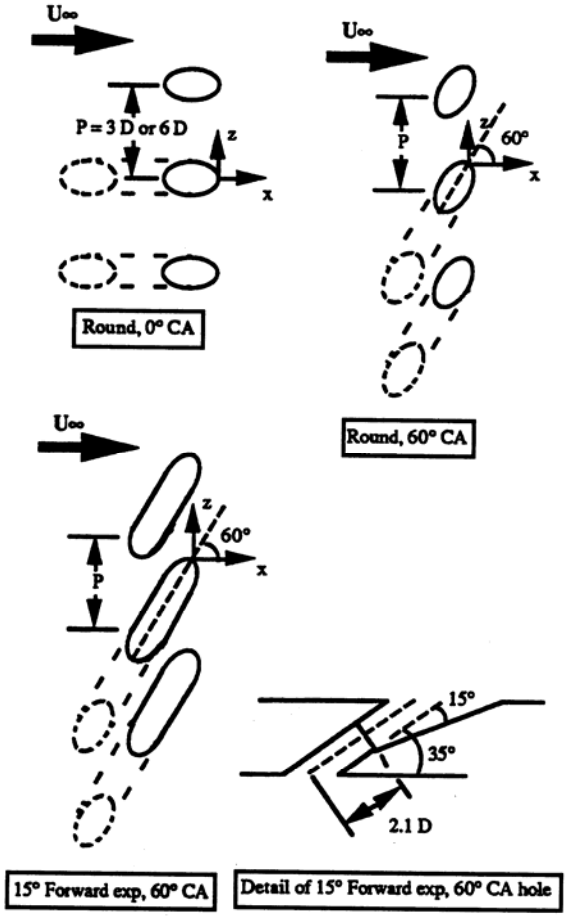

Figure 2-4a. Three hole configurations tested by Sen et al [1996].

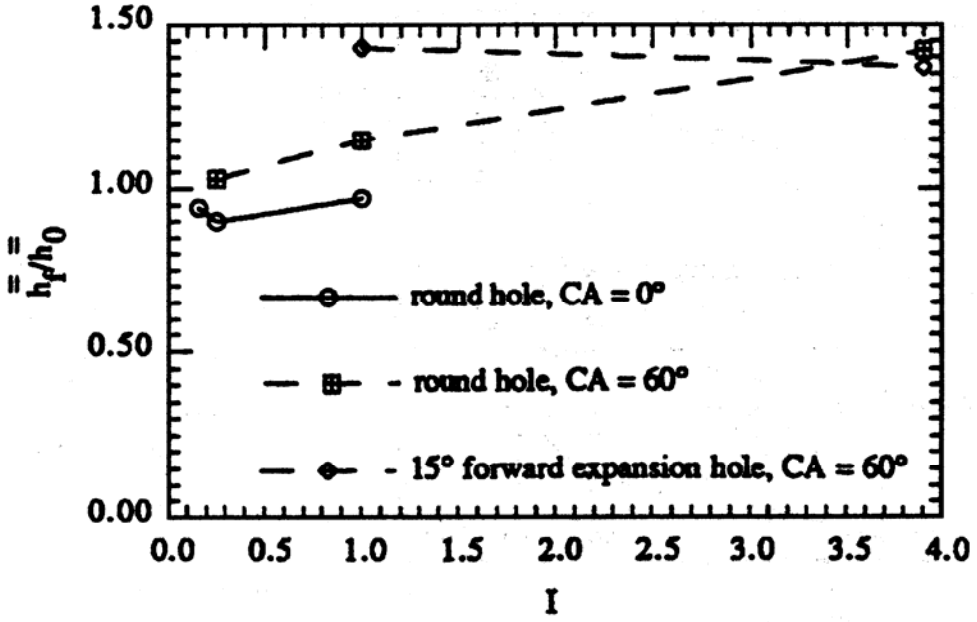

Figures 2-4a and 2-4b. Variation of spatially averaged heat transfer coefficient ratios with momentum flux ratio [Sen et al., 1996].

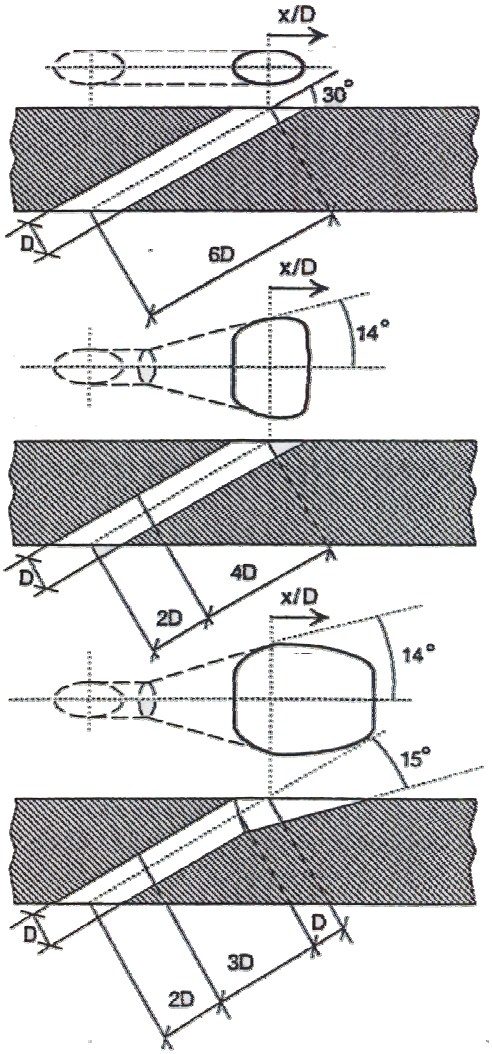

Cylindrical, fanshaped, and laidback fanshaped hole geometries

Figure 2-5. Cross section of film cooling designs studied by Thole et al. [1996].

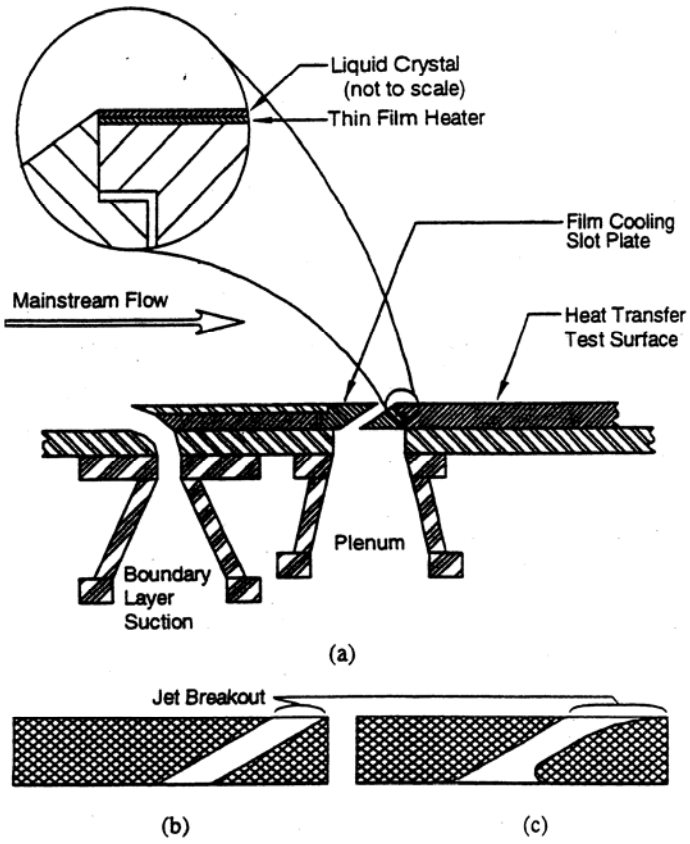

Figure 2-6a. Experimental test surface elements: (a) detailed view of the surface, (b) straight slot, and (c) shaped slot.

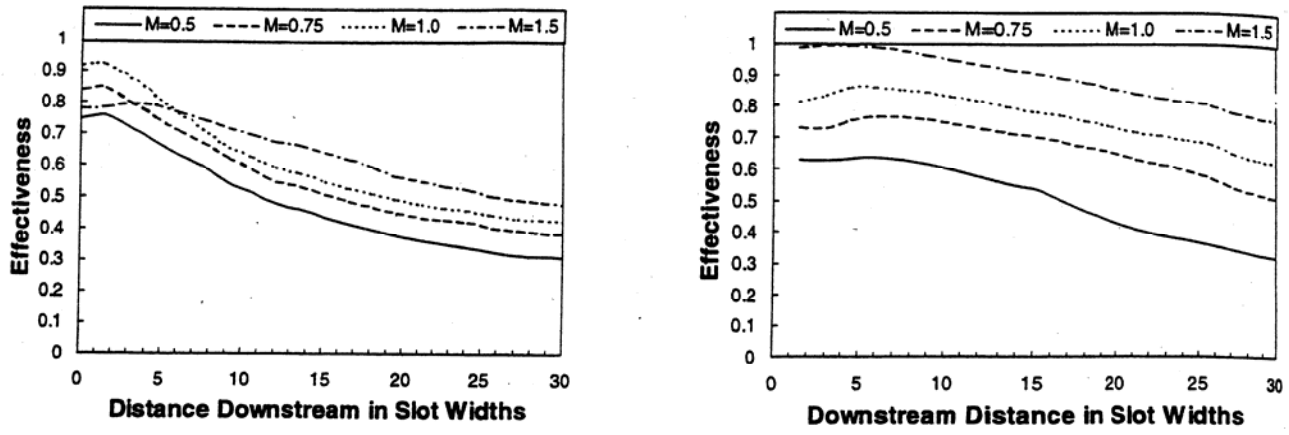

Figure 2-6b. Laterally averaged adiabatic effectiveness for a straight slot and a shaped slot at several blowing ratios [Sen, 1996].

Chapter 3

Design and Construction of Experimental Facility

Microcircuits have not previously been proven experimentally as a viable option for blade cooling. Microcircuit designs are changing rapidly as cooling strategies and manufacturing capabilities become more advanced. The need existed for a facility to test future microcircuit design iterations and to determine cooling capabilities exhibited by current designs. The large scale, low speed wind tunnel test facility was built for the measurement of heat transfer and friction factor information for blade designers' use. Large scale testing of microcircuit designs, scaled up twenty five times, allows experimenters to measure temperature contours at a higher resolution and allows for testing at temperatures and pressures significantly lower than those measured in actual turbines. The scaling factor of the current test facility was chosen to allow for measurement of both internal heat transfer and external film cooling efficiency using compressed air supply capabilities. The same microcircuit coolant flow path was used for internal and external testing, but was instrumented differently for the two types of tests.

This chapter will discuss the design and implementation of the test facility used for testing microcircuit designs. The internal coolant flow supply is discussed in the first section including descriptions of the experimental setup and construction, the instrumentation and data collection procedure, and finally the benchmarking procedure. The second section outlines the external test loop including the design and construction, instrumentation, and the data acquisition process. An uncertainty analysis for internal and external testing is completed in the third section.

3.1 Internal Coolant Supply

This section provides a description of the experimental facilities used to measure the heat transfer and friction factor inside microcircuit designs. Figure 3-1 provides a

composite schematic of the internal and external test facilities to orient the reader. The directional names, streamwise, spanwise, and pitchwise, shown in Figure 3-1 will be used to characterize direction throughout the remainder of this document. Note the location of the internal test facility, which will be described in this section. As an overview, the internal testing flow entered the microcircuit from nine independently controlled plenums, flowed through the feature areas, and exited to atmosphere. The dimensions of the internal test facility are presented in Figure 3-2. A heater instrumented with thermochromic liquid crystal (TLC) makes up one wall of the microcircuit channel. The liquid crystal changes color based on temperature, and images of the liquid crystal were taken at steady state conditions and converted to surface temperatures. Pressure measurements were also collected at 33 locations throughout the microcircuit to calculate the friction factors across the microcircuit features.

Internal Coolant System. The coolant supply, used for cooling in both the internal and external tests, originated from two tanks, which were pressurized by compressors. Internal mass flow rates tested corresponded to Reynolds numbers of 5000, 7500, 10000, and 15000. The main supply of air originated at a tank at the Virginia Tech Power Plant (Long, 2002) and provides compressed air to a piping system that runs throughout the Virginia Tech campus. This tank was automatically recharged at the power plant to maintain a supply pressure of roughly 550 kPa (80 psi). The Power Plant air supplied a high enough mass flow rate to test Reynolds number cases of up to 7500. 10000 and 15000 Reynolds number tests required a supplemental air supply, which originated in the Virginia Tech Aerospace and Ocean Engineering (AOE) Department of Randolph Hall (Edwards, 2002). This tank was pressurized to a maximum of 1400 kPa (200 psi) and the air was routed to the test section through standard polyvinyl chloride (PVC) pipe. The coolant flow supply path is presented in Figure 3-3. The pressure of the tank typically dropped by 345 kPa (50 psi) over an hour, and we would reactivate the compressor as needed. Dryers removed moisture from both tanks, which supplied air at ambient temperature. The temperature of the air from the tanks fluctuated based on outside air temperature, and the heat transfer coefficient and adiabatic effectiveness

values are normalized based on coolant temperature to account for this change as explained in the data analysis chapter.

Initially, braided compressed air hose with a diameter of 2.54 cm was used to connect the local air inlet to the test section located roughly 6 meters away. The hoses, designed to transmit high static pressures, were not optimal for transporting the air at the high flow rates needed in this experiment. Rather than increasing the supply pressure, this hose was replaced with 10.2 cm diameter PVC pipe. This dramatically reduced the frictional losses through the supply piping and allowed much higher microcircuit flow rates for the same compressed air supply pressure [Prausa, 2004].

To measure the coolant flow rate, a Validyne DP-103 pressure transducer with an 1.44 inH_20 diaphragm, rated for high line pressures, measured the pressure drop across the venturi tube (model CV-400) manufactured by Lambda Square, Incorporated. The venturi tube outside diameter measured 10.2 cm, and the flow was contracted to a 6.7 cm diameter at the area change location. The static pressure difference, measured in inH_20, across the precise area change was placed in the following formula provided by Lambda Square to calculate the flow rate in CFM.

$$\dot{m} = 146.09(\Delta P)^{0.5} \tag{3-1}$$

Per manufacturer recommendations, a constant diameter was maintained five diameters upstream of the measurement location, and 0.6 meters of PVC were added downstream of the measurement location to eliminate flow interruptions for two diameters downstream.

After the flow rate was measured the air was split into two separate flow paths using braided compressed air hose with a diameter of 2.54 cm. The hoses fed directly into the top and bottom of an air tank with eleven globe valve controlled exits as shown in Figure 3-4. Nine of these tank exits were used to feed nine separate plenums with the two remaining exits closed off. Braided compressed air hose was used to connect the octopus to the feed plenums. The hoses were initially cut to lengths based on connection distance but were replaced due to differences in pressure drop across the hoses of varying

length. This problem was discovered and rectified when problems were encountered in balancing flows into the nine inlet plenums.

The nine plenums each with dimensions 29 cm by 41 cm with a height of 6.5 cm slowed the air to a low dynamic pressure, thereby ensuring uniform flow into the microcircuit inlet channels. The shape of the plenums encouraged mixing of the air by directing the incoming jet of air into the wall of the plenum. The inlet was also located far from the exit of the plenum to minimize the effects of the high velocity jet in this region. The inlet dimensions are shown in Figure 3-5. The plenums opened directly to nine 90° smooth turns that were constructed from lexan as shown in Figure 3-6. The inlet feeds were distributed at 7.37 cm intervals such that they were aligned properly with the microcircuit inlets. Figure 3.7 shows the flowpath through the microcircuit test section.

Periodic conditions were created at the outside edges of the middle microcircuit by placing a microcircuit on each side of this instrumented microcircuit. The setup consisting of three contiguous microcircuits, shown in Figure 3-8. During testing for microcircuit design one (MC1), inlet channels ran along the outside of the plenum, but inconsistencies in the handmade channels were causing corresponding inconsistencies in the microcircuit inlet conditions. To eliminate this problem the wall of the plenum was moved out 5 cm to enclose the inlet channels and to allow air to flow into the microcircuit inlets directly from the plenums as is visible in Figure 3-8. This eliminated some flow balancing problems, but some remained.

The flow balance problems were resolved by relocating the pressure taps. The taps were initially placed at the microcircuit inlets because this is the point at which balanced flow is necessary. The impingement on the first row of microcircuit features made this location inherently unstable. The static pressure readings at this point fluctuated erratically and therefore did not provide dependable information about the amount of flow leaving the inlets. The pressure taps were then moved to the nine feed plenums as shown in Figure 3-9. While this location is not as close to the point of interest, the measured pressures gave a more representative characterization of the flow entering the microcircuits due to the constant, more measurable pressure readings.

Microcircuit test section. The air entered the microcircuit channel and flowed around the microcircuit features. The three microcircuit designs are shown in Figure 3-10. Overall the designs of the three microcircuits were very similar. The primary differences include the fact that MC1 had 1.27 cm diameter pin fins, and an asymmetric blockage before the slots, while MC2 and MC3 both had 1.02 cm diameter pin fins and symmetric blockages before the slots. The blockage shape in MC2 was longer and thinner than that used in MC3. Dimensional characteristics of the three designs are compared in Table 3-1, and the dimensions common to all three microcircuit designs are shown in Figure 3-11. All three microcircuits had a 0.953 cm deep channel as measured in the spanwise direction. During the testing of MC1, the features were made of Last-a-Foam FR6710 (k = 0.037 W/mK), which was assumed to be adiabatic. Virginia Tech Mechanical Engineering Shop made the features for MC2 and MC3 using computer numerically controlled (CNC) machining. For these two microcircuit designs the features were formed out of Alloy 110 copper due, selected due to its high thermal conductivity (k = 391W/mK). The change to copper was made to better emulate conditions in a turbine blade. A blade is constructed entirely of metal resulting in conduction through both the endwall and out the sides of the cooling features. The cooling features spanned the whole channel height of 0.95 cm (0.375 in). The back wall of the channel was made of 0.95 cm (0.375 in) thick Last-a-Foam FR6710 low thermal conductivity foam.

A heater, coated with an adhesive liquid crystal sheet, enclosed the top of the channel. For testing of MC1 the heater was a custom-made inconel heater manufactured by the Electrofilm MFG Company in Valencia, California. The original heater used to test MC1 consisted of a serpentine inconel circuit encased in electrically non-conductive kapton. The heater was designed to minimize gaps between the paths of the inconel foils, the heat sources. A 0.02 mm layer of copper foil was affixed to the top of the kapton to ensure even heating of the surface, thereby providing a constant heat flux boundary condition on one wall of the channel. To minimize turn-around time after the order of a new heater, off the shelf silinex encased heaters were used for the testing of MC2 and MC3. The gaps between the paths of the inconel foils were again minimized, and a copper layer again worked to ensure an even heating of the surface. At 75°C the thermal

conductivities of the kapton and silinex are 0.159 W/mK and 0.162 W/mK, respectively. The circuit used to power the heaters is presented in Figure 3-12.

A larger heater was selected for use with the copper features because heat was convecting out of the cooling features on the edges of the heater and amplifying edge effects. Creating near periodic thermal conditions with a larger heater minimized edge effects. Another change that was made before the testing of MC2 was the adhesive material used to adhere the heater to the individual pieces. For testing of MC1 very little conduction occurred to the foam features due to the low thermal conductivity of the features, and insulating silicone was an acceptable adherent. In the testing of MC2 and MC3 it was desired for heat to conduct freely to the features. This was achieved by replacing the conductive silicone with a thin layer of 3M Super 77 all-purpose spray adhesive.

In the cases of all three microcircuits, the heater did not cover the length of all three of the microcircuits, and cardstock was used to create an airtight channel in the areas outside the heater and also to act as a spacer to maintain the height of the heater and liquid crystal across the surface of all three microcircuits. An airtight seal was created in the joint between the cardstock and the heater with silicone. Care was taken to ensure that this seal did not protrude past the height of the card stock.

A viewing window was constructed out of 0.95 cm (0.375 in) anti-reflective glass, purchased from American Computer Optics, to allow for the digital pictures of the liquid crystal. A Lexan frame was made by the Virginia Tech ME Shop to hold anti-reflective glass directly to the liquid crystal surface. The antireflective glass was handled with rubber gloves at all times to protect the antireflective coating from the oils on our hands. Extra support was added to the lexan frame because the frame would bulge in the middle at the high coolant mass flow cases. An aluminum L-bracket was added to each side of the frame and created a strong support that alleviated this problem. A uniform height of heater, cardstock, and the silicone sealant was crucial to achieving accurate surface temperature measurements because any protrusions would result in a gap between the glass and the liquid crystal, thereby creating a thin gap of thermally insulating air.

The thermochromic liquid crystal (TLC) used to measure the surface temperatures on the heater was purchased from Liquid Crystal Resources, LLC, formerly Hallcrest

Inc., and was of type type R30C5W Coated Polyester Sheet. The TLC was adhered to the copper surface of the heater using the adhesive placed on the material by Liquid Crystal Resources. Because any air bubbles between the liquid crystal and the copper surface of the heater were visible in the temperature contours, a method of liquid crystal application was developed to eliminate air bubbles. Pressure was applied to one edge of the liquid crystal and copper to affix one end. Directional pressure was applied to the liquid crystal surface away from the portion that had already become attached, as the liquid crystal was affixed to the surface, giving the air an escape route. After application, the air was released from any small remaining bubbles using a needle.

Returning to the microcircuit channel, a paper printout of the microcircuit design was placed on the bottom foam surface of the channel during the testing of microcircuits 2 and 3. This paper had a dual purpose: to smooth the rough foam surface and to act as a guide for feature placement. During thermal testing 2.54 cm (1 in) Styrofoam insulation and a piece of plywood were used to apply uniform pressure and make the conduction effects more constant across the surface. The pressure was applied from behind using adjustable length supports. While setting up the test section for testing mating surfaces were sealed using silicone, which was used as both glue and sealant.

After weaving through the microcircuit features, the air exited through 0.95 cm by 6.35 cm (0.375 in by 2.5 in) slots that were fashioned out of adiabatic foam. Slot dimensions are shown in Figure 3-13, and an example slot is shown in Figure 3-14. The outside of the slot was open to atmosphere. Foam slots were replaced by machined Lexan for testing of MC2 and MC3 to eliminate inconsistencies in the handmade foam.

Measurement of Heat Transfer Coefficient Data. The test section was instrumented with thermocouples, thermochromic liquid crystal (TLC), and pressure taps. The temperature data collection process was completed separately from the pressure data collection. The heat transfer coefficient is defined as follows:

$$q''_{convection} = h(T_w - T_c) \tag{3-1}$$

where, h is the heat transfer coefficient, $q''_{convection}$ represents the power supplied to the heater minus a conduction correction, T_w is the wall temperature as measured by the liquid crystals, and T_c is the local coolant temperature. To calculate the heat transfer coefficient, h, it was necessary to capture temperature measurements for the local coolant temperature and the wall temperature. The coolant air increased in temperature as it moved further along the heater. In order to create a temperature matrix that was representative of this phenomenon, temperature values were measured at the microcircuit inlet and immediately before the slot exit. An array of temperatures was linearly interpolated between these two values through the use of the energy equation. The calculated values were used to represent local T_c.

Liquid crystal shows change in temperature due to the change in angle of the crystals, and the angle change of the crystals can be linearly correlated to temperature. In a normal liquid the properties are the same in all directions. In a liquid crystal material the properties strongly depend on direction even if the substance itself is in fluid form. The rod shaped molecules form crystalline arrangements specific to temperature, and the arrangements reflect different portions of the spectrum. The hue changes caused by the structure change of the crystals can be linearly correlated to temperature (Coleman et al., 2003).

The wall surface temperature, T_w, was calculated using digital imaging of liquid crystal hue values. 480 by 640 pixel Images of the liquid crystal were taken with a Minolta Dimage S404. The camera was bolted vertically in a wooden camera stand that guaranteed that the visibility of the same image area in each picture. The camera stand was black to minimize reflections in the glass and the glossy surface of the liquid crystal. A small hole allowed only the lens to be exposed and prone to reflections, and the rim around the lens was painted black to further combat reflections. In addition to the minimization of reflection from the camera stand, placing a black drop cloth around the camera eliminated the effects of uncontrollable ambient light sources on the images.

Two 100-Watt floodlights were used for illumination of the liquid crystal. The results of Camci et al. [1992] showed that at angles below 40° the lighting angle had a negligible effect on the measured temperature. It was also shown that the magnitude of lighting had only small effects on the hue values measured. Larger effects were

encountered with changes in the camera settings. Light magnitudes as well as camera and lighting angles were kept consistent throughout all tests using lighting and camera stands that were bolted into the test structure.

Liquid Crystal Calibration. The liquid crystals were calibrated in situ according to the method described by Douglass et al. [2003]. A liquid crystal sheet was adhered to an isothermal copper surface, rather than directly to the heater as in microcircuit tests. The copper was instrumented with thermocouples in a uniform grid and a constant heat flux silinex heater (Electrofilm MFG Company, Valencia, CA). The thermocouples were tested using an ice bath at 0°C. Thermocouples with temperatures that differed by more than ±0.1° from the ice bath temperature were remade such that all temperature readings fell within this range. The heater dimensions were identical to those of the copper block, and the heater was secured to the copper using 3M all-purpose spray adhesive. The copper was placed in the position normally occupied by the microcircuit, and lights and camera were arranged as described for testing. The heater was set to heat flux levels resulting in the desired temperatures, as measured by the inlaid thermocouples. Images were taken of the liquid crystal at 0.2°C increments over the reaction range of the liquid crystal. Measurements were made at larger increments of 0.5°C outside of the linear range of the liquid crystal to further characterize the crystal behavior. The resulting matrices derived from the digital images were converted from the red, green, and blue (RGB) values to hue values according to the following equation.

$$\text{hue}(H,S,V) \equiv \arctan\left(\frac{\sqrt{3}(G-B)}{2(R-G-B)}\right) \tag{3.10}$$

The hue values were then correlated to surface temperature using the measured calibration curve.

The liquid crystal that was used for benchmark testing was different than that used for testing of the microcircuits due to lack of availability. The first batch of liquid crystals had a linear hue-temperature correlation over a 5°C range as promised by the supplier. The second batch of liquid crystals was linear in two ranges, with each range

remaining linear for about 1.5°C as shown in Figure 3-15. Applying both linear correlations allowed use of hue values from both linear ranges, allowing us to capture a 3°C total temperature range.

Friction Factor Measurements. Static pressures were measured at multiple locations between the feature rows on the back wall of the microcircuit as shown in Figure 3-16. Pressure taps could not be placed on the middle microcircuit, due to the support structure, but were placed immediately outside of this microcircuit. The pressure taps were placed flush to the surface and a 45° angle was etched out of the tip of the 1.6 mm outer diameter pressure tap as shown in Figure 3-17. This angle was experimentally shown to be the most accurate angle for pressure measurements. The magnitudes of the pressure readings are contingent on location in the flow path, so the pressure taps were placed in the same location, relative to the microcircuit features, from one microcircuit test to the next. To provide an overall picture of the pressure at each streamwise plane, some taps were placed behind features as moving in a streamwise direction and some were placed in a more open flow path.

Pressure taps were routed to a Scanivalve wafer using 1.6 mm (0.063 in) ID Vinyl tubing. The Scanivalve provided a means of selecting each pressure tap remotely using a knob selection device. More precision is achieved by measuring with respect to a known pressure value than to atmosphere. For this reason, ΔP values were measured from the average of the 17 inlet pressures to each location in the microcircuit. The ΔP between the first row and atmospheric pressure was then recorded to convert these relative measurements to measurements with respect to atmosphere. Measurements for low Reynolds number cases were measured using a Setra 5 inH_20 pressure transducer. In the high Reynolds number cases these measurements were made with the 20 inH_20 Meriam Instrument 2100 series Smart Gauge transducer.

The voltage measured by the pressure transducer was fed into a National Instruments SCXI-1100 Data Acquisition Board (DAQ), used for data conditioning. The DAQ was set to read a 0-10 V analog input, and fed the data to a 12-bit A/D board. The digital signals were converted to pressure values using calibration curves and were displayed using National Instrument's LabView software. The scanning rate was set to

1024 scans per second and 1024 samples were averaged to calculate each data point. The same DAQ, A/D conversion, Labview system was used for collection of the temperature data from the thermocouples.

Internal Thermal Data Collection and Equipment. During microcircuit testing, liquid crystal images were taken at several heat flux settings. The heat flux leaving the heater was quantified by measuring the voltage across a precision resistor (1 Ω) in series with the heater. The current through the circuit could then be calculated, and the power to the heater was calculated using the known resistance of the heater. The heat flux added to the system was then calculated by dividing the total heater power by the surface area of the heater. For testing of MC1 the heater was powered by a Hewlett-Packard 6024A DC Power Supply. The remaining two microcircuits were powered by a Lambda Invensys Gen 100-15 DC power supply, capable of producing 100 Volts or 15 amps. The power, heat flux, and voltage input ranges for each Reynolds number are presented in Table 3-2. The large jump in power magnitude between MC1 and MC2 is due to the change in heater type. The heater resistance of the kapton heater was 1.14 Ω as compared to the silinex with a resistance of 54.5 Ω, and the area of the heater changed from 274 cm^2 to 774 cm^2 to minimize edge effects.

The number of images required to characterize the temperature over the entire heater surface changed after the first test. The foam pieces did not allow lateral conduction; therefore a higher temperature gradient could exist across a small area of the heater. The increased uniformity of surface temperature in MC2 and MC3, caused by the high thermal conductivity of the copper pieces, allowed the experimenter to take fewer images while the surface temperature was within the measurement range at all surface locations.

Measured hue values were converted to temperatures, which were, in turn, converted to a heat transfer coefficients (h). An algorithm was developed in Matlab to extract data corresponding only to h values within the linear hue-temperature range as discussed further in Chapter 4. After the effects of conduction are eliminated, the value of heat transfer coefficient is independent of the heat flux setting. Based on the consistency of the heat transfer coefficient, data from all the pictures was then assembled

into one matrix of heat transfer coefficients in which the values were averaged if multiple data points were collected at one pixel location.

As can be seen in Figure 3-18, only a small band of hue values could be correlated linearly to temperature. Figure 3-18 illustrates the visible ranges in each image of the liquid crystal. Due to the nature of the liquid crystal, an increase in the heat flux setting resulted in smaller ascertainable temperature range. This phenomenon made it particularly difficult to acquire valid data near the inlet to the microcircuits where the flow impinges on the first features and cools very effectively. The number of pictures required to collect data ranged from four to seven to ensure the collection of data at all pixel locations on the liquid crystal surface.

In order to lower the uncertainty of the temperature measured at each location to within an acceptable range, it was necessary to take twelve pictures at each heat flux setting. The effect of the radiation from the 100-Watt light sources was visible in the thermocouple readings. To attenuate this effect, the lights were turned off as the system came to steady state, and during the testing the lights were only turned on only while the camera shutter was open. The data taking procedure consisted of turning on the heater and allowing the heater surface to reach the liquid crystal visible temperature range. The coolant flow was then turned on at the mass flow rate selected based on desired Reynolds number. The wall thermocouple temperatures were monitored until they came to steady state, which usually took about 30 minutes from the time the coolant air was turned on. When the lights were turned the temperatures would rise, so a minute and half time period was allowed between each picture to allow the thermocouples to return to within 0.1°C of steady state temperature. After the temperatures stabilized, the next picture was taken, and the process was repeated until 12 pictures had been taken.

Coolant System Benchmarking. Liquid crystal temperature acquisition had not been previously used in the VTExccl lab, so the test method, as well as the new test rig, required validation. The test facility was modified slightly to validate the results in comparison to fully-developed open-channel flow.

Refer to Figure 3-19 for the internal benchmark test design. All of the flow measured in the Venturi was fed into a Lexan plenum from above and below in place of

the nine separate plenums. The two jets entered the channel in a parallel but opposite direction, so the jets hit each other and mixed inside the space. The air exited along a 6.3 mm deep channel. The inlet of the channel was made to mimic the microcircuit inlet feed channels with a 90º curved channel with a constant height of 0.953 cm. Rather than having three inlet feeds that were 1.59 cm long in the pitchwise direction as in regular testing, one inlet feed was constructed for the benchmark channel inlet that was 16 cm long in the same direction. The pitchwise width and spanwise height of the channel remained constant at 6.33 mm and 16 cm, respectively. The streamwise length of the channel, 21.7 cm, converts to an L/D_h ratio of 17, and is therefore long enough to consider the channel fully developed. The exit of the channel opened to atmosphere.

The bottom surface of the channel was covered with a Kapton heater with the top heater surface coated in copper and instrumented with liquid crystal. This arrangement allowed the measurement of the surface temperatures inside the channel for calculation of the heat transfer coefficient. Normalized Nusselt number values are then calculated from heat transfer coefficient as shown in the following equation:

$$Nu = \frac{hD_H}{k} \tag{3.11}$$

where, h is heat transfer coefficient, D_H is the length of the channel, and k is the thermal conductivity of the working fluid, in this case air. The open channel correlation used was an equation empirically derived by Kays and Crawford for fully developed flow in a straight, semi-infinite channel with a constant heat flux boundary and an adiabatic opposing wall [Kays et al., 1980] shown below.

$$Nu_o = 0.0285 \cdot Re^{0.75} \tag{3.12}$$

The measured straight channel results matched this correlation as shown in Figure 3-20. The data peaks initially due to entrance effects, and begins to level out at an L/D_h of 15. The peak at the end of the channel is due to a small overhanging section that does not have a constant heat flux boundary condition [Prausa, 2004].

In addition to demonstrating precision of the testing, the experimenter must show that the procedure is repeatable to validate results. Figure 3-21 shows the results from tests completed on MC3 one week apart. The test results are the same within experimental uncertainty.

Friction Factor Benchmarking. Friction factor values were calculated from pressure tap readings throughout the microcircuit. The friction multiplier as defined by Pratt and Whitney was calculated based on the friction factor values for comparison with Cunha's [2004] pin fin program, which was developed for Pratt and Whitney and was based on data given by Ishida and Hambe [1991], Sinko [1986], and Zakauskus [1972]. The pin fin program calculates the friction multiplier for a bank of pin fins. The friction multiplier represents a ratio of the pressure drop across the pin fin bank and the theoretical pressure drop across an open channel of the same dimensions. The pin fin program allows one to input the size and distribution density of the pin fins to calculate this value for most evenly distributed arrangements of pins.

Friction factors were used in the calculation of friction multiplier as well as for comparison with other published data. The friction factor, f, is defined in equation 3.13.

$$f = \frac{\left(\frac{\Delta P}{\rho} + \frac{1}{2} \cdot \left(V_1^2 - V_6^2 \right) \right)}{\frac{L}{D_H} \cdot \frac{U_{max}^2}{2}} \tag{3.13}$$

The ΔP was measured between points 1 and 4 as shown in Figure 3-22. The velocities at these two points were also taken to be V_1 and V_4. L, 10.2 cm, was the streamwise distance between location 1 and the exit to atmosphere. The hydraulic diameter of the channel is defined as four times the flow area divided by the wetted perimeter of the channel, which was 1.83 cm in this case. A normalizing velocity was required to non-dimensionalize the friction factor value. U_{max} was selected as this normalizing velocity to remain consistent with the pin fin program. The constant flow rate through the microcircuit mandates that the velocity change depending on the flow area. U_{max} was

defined as the velocity as the coolant flowed through A_{max}, the area of channels formed by the pin fins, shown in Figure 3-23.

The measured value of friction multiplier was calculated using the ΔP across the whole microcircuit and also across the pin fin portion of the microcircuit. The equation for friction multiplier in terms of measurable variables was reached after considerable cancellation, substitution, and rearrangement, and is shown in Appendix A. The final form of FM is shown below.

$$FM = \frac{\left(\frac{\Delta P}{4} \cdot \frac{2}{\rho U_{max}^2} \cdot \frac{D_H}{S_P} \cdot \left(\frac{U_{max}}{U_{bulk}} \right)^2 \right)}{f_0} \tag{3.14}$$

The ΔP was measured between points 1 and 4 as shown in Figure 3-22. U_{max} was defined as the velocity in the channels formed by the pin fins, and U_{bulk} is the open flow velocity as shown in Figure 3-23. The hydraulic diameter of the channel is defined as four times the flow area divided by the wetted perimeter of the channel, which was 1.83 cm in this case. S_p is the longitudinal distance between the pin fins. f_0 is the friction factor for an open channel which is calculated using the D'arcy friction factor correlation shown below in equation 3.15.

$$f_0 = 0.316\,Re^{-0.25} \tag{3.15}$$

This is known as the Blasius correlation, and represents the turbulent friction factor in a smooth pipe or channel [Munson, et al., 1998]. U_{bulk} is used as the velocity in the Reynolds number used in calculation of the baseline friction factor.

A comparison was made between the experimental friction multiplier in the pin fin region of the microcircuit, and the theoretical friction multiplier from the pin fin program. The results of this comparison are shown in Figure 3-24. While both the experimental and theoretical cases show a downward trend, the experimental results show a more exaggerated downward trend with increasing Reynolds number than the trend predicted by pin fin. The magnitudes of friction multiplier values are also not in

agreement with the pin fin predictions. While the friction multiplier values obtained are useful for comparison between microcircuit designs, the benchmark of this data was unsuccessful in proving the validity of the experimental friction factor values.

The lack of agreement between the friction multipliers from the pin fin program and the experimental results is due to a combination of factors. The pressure drop across the pin bank is the driving factor in changing the friction multiplier. Thus, the calculation of the pressures at locations 1 and 4 are critical. The pressure measurement at location 1 is inherently unstable due to the impingement at this location. Flow behavior in the experimental impingement jet is significantly different than that in an open channel, which is the initial condition in the pin fin program. Another factor is that the pressure measurements immediately downstream of the pin fin bank are made immediately before the large pedestal blockages. The flow encountering a large blockage can only move laterally, making the flow conditions significantly different than the conditions in an open channel. Cross-flow has a significant impact on the velocity at both the impingement location, and at the point directly after the pin bank. Results discussed in Chapter 5 also indicate that the effect of these large blockages is propagating upstream. These effects are relatively large in relation to the small value of pressure drop across this section of the microcircuit. As a result, the values of pressure drop measured across the pin fin bank alone are not consistent with those for a pin fin bank with no downstream blockages.

3.2 External Mainstream Loop

The distinctive feature of this test rig is that the internal heat transfer coefficients can be tested as well as the effect the internal features have on the external film cooling. The external cooling flow test section is shared with that of the internal testing and an additional external heated flow loop is run for these tests. This section will discuss the design and construction of the external loop as well as the mainstream instrumentation, data collection equipment, and procedure.

Mainstream Design and Construction. The external tests are run on a closed flow loop in which the air was heated by a heat exchanger. A closed flow loop

was selected to eliminate changes in the results due to slight fluctuations in the ambient conditions. The external tests were designed to run separately from the internal tests because the instrumentation for each type of test interferes with the testing for the other.

A mainstream velocity of 10 m/s was desired to achieve the blowing ratios required by Pratt and Whitney with a combination of the facilities compressed air and the AOE air compressor. It was also a requirement that flow path be wide enough to house three contiguously arranged microcircuits. Based on these flow path requirements a 13.75 hp Cincinnati Fan high-pressure blower was selected to circulate the flow at the necessary speed. The blower was powered by three-phase alternating current at 460 V. A motor controller allows for the selection of blower speed from 0-60 Hz. A blower speed of 39 Hz, which falls well within the range of the blower, results in a mainstream flow rate of 10 m/s. Blower vibrations were a concern, so the blower was placed on vibration absorption mounts, and the blower was connected to the flow path using a pliable rubber sheet.

Upon exiting the blower the air enters a large diffuser box constructed of 2.54 cm medium density fiberboard (MDF) with 1.52 m sides. In the diffuser the air is slowed to a velocity close to zero as it moves through the flow path with a constant area of 2.31 m^2. This conversion of dynamic pressure to static pressure, using a splashplate configuration, results in more uniform velocity and thermal profiles at the test section because pressure is driving the flow. The air flows directly into a square MDF blockage placed in the center of the flowpath. The air moves radially outward from the center along this flat surface where it moves around the outside of the blockage. At this point, the forward velocity is further obstructed by the placement of an "inverse splashplate" with open area in the middle and a blockage around the outside rim, the area where air is being directed from the first splashplate.

The two splashplates slow the air to the slowest velocity seen in the flow loop, making this the most suitable location for the heater or heat exchanger coil. The speed of the air passing a heat source inversely affects the amount of overall heat exchanged. The heat exchanger was selected over heaters due to cost and versatility considerations. The heat exchanger was a more versatile choice because of the ability to either heat or cool the mainstream air depending on the temperature of the fluid in the heat exchanger.

Super Radiator Coils of Richmond, Virginia donated the heat exchanger to VTExCCL. The specifications for the heat exchanger are presented in Appendix B.

Heat loss calculations were completed on the flow loop to determine that 4.2 kW had to be added to the flow to maintain the desired 10ºC temperature differential between the mainstream and coolant flows. Based on the speed of the air and hot water flow, the heat exchanger water had to be kept at a constant temperature of 80ºC. The water was heated using a commercial hot water heater with an 80-gallon tank, type American Standard CE-80-AS-18, which was rated to 18kW. The hot water heater was sized to allow the system to come to test conditions within a reasonable amount of time. The hot water tank was heated by three 460-volt heating elements.

To achieve the required heat exchange, the water was pumped through the heat exchanger at a speed of 9.5 liters per minute. A 0.04 hp TACO cast iron pump was used to circulate the water to the heat exchanger at the required flow rate.

After crossing the heat exchanger, the air was channeled into the mainstream of the test section. A smooth contraction was designed to reduce the flow area by a factor of 10 to 1 to ensure flow uniformity. The design of the contraction was complicated by the non-uniform contraction of the flow path from a square to a rectangle with an aspect ratio of 3.5 to 1 over a relatively short length. A horizontal contraction of 83% and a vertical contraction of 41% were completed over a length of 1.67 m as shown in Figure 3-25. The contraction design was constructed in an S-curve configuration, the dimensions of which were designed according to equations developed by Su [1991]. The equation for the s-curve is shown below:

$$F = \begin{cases} 1 - \dfrac{(x/L)^n}{X^{n-1}} & 0 \le x/L \le X \\ \dfrac{(1-x/L)^n}{(1-X)^{n-1}} & X \le x/L \le 1 \end{cases} \tag{3.16}$$

where F represents $(H - H_2)/(H_1 - H_2)$ and X is a shape parameter. H_1 and H_2 are the height of the contraction at the inlet and exit, respectively. An appropriate shape parameter, X = 0.3 in both the horizontal and vertical directions, was selected using computational fluid dynamic (CFD) predictions. Selection of X was based on

optimization of the uniformity of flow field velocity leaving the contraction. CFD predictions found the flow velocity to be within ±2.5% after the contraction. Appendix C shows the geometric details of the s-curve contraction. A contractor for the Virginia Tech Physical Plant built the contraction from 0.32 mm cold rolled steel. The eight metal segments were cut out separately and then welded together, two to a side. The weld beads were ground off to make a smooth surface, and 5.1 cm flanges were attached to the inlet and exit of the contraction for attachment to the test rig. The steel contraction section was a significant source of heat loss leading to the formation of a cooler thermal boundary layer along the wall. To partially alleviate this problem, an insulation box was formed around the outside of the contraction.

The test section was the next portion encountered in the mainstream flow loop. Two walls of the mainstream were made of 0.953 cm Lexan. The remaining two walls were made of 2.54 cm MDF. The bottom surface was covered with a Formica sheet to provide a smooth surface. A 0.953 cm layer of foam was affixed to the MDF on the wall to make the wall theoretically adiabatic and to provide a uniform surface for infrared (IR) images. The IR camera best resolves temperatures on surfaces with high emissivity. The foam imaging surface was coated with XO-19 flat black paint, made by X-O Rust, to increase the emissivity of the material [Couch, 2003].

A bleed slot was added with the intention of removing the cooler boundary layer that had formed along the surface of the contraction and to create a constant velocity flow field as possible at the test section. The boundary layer removal was achieved by creating a slot along the surface which was piped, using 15.24 cm piping, to a high speed, low static pressure section in the return duct, which will be discussed in detail later. The higher static pressure in the test section would force the air near the wall out to the lower pressure area.

Immediately after the slot, the piece of foam was shaped to promote the splitting of the streamlines. The foam decreased the flow path by 0.953 cm. Streamlines could either enter the bleed slot or continue along the surface of the test section wall. A pressure difference from before the slight diffusion to after the bleed slot allowed detection of the amount of bleed off. In theory, the pressure difference would be zero if only the boundary layer was removed. If too much air were removed, then the flow

would be moving more slowly than before the slot and a negative pressure differential would be measured. If not enough air was removed, then the pressure differential would be positive due to the higher speed of the air after the flow path was made smaller by the layer of foam [Prausa, 2004].

The amount of boundary layer flow was adjusted by lowering the static pressure in the bleed off section. Prausa [2004] lowered the pressure at this location by increasing the speed in the bleed off section of the return duct by adding a flow obstruction.

After boundary layer removal, the flow traveled a distance corresponding to the distance from a vane stagnation point to the first row of microcircuits (71.4 cm). At this point, the coolant entered the flow through the nine plenum, three microcircuit configuration described in Section 3.1. The coolant air exited to the mainstream flow path through six staggered slots that were initially fashioned out of adiabatic foam. Slot dimensions are shown in Figure 3-13, and an example slot is shown in Figure 3-14. A demonstration of slot construction is shown in Figure 3-26. Foam slots were replaced by machined Lexan for testing of MC2 and MC3 because unexpected results led to questions about the effects of inconsistencies in the handmade slots. The trailing edge of the three upstream slots was placed 71.4 cm downstream of the bleed slot. The leading edge of the three downstream slots was positioned on the same line. The adiabatic foam surface stretched 100 slot widths downstream of the coolant slots to allow for characterization of the film cooling along the surface.

A joint between sheets of foam was located 28 cm downstream of the coolant slots. The joint would be visible in the infrared (IR) images and had to be masked with a material with similar heat transfer properties and similar emissivity. This joint was filled with expandable foam according to the method described by Couch (2003)

The wall temperatures were measured along the foam surface for calculation of adiabatic effectiveness. The equation for adiabatic effectiveness (η) is shown below.

$$\eta = \frac{T_\infty - T_{AW}}{T_\infty - T_C} \tag{3.17}$$

where T_∞ is the mainstream temperature, T_{AW} is the wall temperature measured by the infrared camera (IR), and T_C is the coolant temperature. The mainstream and coolant temperatures were measured using thermocouples.

IR images must either be taken of the surface directly or through a specially made Zinc-Selenide window that allows transmission of the IR wavelengths. IR camera ports were built into the Lexan wall opposite of the cooled surface. The ports allowed for the direct imaging of the surface, but to maintain steady state conditions of the mainstream flow loop the ports had to be made airtight during the imaging process. The opposite wall was also only 26 cm away from the cooled surface, while the minimum focal length of the camera was 30 cm. A cone shaped extension was built to accommodate the focal length requirement and to seal the area around the camera.

Lexan insert panes were constructed with one fitting to the cone shaped extension. The panes could be quickly removed and placed into a configuration with the extension piece located at the image location. Converting quickly from one picture to the next was necessary to allow the system to quickly return to steady state.

The IR camera ports were placed in nine locations to allow full visualization of the slots and the area cooled by the two middle slots. At the focal length of 30 cm the image area is 10.5 by 14 cm. The ports were positioned to take images that overlapped slightly at the edges to ensure that no data was missed in the gaps between pictures as shown in Figure 3.27. One composite image of the surface temperature contour was compiled from the individual images after the data analysis process. The composite image was generally made up of seven pictures per test. This change was made after initial testing using nine image locations showed balanced flow through the 6 slots.

A camera stand was custom designed for holding the IR camera up to the camera ports. The stand consisted of an aluminum tube with a flat MDF platform mounted on top. A bolt hole on the bottom of the camera allowed it to be bolted across the platform. Rotation of the camera on the platform was eliminated by custom fitting pieces of MDF onto the platform around the shape of the camera. The bottom of the stand was a five-sided support structure that held the platform at the lowest image location. A pin and hole system was used to raise the platform to the heights of each of the image port locations. A pin was inserted into a hole in one side of the support structure, through

strategically placed holes in the aluminum pole, and then out a hole on the opposite side of the support structure. The support structure and platform could be moved to three streamwise locations to record images for 31 slotwidths in the streamwise direction.

The test facility was maintained at constant flow area for a distance of 100 slot lengths downstream to eliminate downstream effects in the test section. At this point a transition was made to a wider duct. The duct diverged horizontally at an angle of 15° over a distance of 71.3 cm. This expansion was to make the downstream transition to a square duct as smooth as possible. Three sides of this transition section were constructed from 2.54 cm MDF, and the top was made of Lexan to provide an access port to the downstream curved duct. The side and bottom walls were covered with a Formica sheet to guarantee a smooth surface.

Following the expansion section the area remained constant at 49.7 cm in width by 90 cm in height for a length of 2.2 m. This distance was chosen to attenuate the effects of the upward bend on the test section. The upward bend was designed to return the flow to the blower. The first segment of the return duct channeled the flow to a square cross section with while also changing the direction of the flow by 90°, directing it up. The sides of this turning section was made of 2.54 cm MDF, the sides were made of pre-curved 16 gauge stainless steel. The remaining turning sections were made with 63.55 mm hardboard sides, to minimize size and weight, and 16 gauge stainless steel. All stainless steel sections were covered in insulating foam. A 2.54 cm flange allowed for connection between sections of the return ducting.

The next portion of return duct turned the flow 90°, using the same MDF and steel construction, so that it was moving parallel to the test section flow but in the opposite direction. The return duct was built of 63.5 mm hardboard in 1.22 m sections, and followed the entire length of the test facility. Aluminum L-bracket was used to make the duct from the boards, and all corners were sealed with silicone. A total of six 1.22 m sections and two custom sized sections were used to return the air to the opposite end of the test facility.

Ducts, constructed in the same manner as was previously discussed, were utilized to feed the air into the side entrance of the blower. A total of four 90° ducts were needed

to guide the air directly into the fan inlet. The return duct was attached to the blower using a flexible rubber attachment to isolate vibration.

External Mainstream Instrumentation. One important assumption in calculating values of η is that the surface must be adiabatic. This is because the actual temperature that is necessary for the calculation of η is that of the air directly in contact with the wall rather than the wall temperature. If the surface is adiabatic, then there is no heat flux, and these two temperatures are equal. In this experiment the foam wall on which the IR images were taken was assumed adiabatic, and the surface temperatures were measured.

Thermocouples were used to measure the flow temperatures in the test loop and also for calibration of the IR images. The IR camera is very effective in measuring temperature gradients, but calibration is required to ensure that the absolute temperatures are accurately measured. The wall in each image location was instrumented with a thermocouple in the hottest and coolest areas of the image as predicted by rough CFD estimates. For mounting of the thermocouples, holes were drilled in the foam and the thermocouples were placed flush with the mainstream surface. The area around the thermocouples was filled with OmegaBond OB-400, made by Omega, a high thermally conductive and low electrically conductive material. Because of the high thermal conductivity of the material, the mass of OmegaBond stayed the same temperature as the wall with which it came into contact.

Thermacam Pro, IFA300 version 4.5, was a program distributed by the FLIR Corporation and was used for calibration purposes. The thermocouples were visible in the IR images, taken with a FLIR P20 Infrared Camera, due to the change in radiative properties of the foam and the OmegaBond. The absolute temperatures at the two thermocouple locations were known, and adjustment of the emissivity and background temperatures allows one to match the known temperatures to the temperature magnitudes at the thermocouple locations. Thermocouple locations were placed only in areas with a low temperature gradient because in high gradient areas, a slight change in temperature sampling location led to large changes in measured temperature. The changes in the

emissivity and background temperature adjust the surface temperature, T, according to the following relationship:

$$T = \sqrt[4]{\frac{1}{\varepsilon \cdot \sigma}\left[q''_{rad} + (\varepsilon - 1) \cdot \sigma \cdot T_{bg}^4\right]} \tag{3.18}$$

where ε represents the surface emissivity, σ is the Botlzman Constant, and T_{bg} is the temperature of the environment surrounding the surface. q''_{rad} is the total radiation heat flux measured by the IR camera. When the mainstream temperature is 51.8°C, typical values for the parameters used in calibration are as follows: ε = 0.94, T_{bg} =76.5.

A composite image was made of the temperature contours from all image locations using Matlab code developed by Knost [2003]. The images were positioned based on marker locations that were readily visible in the images. These markers were placed in opposite corners of the images to improve the positioning resolution of the program. The thermocouple and marker locations are detailed in Figure 3-28.

The pressure difference between the plenum mixing box and the test section allowed for the calculation of the mainstream velocity using the Bernoulli equation. The plenum velocity was assumed to be zero, and the pressure at both locations was known. As documented in the internal testing section, the total coolant flow rate was measured across a venturi tube, and the octopus valve system was used to balance the coolant flow entering the nine microcircuit inlets.

External Mainstream Data Acquisition Equipment and Procedure. A National Instruments SCXI-1100 data acquisition module conditioned all thermocouple and pressure transducer signals. The module passes the data to an SCXI-1000 chassis, which collects the voltage measurements and passes them to a 12-bit analog to digital conversion board on the computer. The manufacturer must calibrate pressure transducers, and the calibration constants are used to scale the voltage readings. After the voltages are collected, the temperature and pressure values can be monitored on a computer display in Labview. Before use, the thermocouples are selected for use only if the uncertainty of the thermocouple lies within ±0.2°C during an ice-bath test.

The first step in the test protocol consisted of turning on the heat exchanger/ hot water heater flow loop. After a few minutes, the temperature of the copper heat exchanger feed pipe would level out, and the blower was turned on using the digital motor controller. For most test cases the blower setting was 39 Hz, resulting in a mainstream flowrate of around 10.5 m/s. The system was allowed to equilibrate under these conditions for a minimum of two hours.

After the mainstream conditions were determined to be stable, pressure measurements were taken to determine the mainstream velocity and density. These velocity and density calculations determined the amount of coolant flow needed to achieve the required mass flux ratios. Table 3-3 shows internal and external running conditions expressed in mass flow rates and Reynolds numbers for comparison.

The same coolant flow loop used in internal testing, was then turned on at the proper flow rate and the coolant leaving the exit slots was fed into the mainstream. The plenums were balanced with respect to each other to verify that coolant inlets all saw equal amounts of flow. The whole system with heated mainstream and coolant flow was allowed to come to steady state for a period of about 30 minutes, at which point wall temperature readings were used to verify steady state conditions in the flow circuit.

When flow and thermal conditions were steady, the mainstream flow velocity and density were then calculated for the flow conditions using the pressure readings at various points in the test rig. The flow rate was then measured across the venturi tube for a period of two minutes, and the value was averaged to determine the mass flow rate of the coolant air. Labview was used to record the mainstream, coolant, and wall temperatures for each image set while IR images were being taken. Eight images were taken at each image location to decrease the uncertainty of each surface data point. The data from these eight images was later averaged together in Matlab. The data acquisition was stopped after the images were collected.

After the completion of data collection for one image set, the IR window port and camera stand were repositioned to prepare for the next test. After the test facility was set up for the next test, the mainstream flow was given time to return to steady state, which was usually a period of about fifteen minutes. As the tunnel returned to steady state, the pictures were uploaded to the computer to verify that there were no slight shifts in the

data collection location from picture to picture. If there were inconsistencies between the pictures, then the images at that location would be retaken, otherwise, the data was acquired for the next image location.

External Mainstream Benchmarking. Velocity and thermal profiles of the mainstream flow were taken before external testing to ensure the uniformity of the flow field in the test section. Velocity measurements were measured two slot widths upstream of the slot using a pitot-static probe. A thermocouple was attached to this probe to take corresponding temperature measurements. The velocity measurements, taken upstream of the film cooling slots in both the horizontal and vertical directions, are shown in Figure 3-29, as well as a horizontal temperature profile. Both the temperature and velocity boundary layers are distinguishable in these measurements.

Precision and repeatability are necessary to validate a test method. Figure 3-30 shows spanwise averaged adiabatic effectiveness for a blowing ratio of M = 0.50. The data is averaged across one periodic microcircuit and includes two slots. The data shows repeatability within the measurement uncertainty. The data for the two cases was taken three weeks apart, and the η values are similar. The similarity between the two data sets indicates that results from the test facility are independent of outside stimuli.

Adiabatic effectiveness results were compared to a correlation developed by Seban [1956]. Seban's tests were completed unshaped slots that entered the flow at a 90 degree angle from the direction of flow. These tests were similar in that they were completed at low Mach number and at similar blowing ratios. The tests are different in that the tests are fed by an open plenum, whereas in the current testing, the air leaving the slot has encountered and possibly been affected by the microcircuit feature. Seban's correlation is shown below in Equation 3.19.

$$\eta = 2.2\left(\frac{X}{Ms}\right)^{-0.5} \tag{3.19}$$

X is the streamwise length past the slot, M is the blowing ratio, and s is the injection slot height. A comparison was made between this correlation and a line of data extracted

from the centerline of the slot in the case of M = 0.5. The results are in agreement as the air exits the slots, but the Seban coolant shows higher effectiveness further downstream as seen in Figure 3-31. The higher values downstream can be attributed to the fact that the slot is a discrete rather than a two dimensional slot. The air leaving the discrete slot spreads out more than the air leaving a straight slot. This spreading effect is resulting in decreased cooling effectiveness downstream.

3.3 Experimental Uncertainty

Uncertainty analysis was completed for high and low values of η, Nu, and friction factor by the method described in Moffat [1988]. Each of the values is expanded out to show the experimentally measured values used to compute the calculated values. The partial derivative of the expanded equation is taken with respect to each of the experimental values. These partial derivatives provide a weighing factor. The uncertainty of each experimentally measured value is then multiplied by its corresponding weighing factor. The root sum of squares of these values is taken as the overall uncertainty. The uncertainty values are summarized in Table 3-4, and are presented in detail in Appendix D.

The uncertainty calculations show that the measured Nusselt number values are accurate to within 2-5%. Similar absolute values of total uncertainty are measured at all magnitudes of Nusselt number, but dividing by a low Nusselt number results in a higher percent uncertainty. Friction factor uncertainties were consistently on the order of 2% for all values of Reynolds number. η uncertainties varied based on the local magnitude of η. At low values of η the uncertainty was on the order of 19%, while at high values of η the measurements were accurate to within 3.7%.

Table 3-1. Geometric Specifications of Three Microcircuit Designs

	MC1	**MC2**	**MC3**
Open flow area (%)	66	71	68
Pin fin diameter (cm)	1.27	1.02	1.02
Metering area (cm^2)	4.53	3.63	4.16
U_{max} flow area (cm^2)	1.39	1.61	1.61
Sn (transverse) (cm)	1.1	1.96	1.96
Sp (longitudinal) (cm)	1.92	1.92	1.92

Table 3-2. Power, Heat Flux, and Voltage Input Ranges for Internal Tests

	MC1					
Reynolds Number	**q**		**q''**		**Voltage**	
	minimum (W)	maximum (W)	minimum (W/m^2)	maximum (W/m^2)	minimum (V)	maximum (V)
5272	13	26	465	937	7.5	10.5
6945	13	60	465	2204	8	12
10496	17	43	634	1576	9	14
15127	19	60	699	2194	9	17

	MC2					
Reynolds Number	**q**		**q''**		**Voltage**	
	minimum (W)	maximum (W)	minimum (W/m^2)	maximum (W/m^2)	minimum (V)	maximum (V)
5317	51	74	654	953	53.5	64
7637	82	123	1060	1587	68	83.3
10097	105	127	1359	1638	77.1	84
14843	115	121	1489	1563	82.6	90.9

	MC3					
Reynolds Number	**q**		**q''**		**Voltage**	
	minimum (W)	maximum (W)	minimum (W/m^2)	maximum (W/m^2)	minimum (V)	maximum (V)
5396	60	101	776	1303	57.9	75.1
7434	56	104	727	1343	56	76.2
10056	84	131	1079	1690	68.7	89.7
14380	99	143	1278	1853	74.8	90.1

Table 3-3. Running Conditions for Internal and External Testing

Table 3-3a. External Running Conditions Including Reynolds Number of Coolant Flow

Mass flux ratio	0.506	0.75	1	1.44
Coolant Reynolds number	3190	4700	5870	8580
U_{inf} (m/s)	10.37	10.40	9.74	9.75
$U_{internal}$ (m/s)	2.76	4.09	5.08	7.40
Mass flow rate (kg/s)	0.0064	0.0094	0.0118	0.0172

Table 3-3b. Internal Reynolds Numbers and Running Conditions for Comparison

Coolant Reynolds number	5400	7430	10060	14380
U_{inf} (m/s)	N/A	N/A	N/A	N/A
$U_{internal}$ (m/s)	4.58	6.35	8.52	12.09
Mass flow rate (kg/s)	0.0108	0.0150	0.0203	0.0289

Table 3-4. Experimental Uncertainty Results

Variable	**Value**	**Case**	**Total Uncertainty**
η	0.22	Low η	0.41 (19%)
η	0.9	High η	0.337 (3.7%)
Nu	160	High Re, High Nu	3.43 (2.1%)
Nu	88.4	High Re, Low Nu	2.94 (3.3%)
Nu	128.3	Low Re, High Nu	4.04 (3.1%)
Nu	65	Low Re, Low Nu	3.24 (4.9%)
f	0.971	High Re	0.018 (1.9%)
f	1.029	Low Re	0.0007 (1.9%)

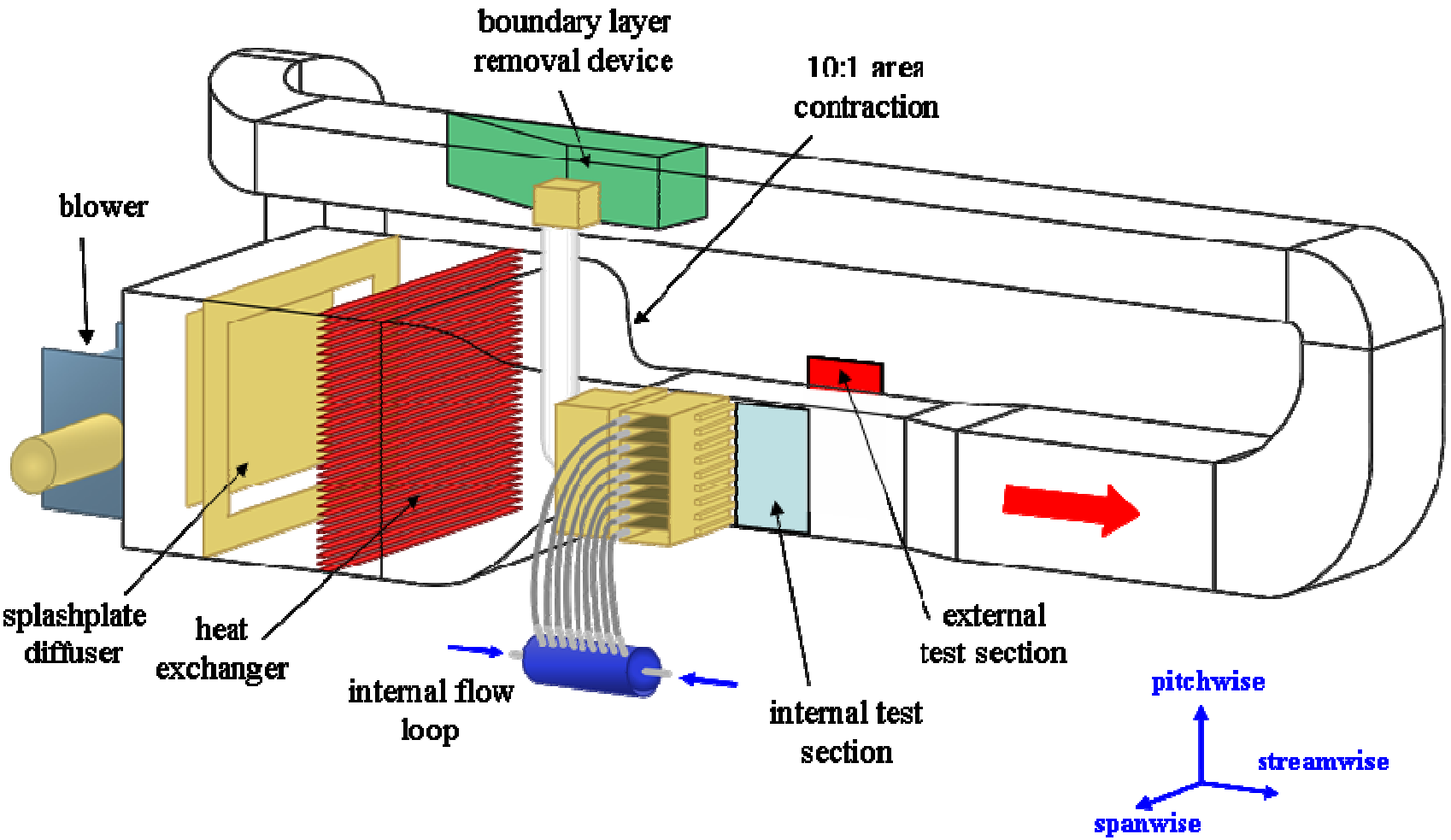

Figure 3-1. Combined internal and external test facility.

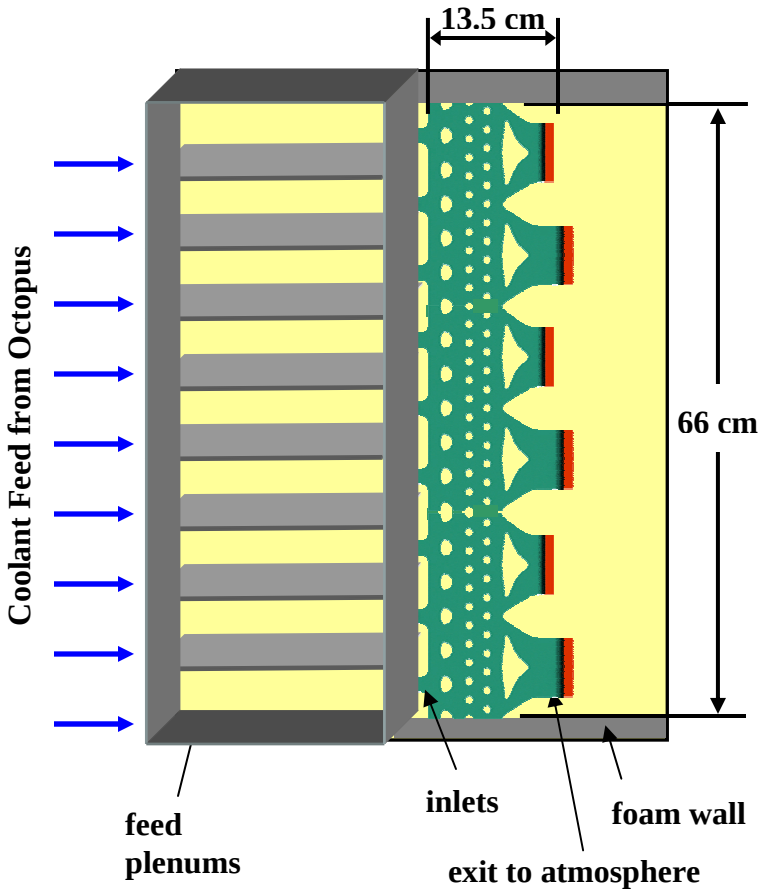

Figure 3-2. Cross section schematic of internal test section.

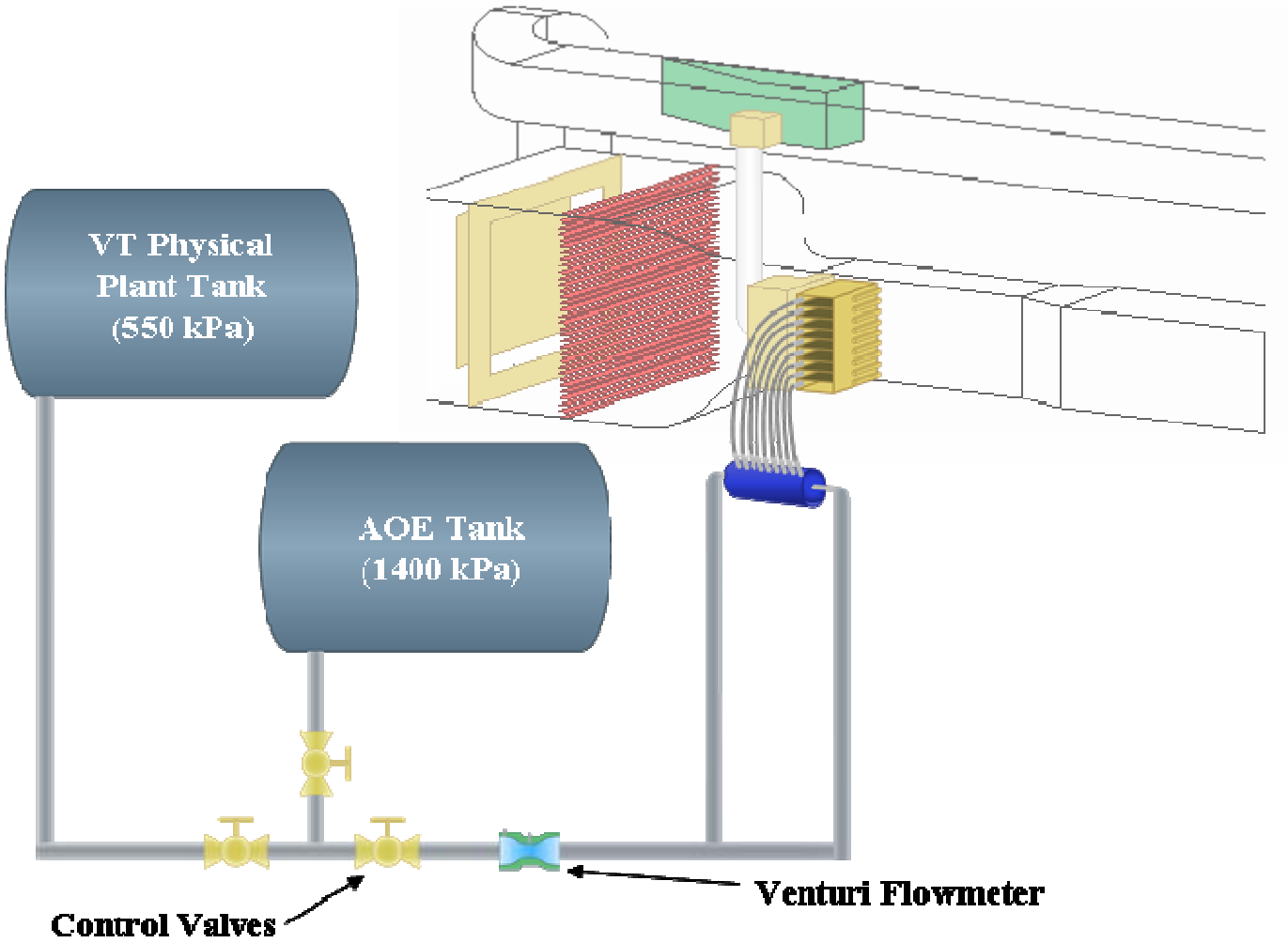

Figure 3-3. Coolant air sources and plenum feed schematic for internal cooling channel.

Figure 3-4. Octopus air tank used to control plenum feed flow. Air enters from above and below and exits evenly through the nine hoses.

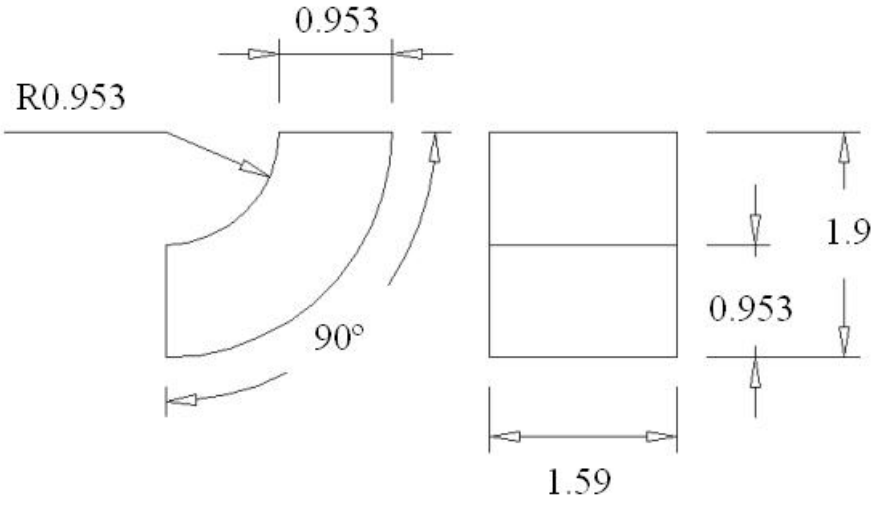

Figure 3-5. Inlet channel dimensions in cm.

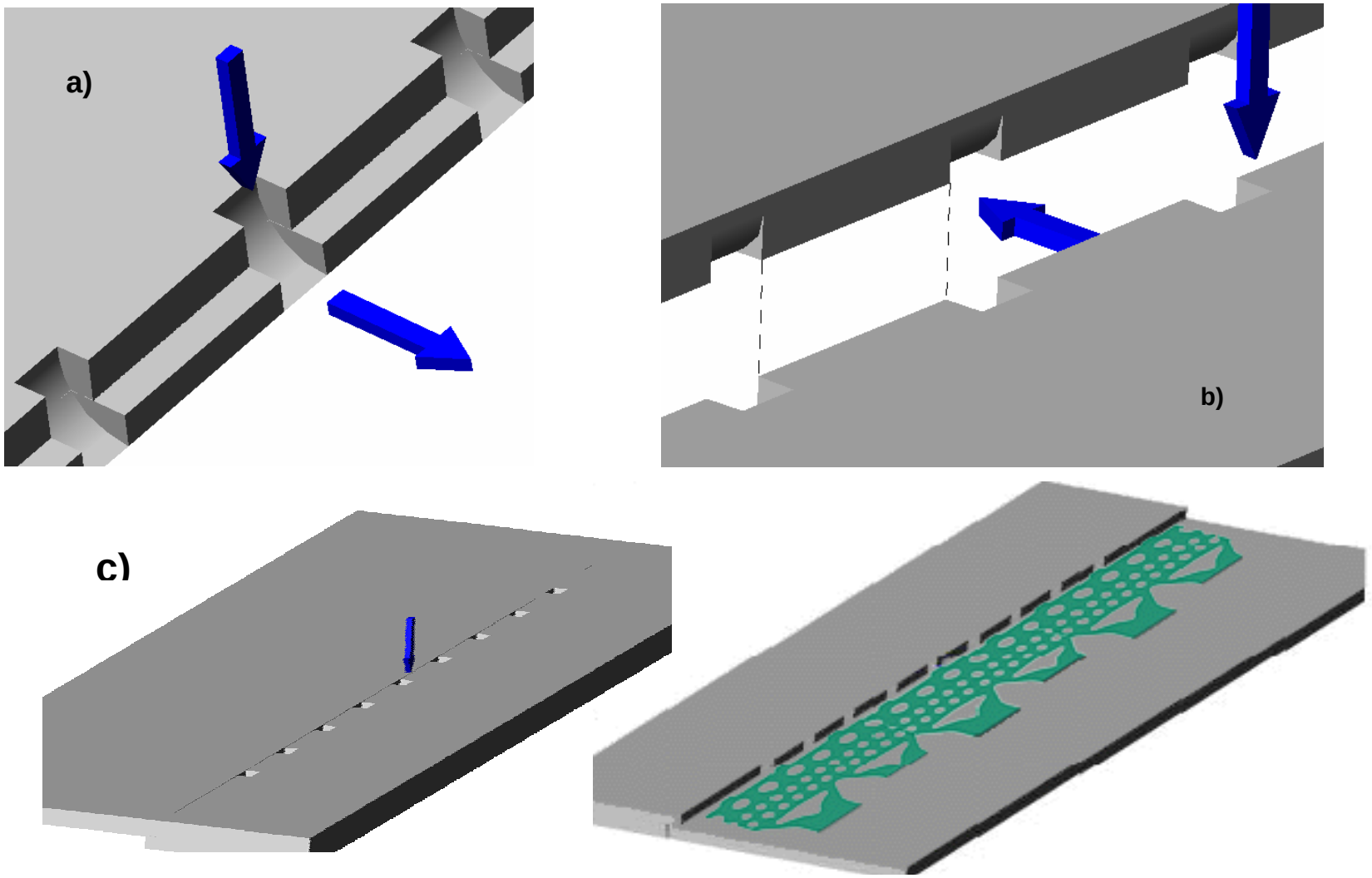

Figure 3-6 a) Concave inlet bend piece is shown, the coolant enters from the feed plenum and exits into the microcircuit b) convex inlet bend piece, shown above the concave piece c) completed inlet bend part from top (left) and bottom (right).

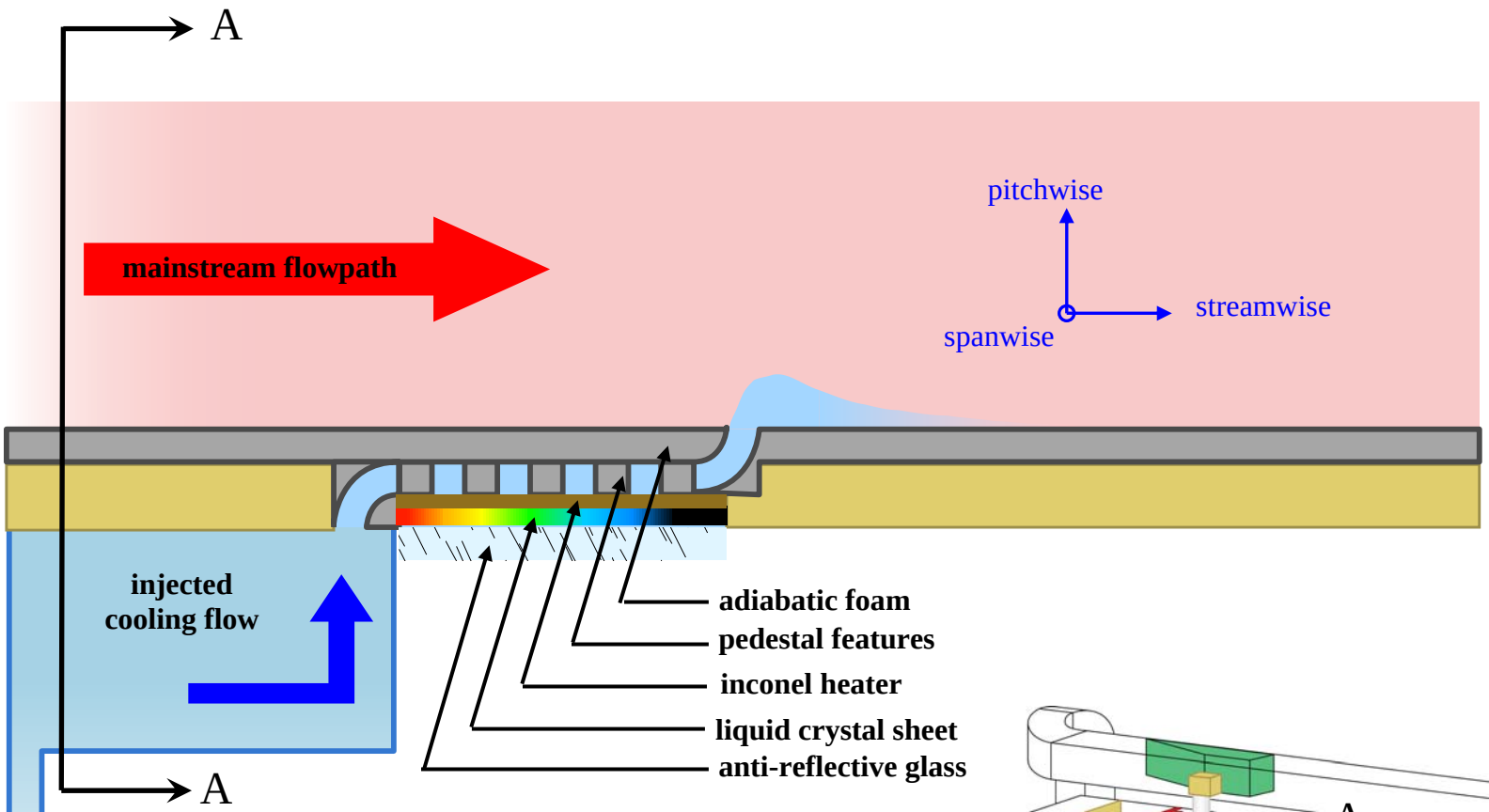

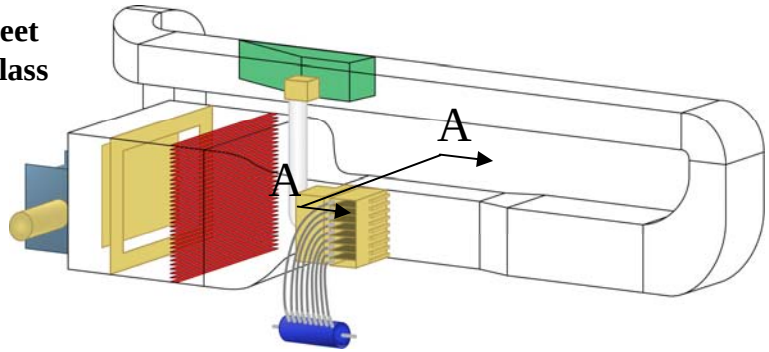

Component	Thickness
adiabatic foam	9.5 mm
pedestal features	9.5 mm
inconel heater	1.6 mm
liquid crystal sheet	0.8 mm
anti-reflective glass	9.5 mm

Figure 3.7. Cross-sectional view of test section.

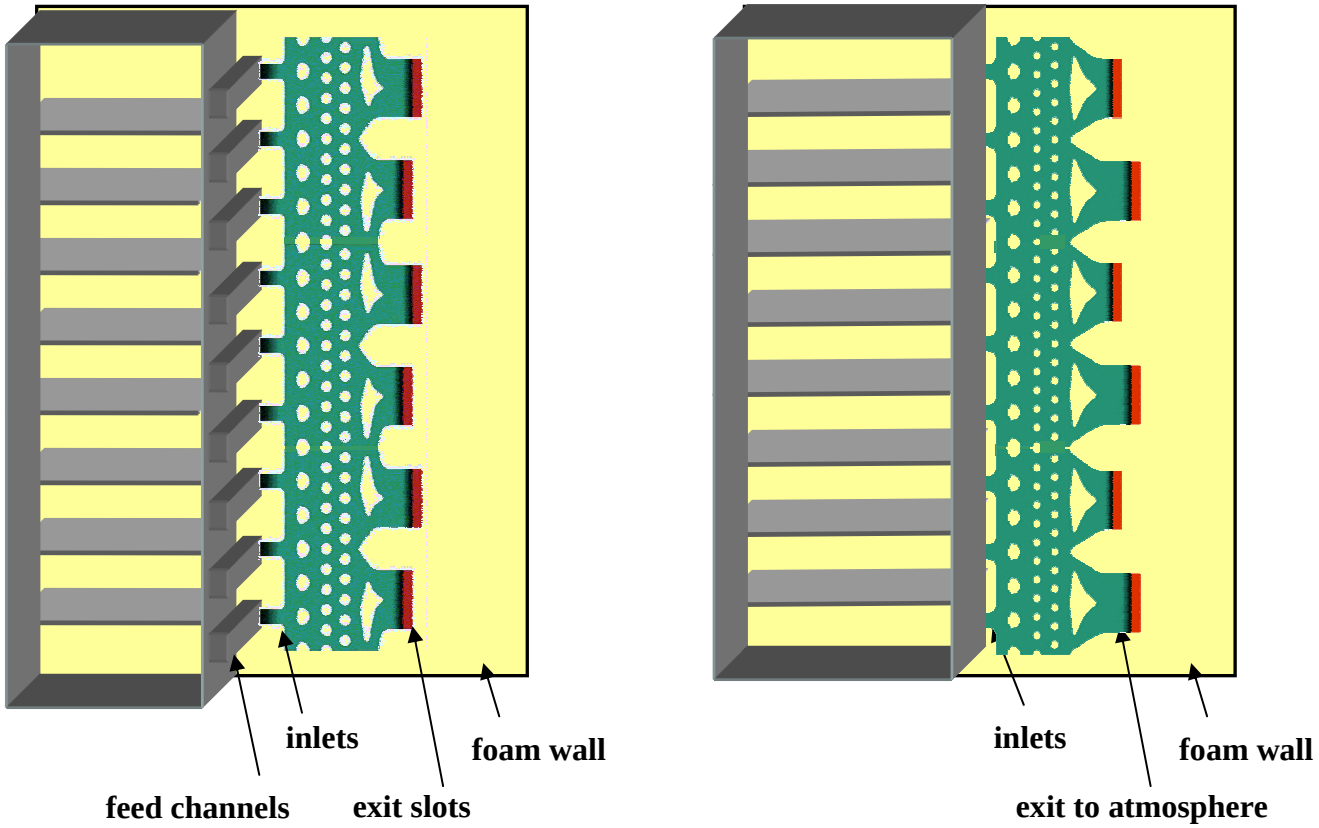

Figure 3-8. The contiguous arrangement of the three microcircuits is shown as well as the microcircuit feed channel redesign.

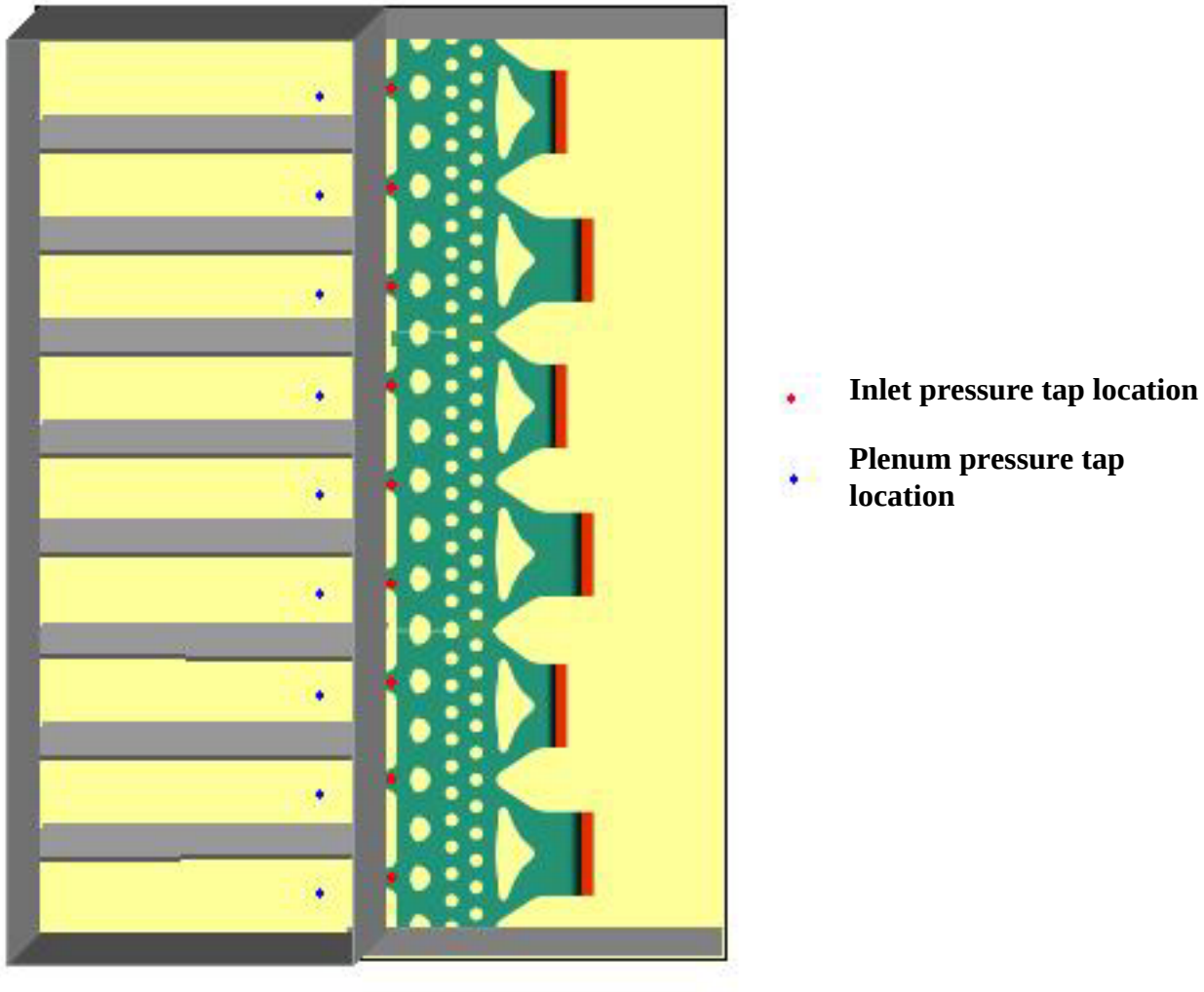

Figure 3-9. Pressure tap placement before and after reinstrumentation.

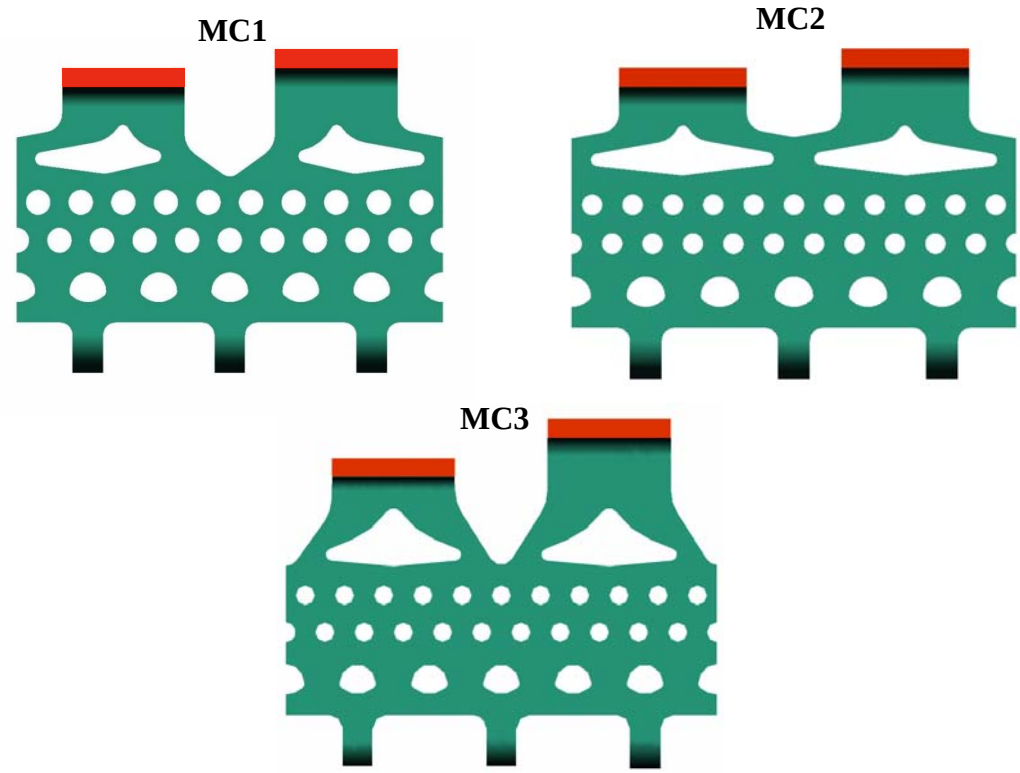

Figure 3-10. Microcircuit feature geometries.

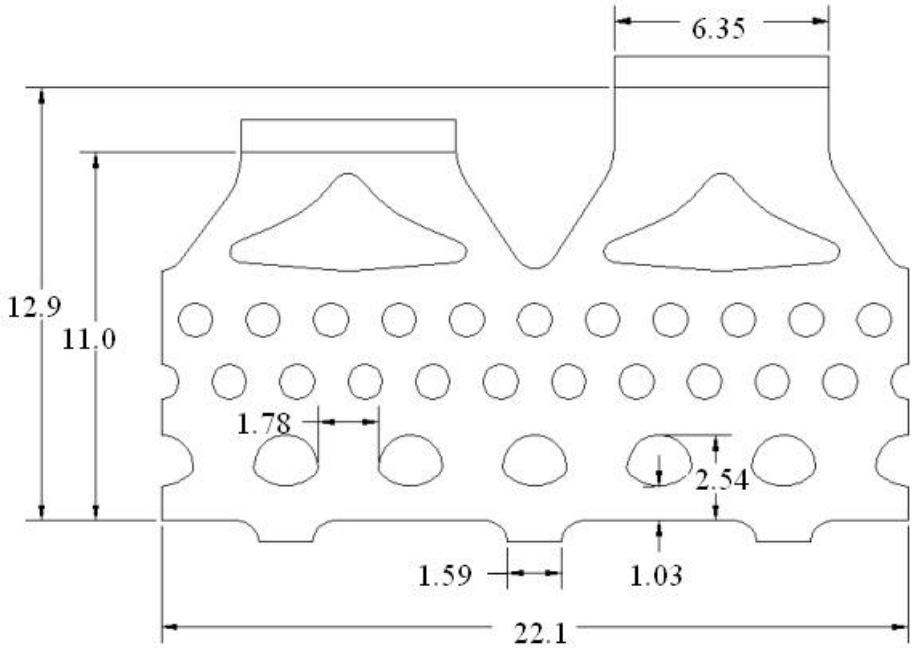

Figure 3-11. Microcircuit dimensions common to MC1, MC2, and MC3.

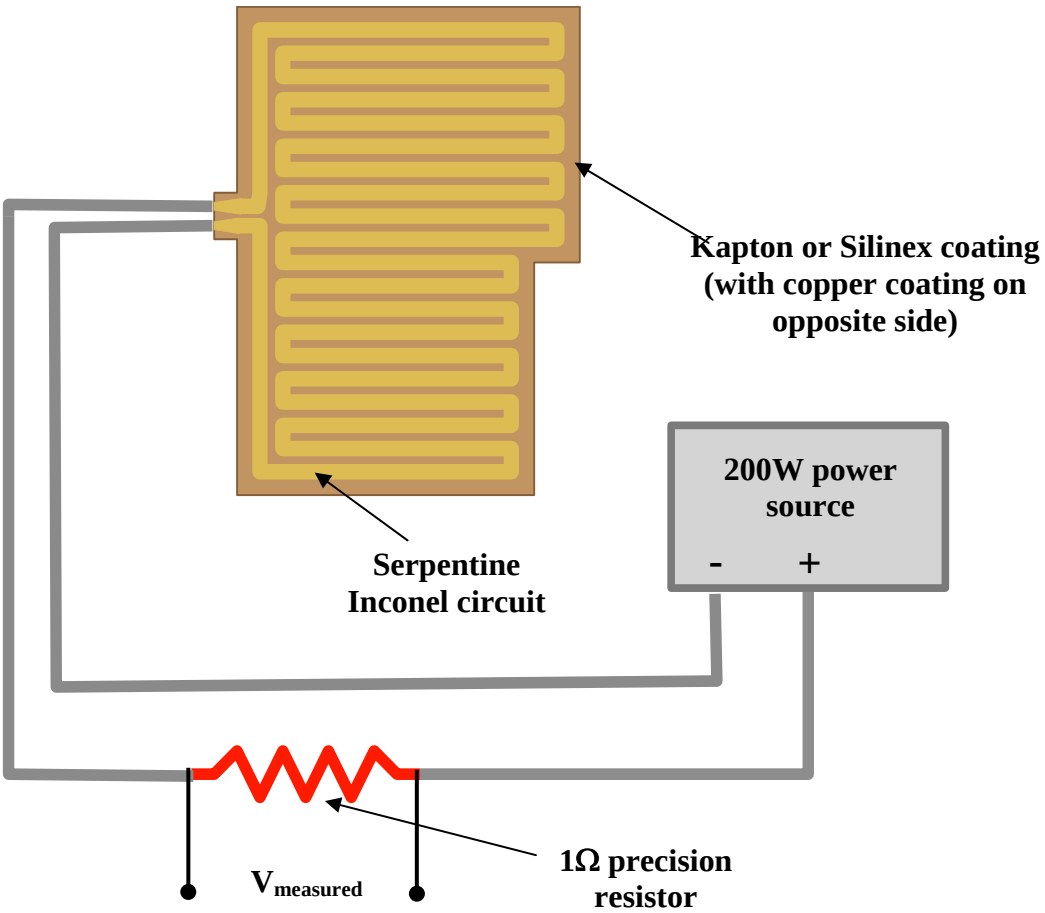

Figure 3-12. Heater circuit configuration.

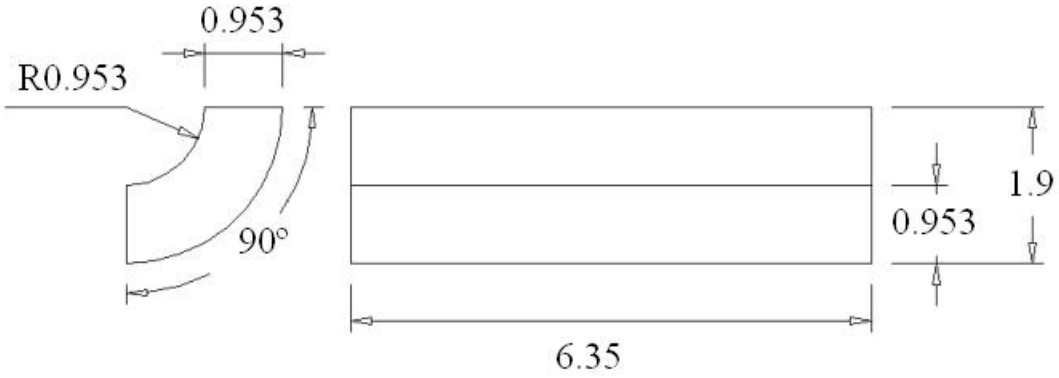

Figure 3-13. Microcircuit exit slot dimensions in cm.

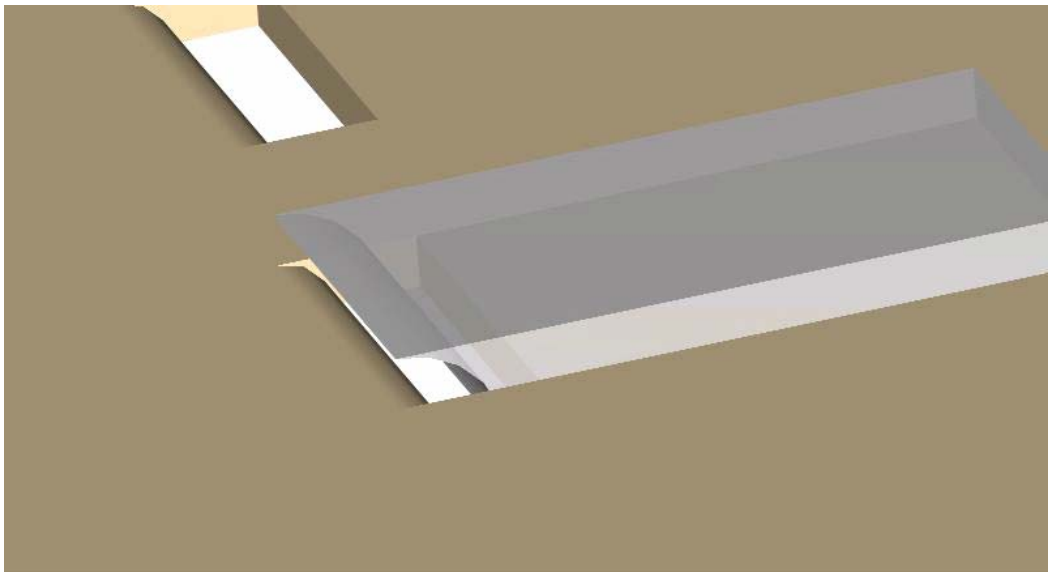

Figure 3-14. Exit slot geometry for microcircuits.

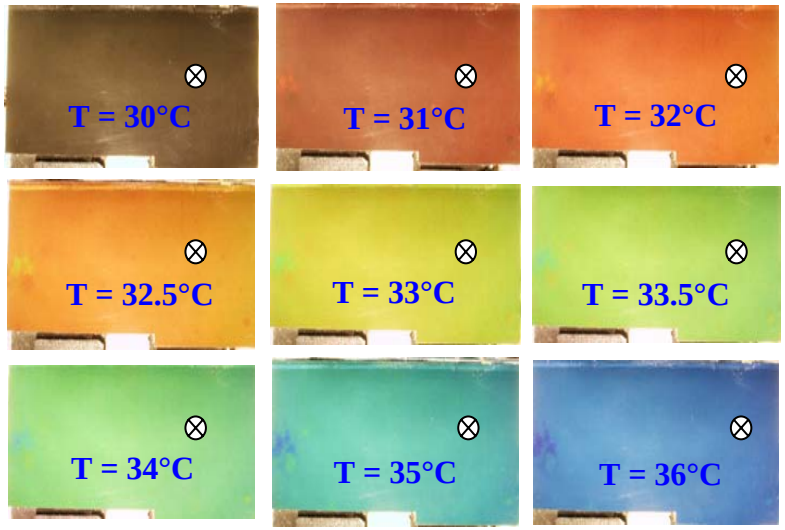

$$\mathrm{Hue}(R,G,B) = \arctan\left(\frac{\sqrt{3}\cdot(G-B)}{2\cdot(R-G-B)}\right)$$

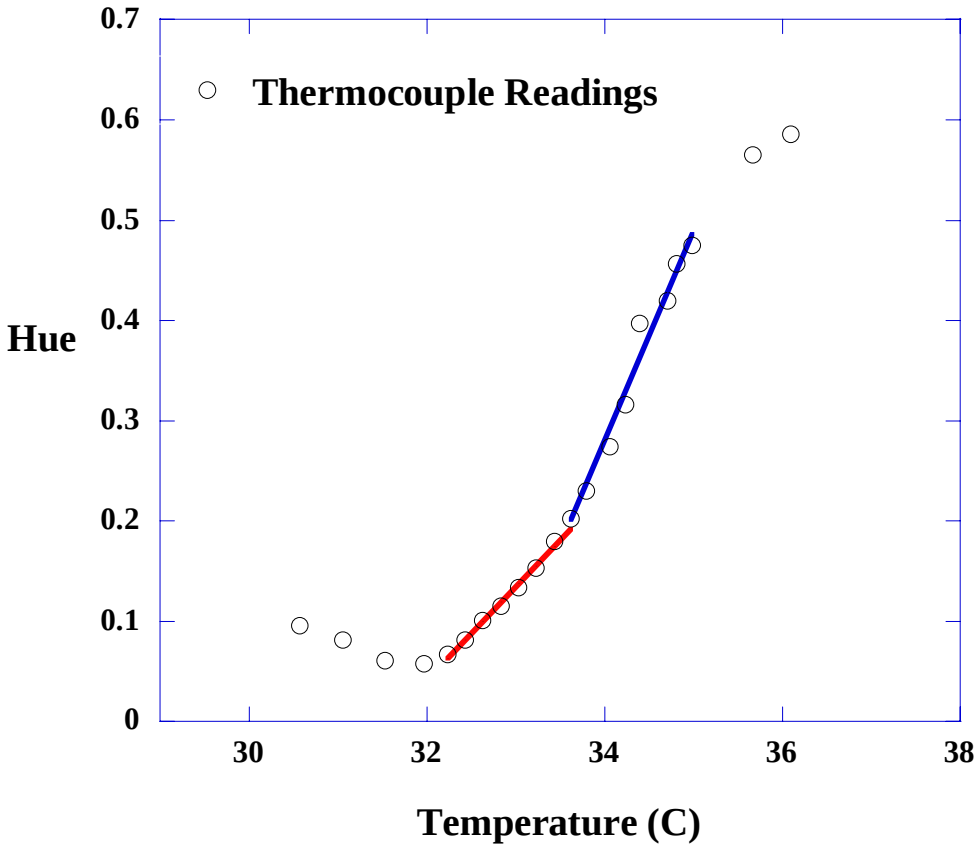

Figure 3-15. Hue to temperature calibration curve.

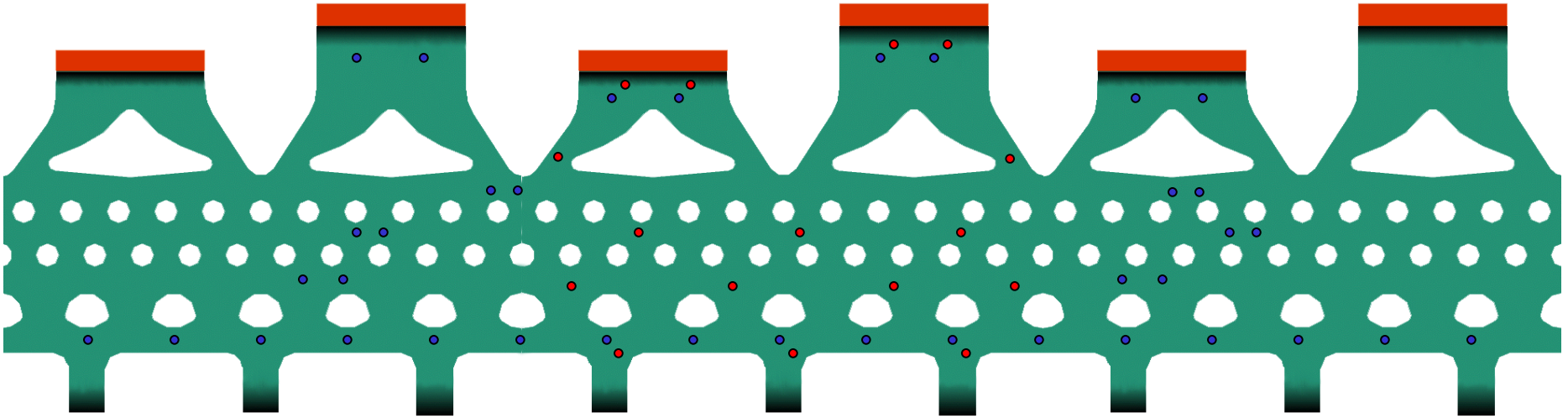

Figure 3-16. Microcircuit 3 pressure tap and thermocouple locations.

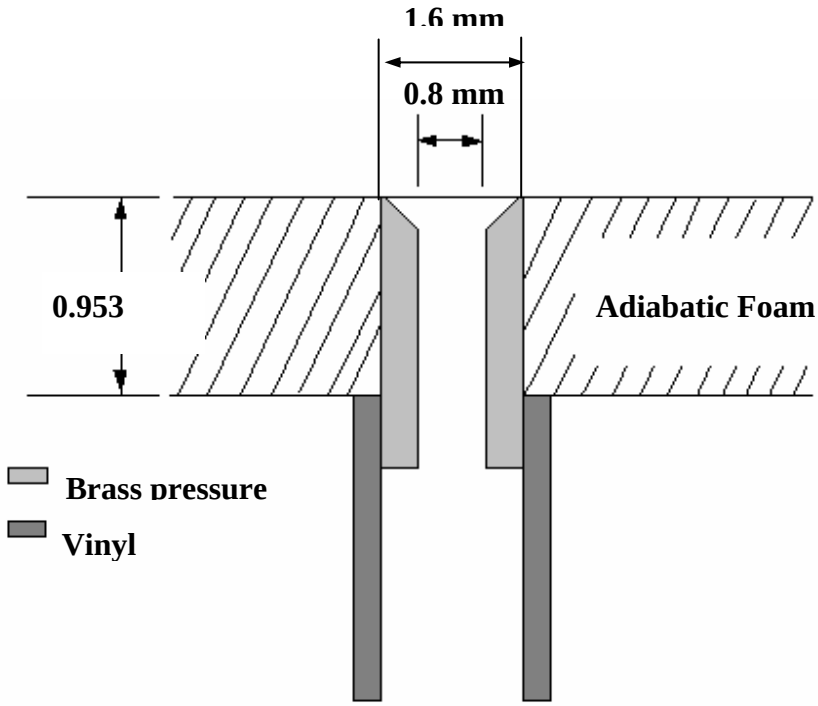

Figure 3-17. Pressure tap installation configuration [Couch, 2003].

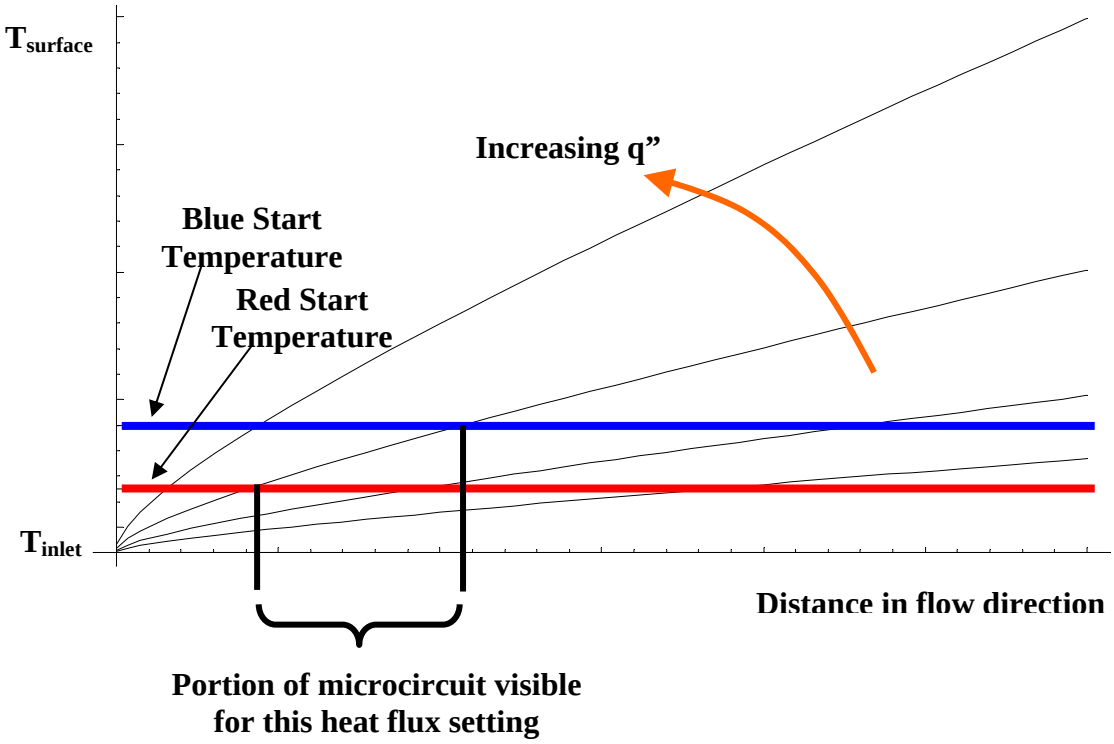

Figure 3-18. Liquid crystal measurable temperature range.

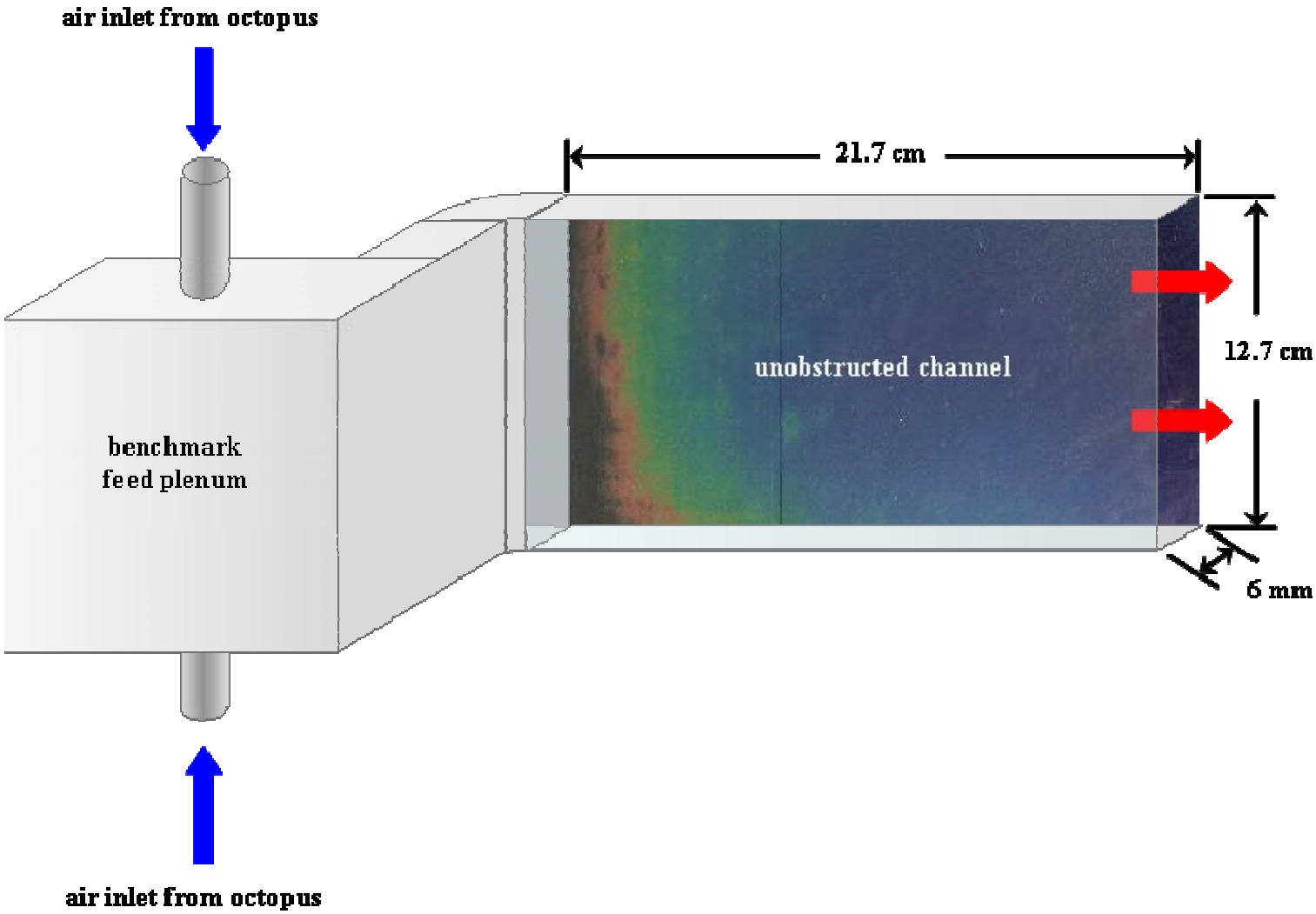

Figure 3-19. Internal benchmark test design.

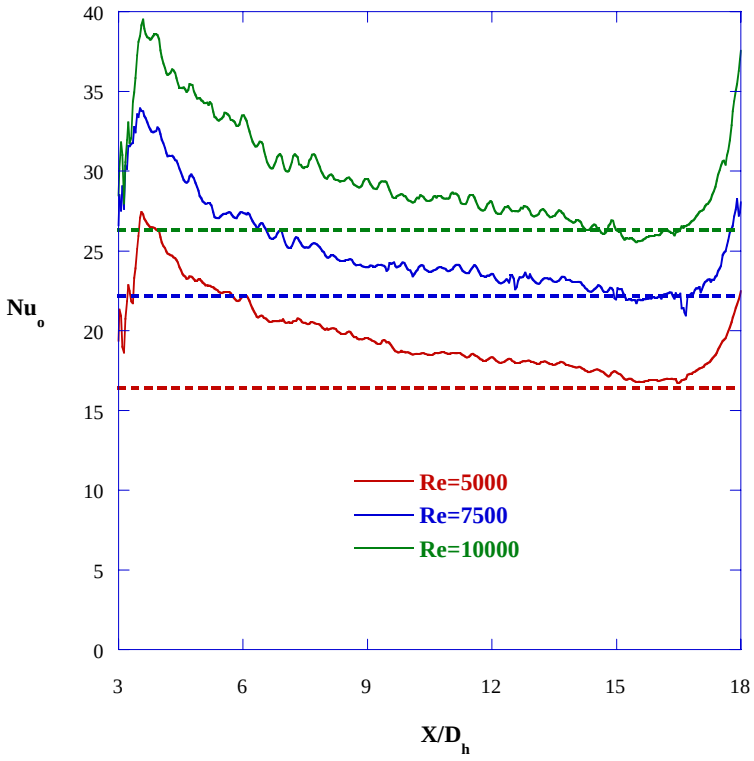

Figure 3-20. In benchmark testing, Nusselt numbers approach those of an open channel at fully developed values of X/D_h.

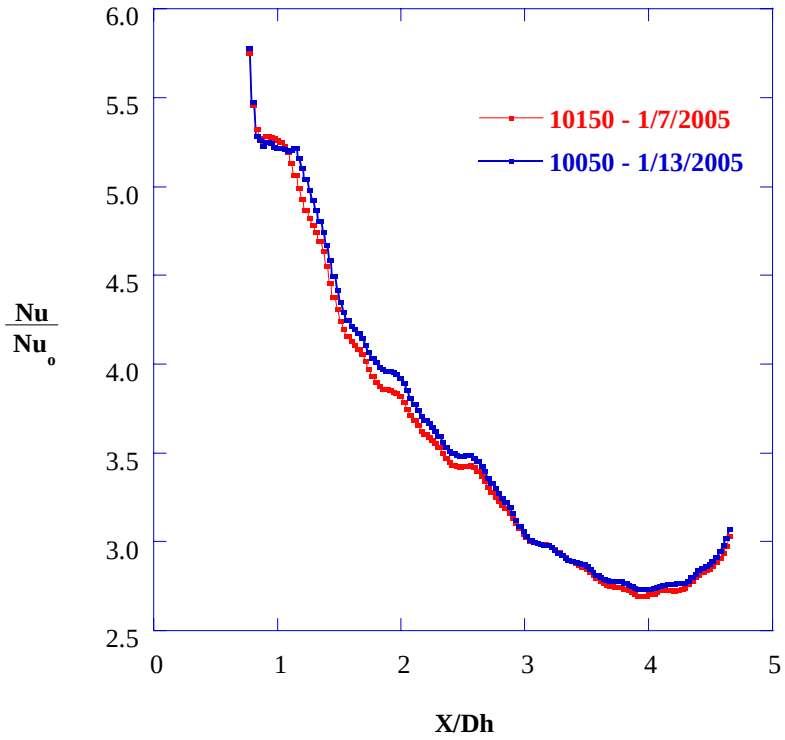

Figure 3-21. Internal benchmark testing repeatability test for MC3.

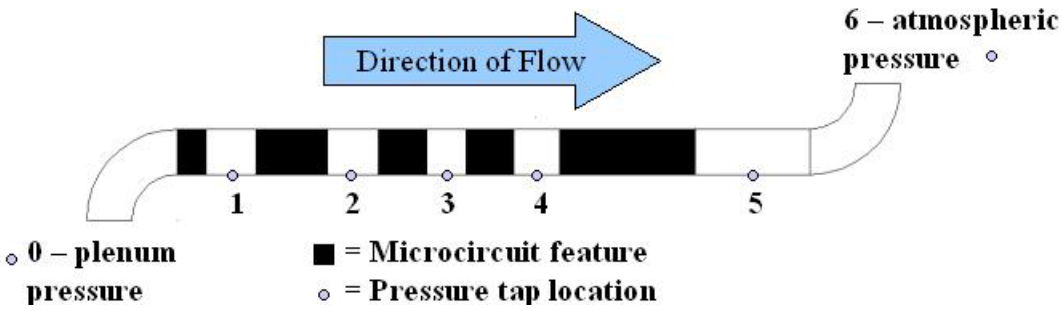

Figure 3-22. Pressure tap locations in streamwise direction.

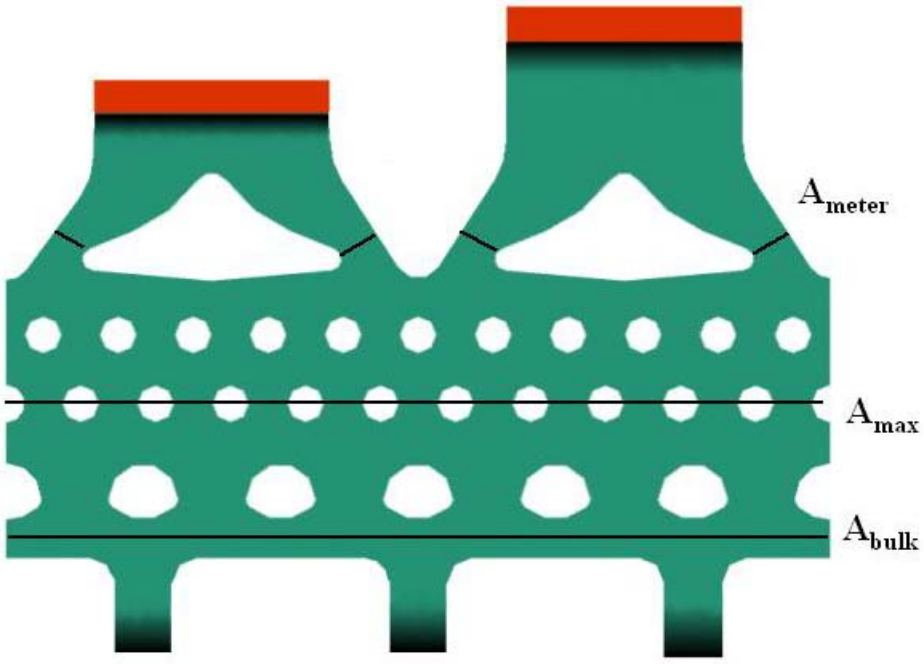

Figure 3-23. Flow areas used in the calculation of flow velocity

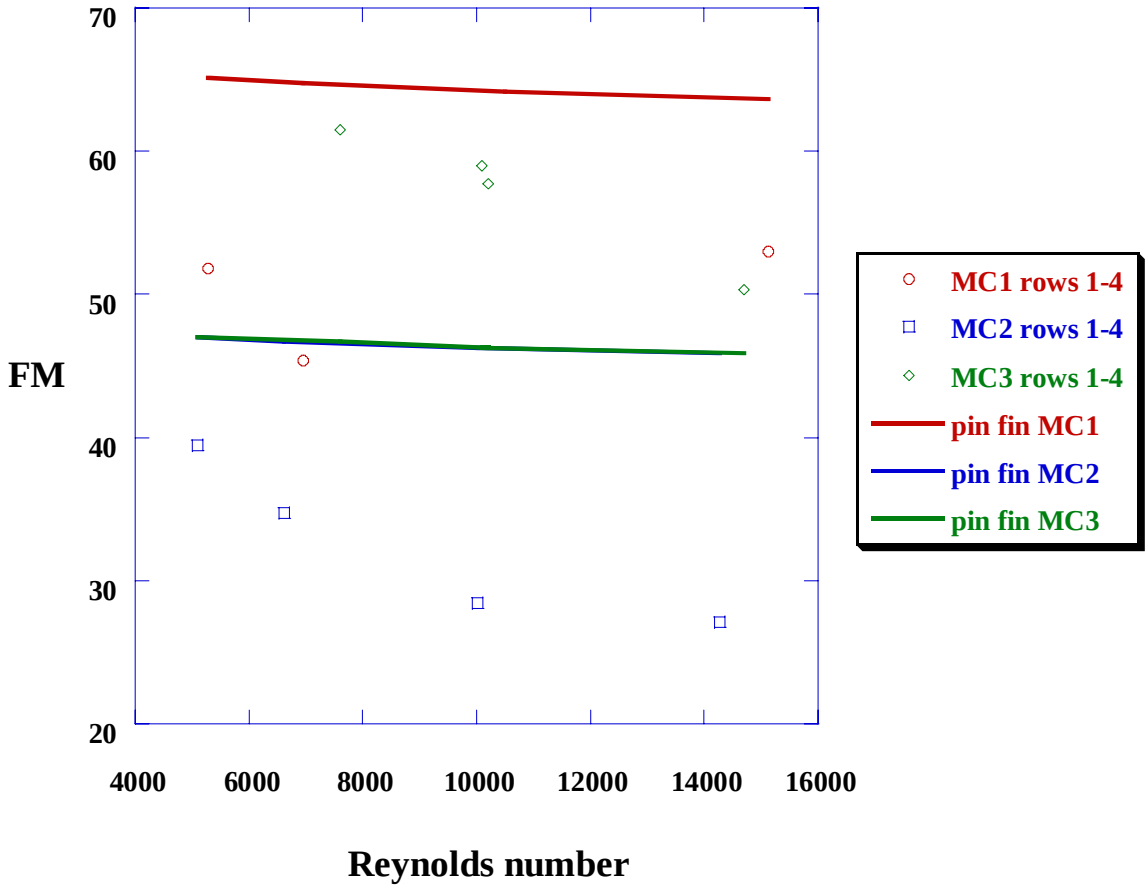

Figure 3-24. Friction multiplier benchmark results show trends in each microcircuit, but the trends are not in agreement with those predicted by the pin fin program.

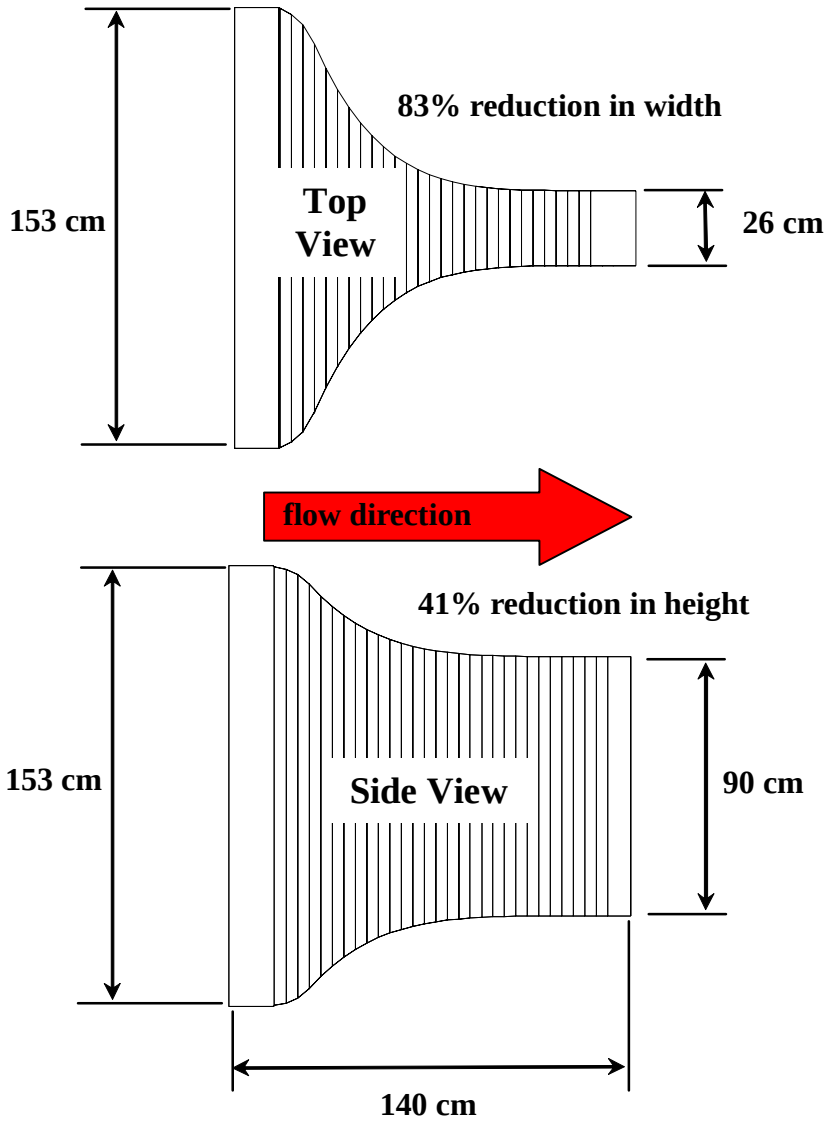

Figure 3-25. Contraction dimensions.

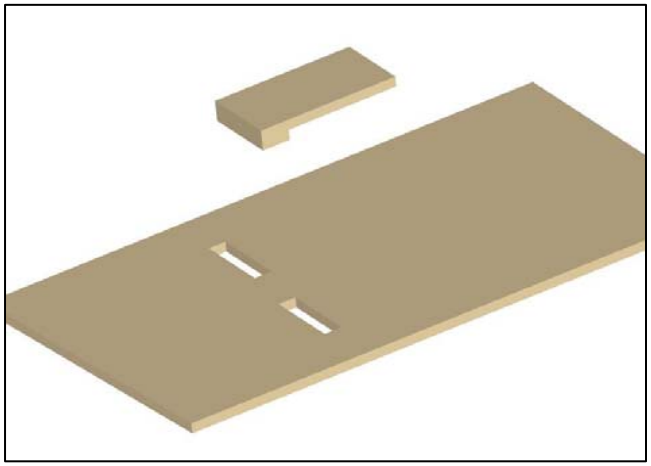

Step 1

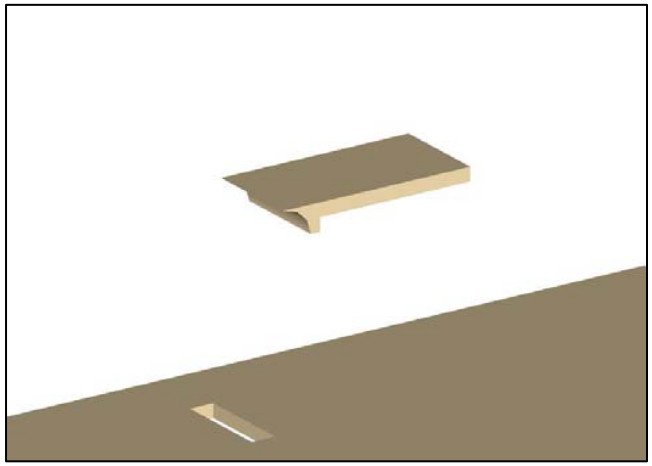

Step 2

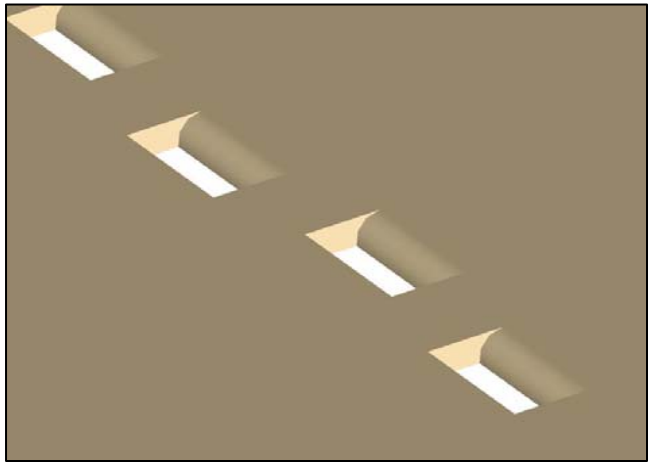

Step 3

Figure 3-26. Exit slot construction.

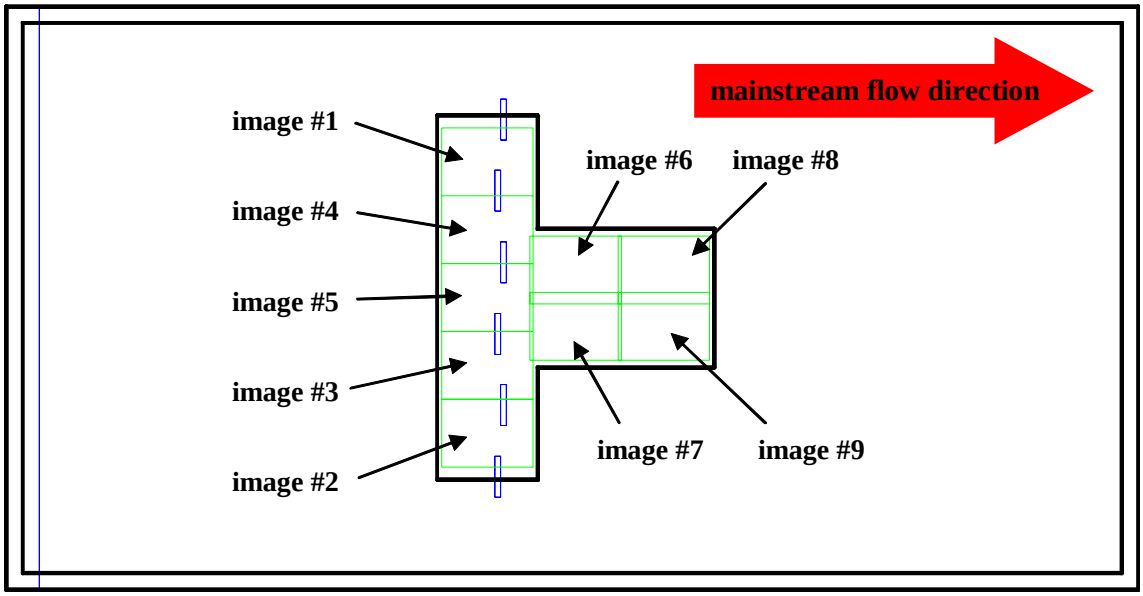

Figure 3-27. IR data collection image locations.

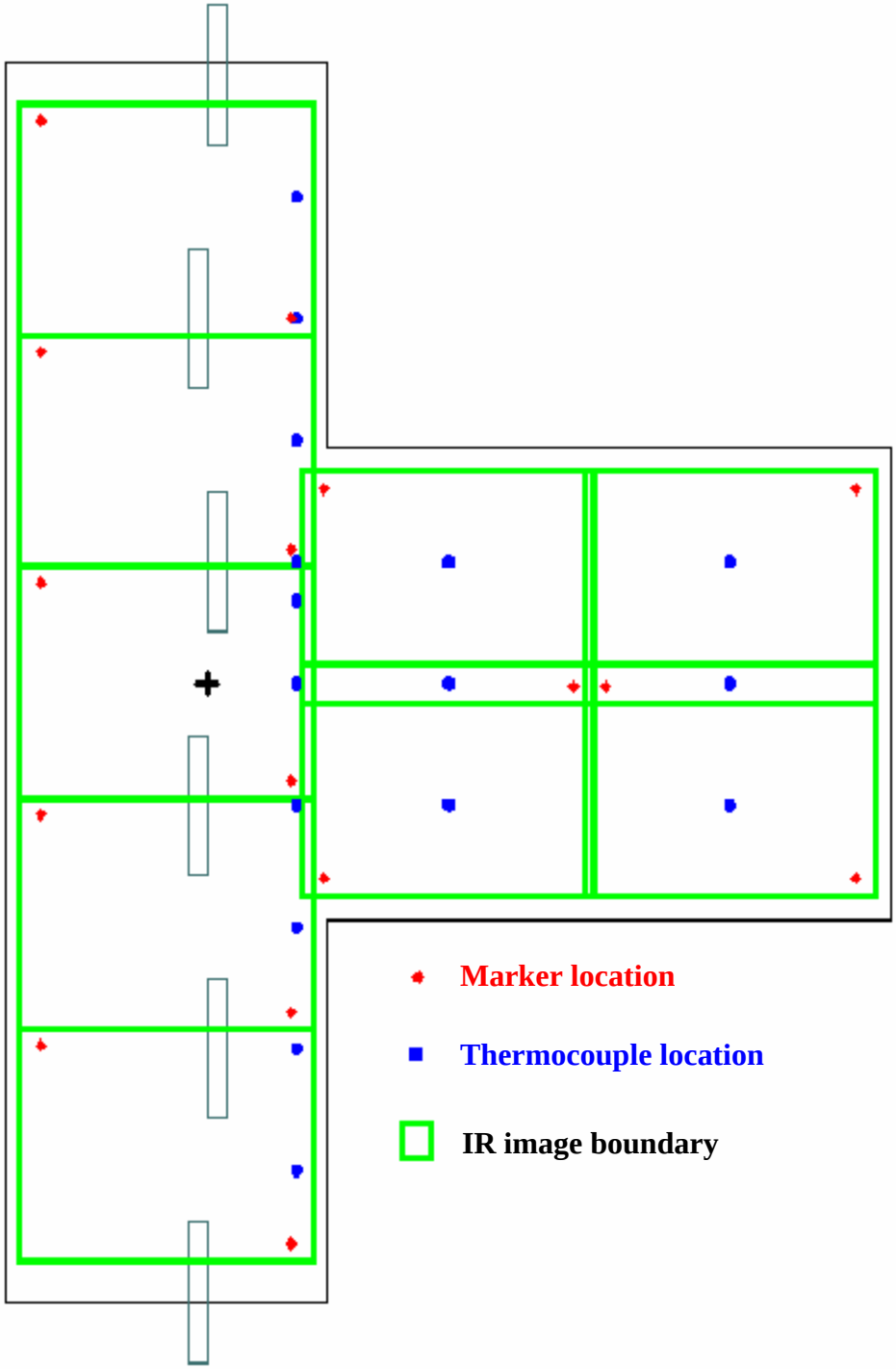

Figure 3-28. Thermocouple and marker locations for adiabatic effectiveness tests.

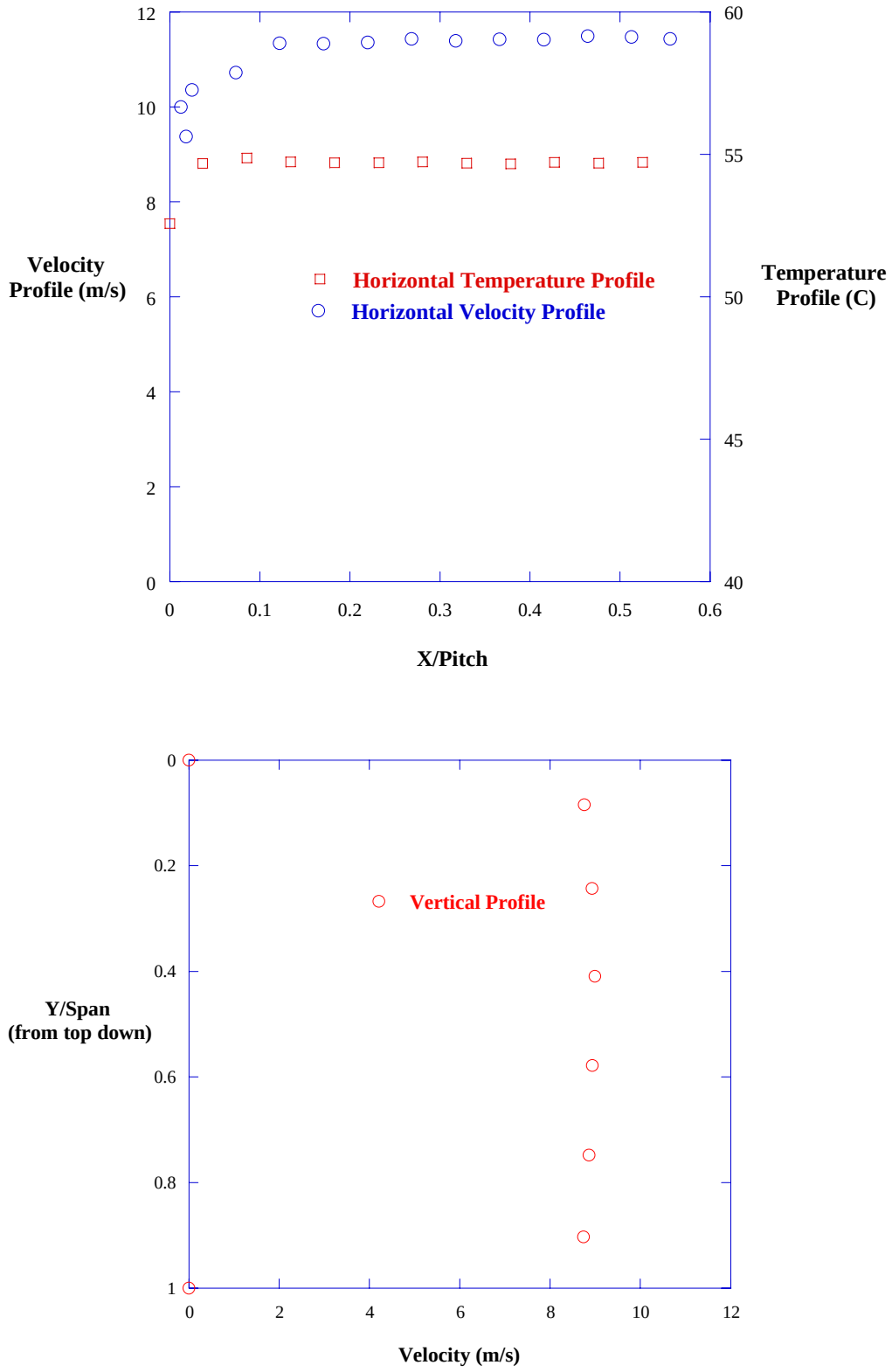

Figure 3-29. Mainstream temperature and velocity profile measurements.

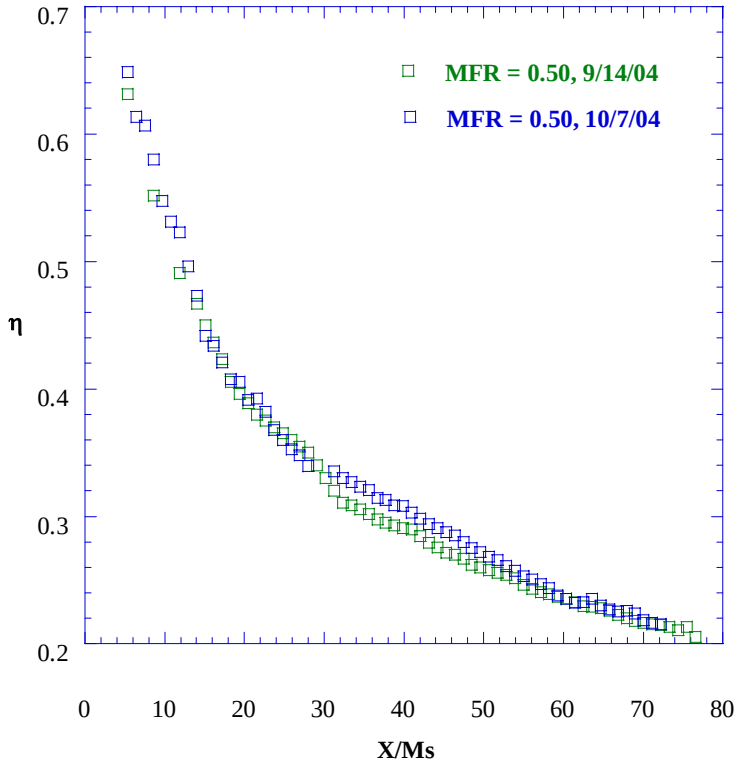

Figure 3-30. External repeatability testing shows similar results for data taken three weeks apart.

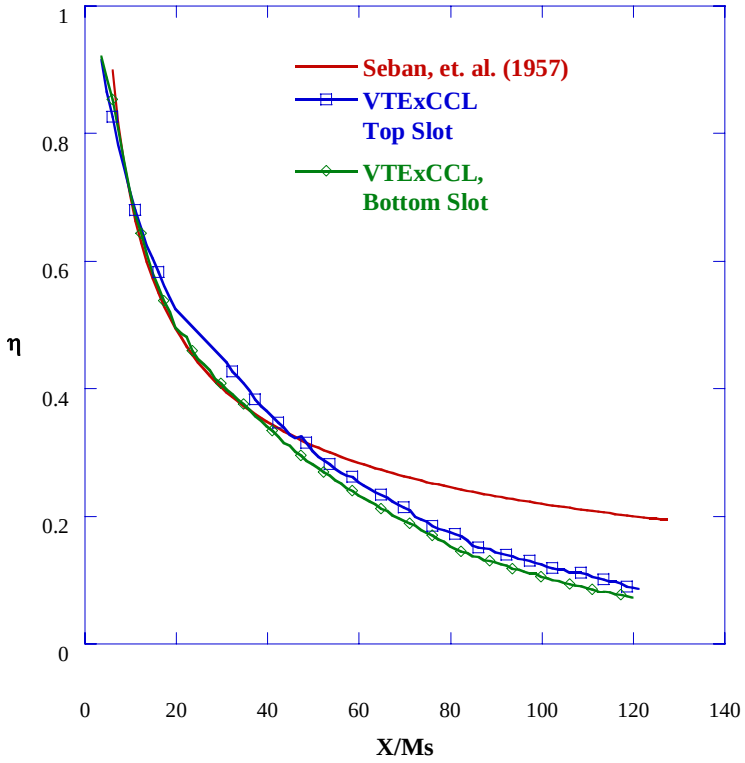

Figure 3-31. VTExCCL data agrees with Seban's results for a 90 degree slot at an MFR = 0.50.

Chapter 4
Data Reduction Methods

The data collection procedures employed in this testing included liquid crystallography and infrared thermography. The surface temperature data for the internal testing was collected in the form of hue values. The surface temperature data for external testing was collected in the form of radiation heat flux values. The application of calibration was necessary to convert the collected data into temperature contours.

This chapter will discuss the process of averaging images, extracting valid data, correcting for radiation and conduction, and applying calibration data to the internal data. The external data calibration and conduction correction procedures will also be discussed. A definition is also given for the friction factor augmentation and the efficiency index.

4.1 Liquid Crystal Image Processing

This section will discuss the use of Matlab to convert hue values, extracted from digital images, to temperatures. The initial step was the collection of calibration data as described in the section titled Liquid Crystal Calibration in Section 3.1. Matlab was used to create a linear correlation at each pixel location for the conversion of hue to temperature. The liquid crystal calibration data included a slope and intercept at each pixel location based on the hues measured on the copper block at 0.2°C temperature intervals as seen in Figure 3-15.

Several sets of data were combined to obtain a thermal contour of the surface as described in Section 3.1. Twelve images were taken for each heat flux setting to lower the precision uncertainty of the measured temperature values. The camera was secured to ensure that the same area was visible in each image. A set of example liquid crystal images with the respective heat flux values is shown in Figure 4-1. The linear color range of the liquid crystals is visible as green and red, and the pictures on the right show the valid data extracted from each of the images in blue. The pictures were taken such

that the entire surface area is covered in a color linearly related to hue in at least one of the pictures. By compiling these pictures, valid data can be extracted at every point on the surface. Figure 4-2 is a contour of the number of occurrences of valid data at each pixel location. This figure shows that valid data is available at each pixel location and multiple data points are available at over half of the pixel locations. The valid hue data two dimensional matrices were then placed in a three dimensional matrix with each level corresponding to a heat flux setting. The original digital image is stored in RGB values. The hue values were derived from the RGB values using the following formula.

$$\text{hue}(H,S,V) \equiv \arctan\left(\frac{\sqrt{3}(G-B)}{2(R-G-B)}\right) \tag{4.1}$$

The matrix of slopes and the matrix of intercepts was applied to each pixel in the three dimensional matrix to convert the matrix to a matrix of valid temperatures as shown in Equation 4.2.

$$T_w = \text{Hue} \cdot \text{Slope} + \text{Offset} \tag{4.2}$$

Conversion to heat transfer coefficients is necessary for compilation of the data. Heat transfer coefficient, h, is determined based on Equation 4.3.

$$q''_{\text{convection}} = h(T_w - T_c) \tag{4.3}$$

where, h is the heat transfer coefficient, $q''_{\text{convection}}$ represents the power supplied to the heater minus a conduction correction, T_w is the wall temperature as measured by the liquid crystals, and T_c is the local coolant temperature.

The value for $q''_{\text{convection}}$ is the amount of heat flux to the heater after the heat lost to conduction is accounted for. The conduction to be subtracted off was calculated according to Equation 4.4.

$$q''_{\text{cond}} = \frac{T_w - T_{\text{ambient}}}{\frac{1}{h_{\text{ambient}}} + \frac{t}{k}} \tag{4.4}$$

where, T_w is the liquid crystal surface temperature, $T_{ambient}$ is the room temperature, $h_{ambient}$ is the heat transfer of still air (5 W/m^2K), t (0.953 cm) is the thickness of the glass separating the heater from the room air, and k (1.4 W/mK) is the heat transfer coefficient of the glass.

Equation 4.3 is evaluated at each pixel location to obtain a heat transfer coefficient as discussed in Section 3.1. The values measured for (T_w - T_c) and $q''_{convection}$ are related by the heat transfer coefficient, by definition. As a result the heat transfer coefficients measured in the channel should be consistent for different values of (T_w - T_c) and $q''_{convection}$. At this point the heat transfer coefficients on the various levels of the matrix are equivalent and can be meshed into one continuous contour of heat transfer coefficients. A stack of data is compiled at each pixel location. If more than one heat transfer coefficient value was measured at each pixel location, then the values are averaged together. A two dimensional matrix of heat transfer coefficients is the final product of this process.

The heat transfer coefficients were converted to non-dimensional Nusselt numbers for comparison with the literature. The equation for Nusselt number is shown below:

$$Nu = \frac{h \cdot D_H}{k} \tag{4.5}$$

where h is the heat transfer coefficient, D_H (1.91 cm) is the hydraulic diameter of the channel, and k is the thermal conductivity of the fluid, in this case air. The hydraulic diameter was competed as four times the flow area over the channel perimeter and is approximately two times the height of the channel. The hydraulic diameter is a useful parameter for comparing the heat transfer characteristics of channels of differing geometries.

Residual data had to be removed from some of the data sets due to the hue change characteristics of the liquid crystal. The hue would change from black to red to green to blue and would eventually back to black. The hue values increased as the color changed from red to green to blue, but the hue value dropped drastically in the change from blue to black as shown in Figure 4-3. As the hue crossed the brink from blue to black a thin

band of random values was visible as shown in Figure 4-4. This artificial band of data was removed manually using the roifill command in Matlab.

Nusselt number augmentation due to channel features is commonly recorded in literature and was calculated for data comparison. The augmentation is the measured Nusselt number divided by the Nusselt number expected for an open channel of the same dimensions. A curve fit of Kays and Crawford's [1980] Nusselt number for unobstructed channel flow was used as the baseline Nusselt number. This correlation is for a channel with a constant heat flux on one side and with all other walls being adiabatic. The baseline Nusselt number correlation is shown below:

$$Nu_0 = 0.0285 \cdot Re^{0.75} \tag{4.6}$$

where, the Reynolds number velocity is based the velocity that the air travels in the open portion of the channel (U_{bulk}).

4.2 Infrared Image Processing

Infrared imaging provides a contour of radiation heat flux along a surface for conversion to temperature values. This method was used to determine the external wall temperatures after the coolant flow exited the slot to the mainstream. The following equation was used to calculate adiabatic effectiveness (η)

$$\eta = \frac{T_\infty - T_{AW}}{T_\infty - T_C} \tag{4.7}$$

where, T_∞ is the mainstream temperature, T_{AW} is the surface temperature, and T_C is the coolant temperature. The mainstream and coolant temperatures were collected using thermocouples, and the external wall temperatures were derived from the infrared images after calibration.

The infrared camera provides precise information about temperature difference, but without calibration, the camera does not accurately measure temperature magnitudes. Thermocouple measurements were taken in conjunction with the infrared imaging. The

images were then imported into ThermaCAM IFA300 version 4.5 for calibration. As discussed in Chapter 3, the absolute temperatures at the two thermocouple locations, one high temperature and one low temperature, were known, and adjustment of the emissivity and background temperatures allowed one to match the known temperatures to the temperature magnitudes at the thermocouple locations. The background temperature would shift both values maintaining the same temperature difference between the two, while the emissivity would change the scaling of temperature difference between the two thermocouple measurements. The changes in the emissivity and background temperature adjust the surface temperature, T, according to the following relationship:

$$T = \sqrt[4]{\frac{1}{\varepsilon \cdot \sigma}\left[q''_{rad} + (\varepsilon - 1) \cdot \sigma \cdot T_{bg}^4\right]} \tag{4.8}$$

where ε represents the surface emissivity, σ is the Botlzman Constant, and T_{bg} is the temperature of the environment surrounding the surface. q''_{rad} is the total radiation heat flux measured by the IR camera. When the mainstream temperature is 51.8°C, typical values for the parameters used in calibration are as follows: ε = 0.94, T_{bg} =76.5 °C. Conduction effects, generally on the order of 5% of heat flux, were also incorporated into the process of selecting suitable values for emissivity and background temperature as will be discussed further later in this section. After the selection of suitable values of background temperature and emissivity for each image, the images were exported from ThermaCAM as temperature matrices.

Adiabatic effectiveness is a measurement of the extent of cooling along the wall. A value of 0 for adiabatic effectiveness means that the mainstream temperature is the same temperature as the wall temperature, and that no cooling is occurring. A value of 1 for adiabatic effectiveness means that the wall temperature is the same as the coolant temperature and it is, therefore, being perfectly cooled. The values measured upstream of the slot, where no coolant flow was present, were around 0.2. A combination of effects resulted in the high measured values of effectiveness. While the assumption was made that the wall was adiabatic, this was not actually the case and conduction through the wall resulted in the development of a thermal boundary layer.

The Reynolds number of the mainstream flow was $4.1*10^5$ which is below the value for transition to turbulence of $5*10^5$. The velocity boundary layer can therefore be calculated using the following equation.

$$\frac{\delta}{x} = 4.92 \cdot \mathrm{Re}^{-(1/2)} \tag{4.9}$$

where δ is the height of the velocity boundary layer, x is the distance from the start of the boundary (71.4 cm), and the Reynolds number was calculated based on the distance from the boundary layer removal location to the slots. The velocity boundary layer at the slot location is 0.55 cm. This value can be used to calculate the thermal boundary layer height because the two are related by the following relationship.

$$\frac{\delta_t}{\delta} = \mathrm{Pr}^{(-1/3)} \tag{4.10}$$

where δ_t is the height of the thermal boundary layer and Pr is the Prandtl number of the mainstream fluid, in this case 0.72 for air. Based on this equation, the thermal boundary layer was 1.126 times the height of the velocity boundary layer, or 0.62 cm.

Theoretically, surface temperatures would be the same as the mainstream temperatures in adiabatic effectiveness testing. In actual testing, conduction and convection result in a deviation from the theoretical value. Conduction lowers the temperature of a thin boundary layer along the wall. As a result, air that contacted the surface was cooler than the actual mainstream temperature. Because η is a measurement of the film-cooling effectiveness it is desirable to isolate the effects of the film-cooling from conduction and convection. An analysis of the conduction through the wall (Appendix E) shows the temperature of the wall to be 0.8°C lower than the mainstream temperature due to conduction. The results of the lowered wall temperatures were the measurement of η values of around 0.125 upstream of the slot where no film-cooling effects were present. To isolate the effects of film-cooling this value needed to be 0 with no film-cooling.

As seen in the equation for η, for the η equation to equal 0, the values of T_{AW} and T_∞ need to be equal. The effects of conduction and convection of the slot were variable

based on test conditions, so to normalize all test conditions for comparison it was necessary to calibrate the images such that the wall temperature was set to the mainstream temperature. Initial calibration using the thermocouple values provided accurate values of emissivity, which determined the ΔT between the hot and cold values on the image. The background temperatures were used to shift the wall temperatures such that T_{AW} was equal to T_∞. This background shift generally resulted in a shift in T_{AW} of 4°C, which was equivalent to a decrease in eta of approximately 10%. A comparison of data before and after the correction is shown in Figure 4-5.

During testing of MC1 a different method was used to eliminate conduction effects. A set of adiabatic effectiveness data was taken with no coolant flow. The difference between the mainstream temperature and the wall temperature determined the amount of cooling by convection. The mainstream value was corrected using the following equation.

$$T_{\infty,\text{corrected}} = \frac{\eta_{0,\infty}(T_C) + T_\infty}{1 + \eta_{0,\infty}} \tag{4.11}$$

where $\eta_{0,\infty}$ = 0.125 is the experimentally measured upstream effectiveness with no cooling flow. The experimentally determined upstream effectiveness is an area average of conditions recorded during three experiments run at elevated temperatures with no cooling flow [Prausa, 2004]. The change from this method was made to incorporate convection effects into the correction, and MC1 data was reanalyzed using this method for comparison with current data.

Infrared image were taken at seven locations to capture the surface temperature contour for the two center slots for a distance of 30 slot widths downstream of the slot. Eight images were taken at each image location to minimize the uncertainty of the temperature measurements. The eight temperature matrices at each image location were exported from ThermaCAM and averaged in Matlab to make one average image. The conversion was then made to eta values using Equation 4.5. The matrices of eta values from the seven image locations were combined to create one matrix which in the form of an x and y value corresponding to each data point. The Matlab code used to combine the eta values into one matrix was developed in the VTExCCL lab by D. Knost and is

described in detail in Knost [2003]. The wall is instrumented with markers in opposite corners of each image. The brass markers, made of pressure tap tube, were placed flush with the surface and were visible in the images. The global locations of these markers were known, and a GUI allowed point and click selection of the marker name, global position, and the marker location. The eta values from the images were then compiled into one eta contour as shown in Figure 4-6.

The η contours often did not line up across the junction between pictures. Testing was completed to verify that a sufficient number of images was being taken to average out the flow fluctuations. A data set with 24 images per image location as compared to the standard of eight images per location. The data collected from this test was not significantly different than the taken with eight images per location. Based on this test the problem was found to be within the image compilation process. Slight discrepencies between the physical marker locations and global measurement locations were responsible for the misalignment, and adjustments in marker location values were made to ensure that contours were consistent across the picture breaks.

4.3 Pressure Data Analysis

Pressure taps were located throughout the test facility and were used to detect the local static pressure during internal and external testing as described in the Friction Factor Measurements of Chapter 3. Pressure is the driving force in moving air from the high pressure compressor through the turbine cooling channels. As a result, the driving pressure must not exceed the pressure available at the exit of the compressor. Friction factor is a critical value in microcircuit designs because the pressure drop through the channels, with small hydraulic diameters and large blockage features, are significantly higher than those measured in the pin fin and dimpled channels currently in use and it is necessary that the required pressure drop is not too large. The friction factor provides a dimensionless, scalable value representative of the frictional losses through the cooling channels. D'arcy friction factor and baseline friction factor values across the microcircuit were calculated as described in Chapter 3. The D'arcy friction factor was selected to simplify comparison to the pin fin program developed by Pratt and Whitney [Cunha,

2004]. A friction factor augmentation factor was defined as the measured friction factor divided by the baseline friction factor for an open channel of the same dimensions as was also described in Chapter 3.

An efficiency index represented the ratio between the heat transfer augmentation and the friction factor augmentation.

$$\text{Efficiency Index} = \frac{Nu/Nu_0}{f/f_0} \tag{4.12}$$

A high efficiency index would represent efficient use of the coolant air because a large cooling benefit would be achieved without a high friction factor penalty.

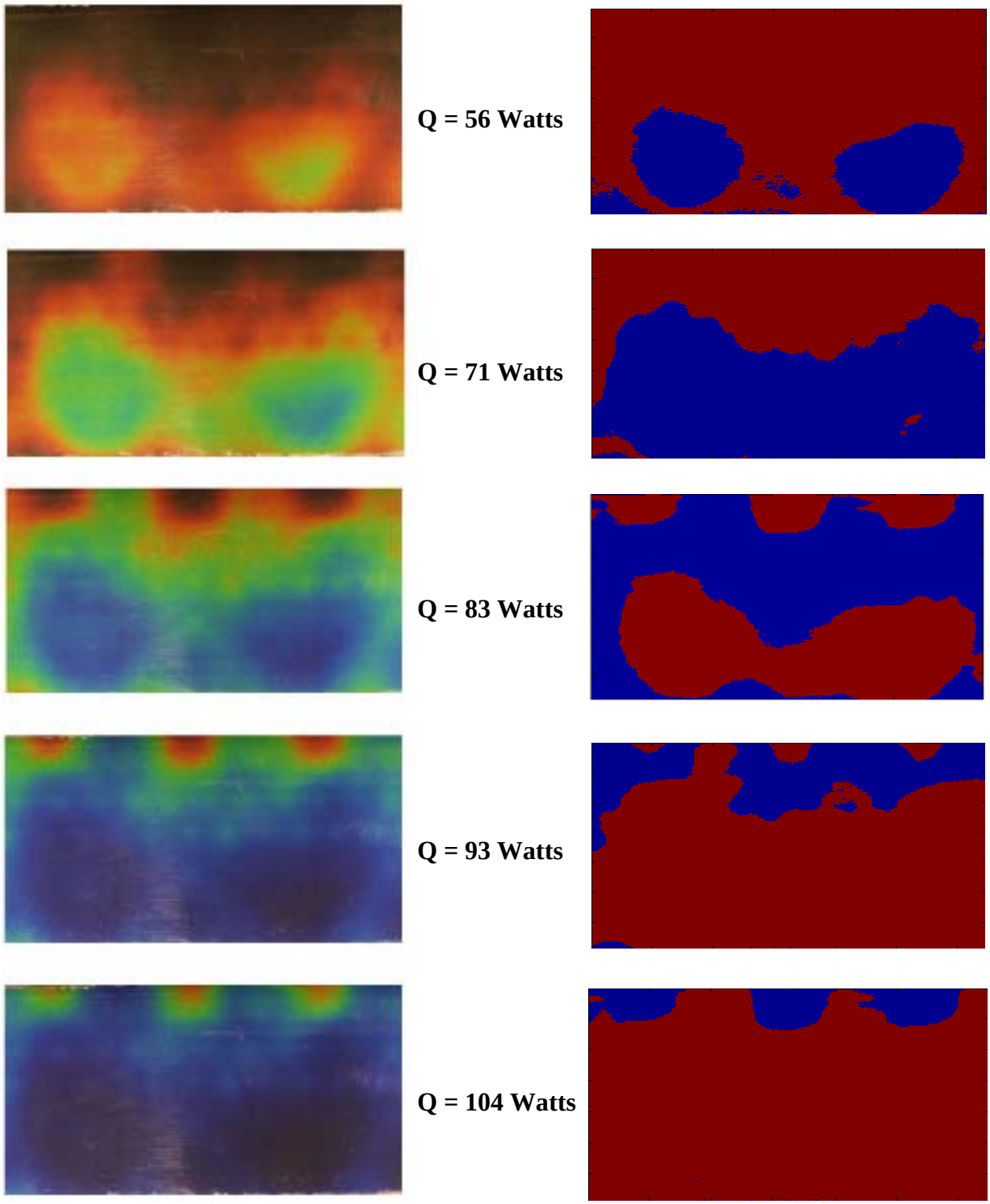

Figure 4-1. Liquid crystal surface for MC3 at selected values of heat input (Q), Re = 7500. Images on the right show the valid data selection range in blue.

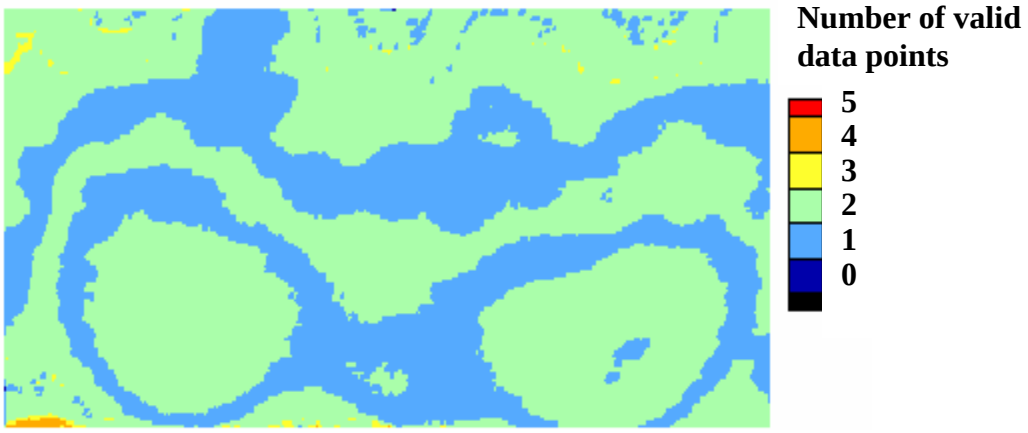

Figure 4-2. The number of data points averaged at each image location for MC3, Re = 7500 for the values of Q applied in Figure 4-1.

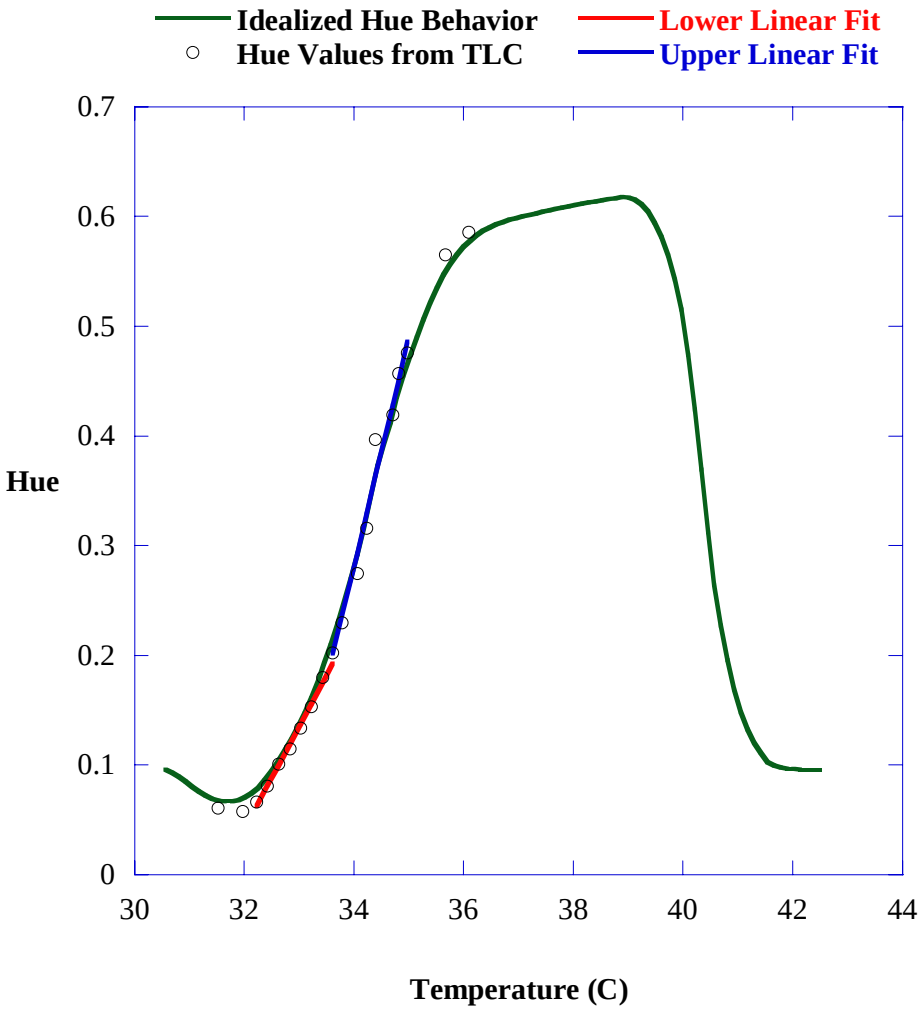

Figure 4-3. Hue versus temperature plot including theoretical transition from blue to black.

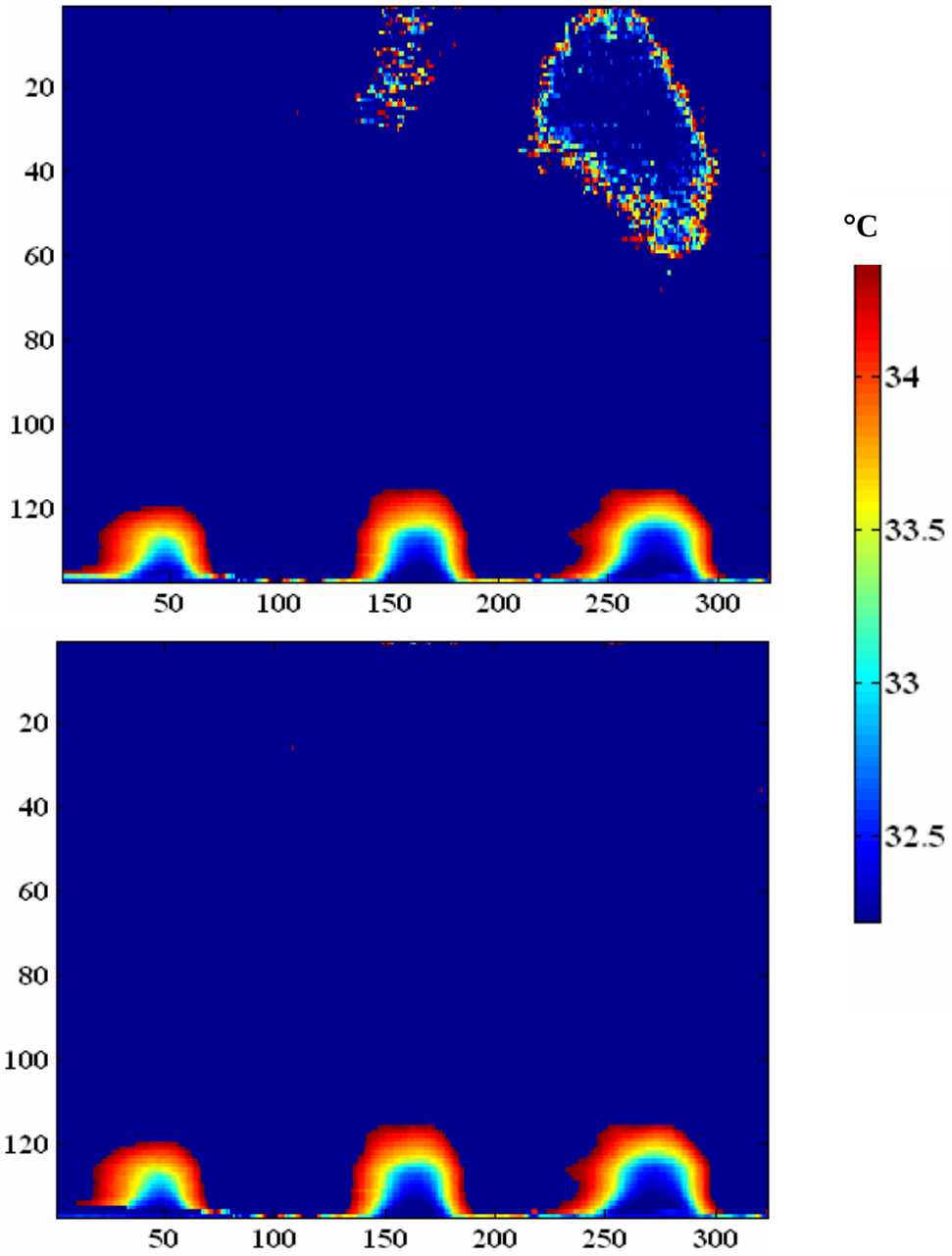

Figure 4-4. Removal of invalid data points was necessary due to the fact that the hues crossed back over the valid temperature range when moving from blue to black.

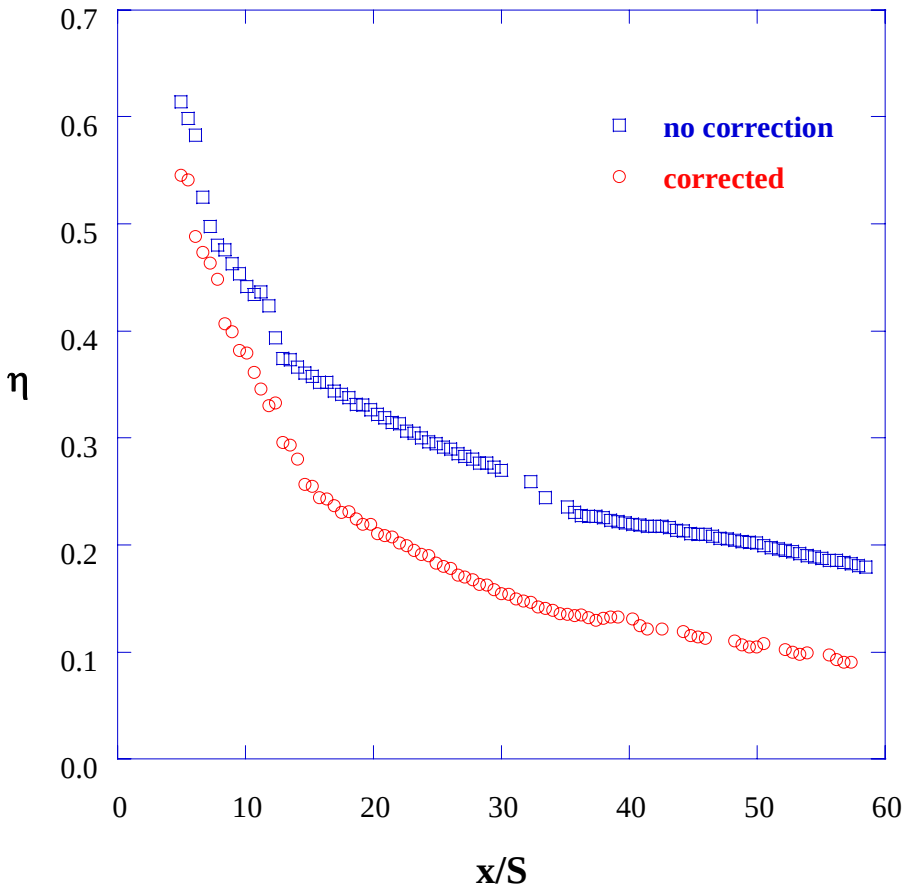

Figure 4-5. Comparison of conduction corrected and uncorrected values of average eta (MC3, MFR = 0.75).

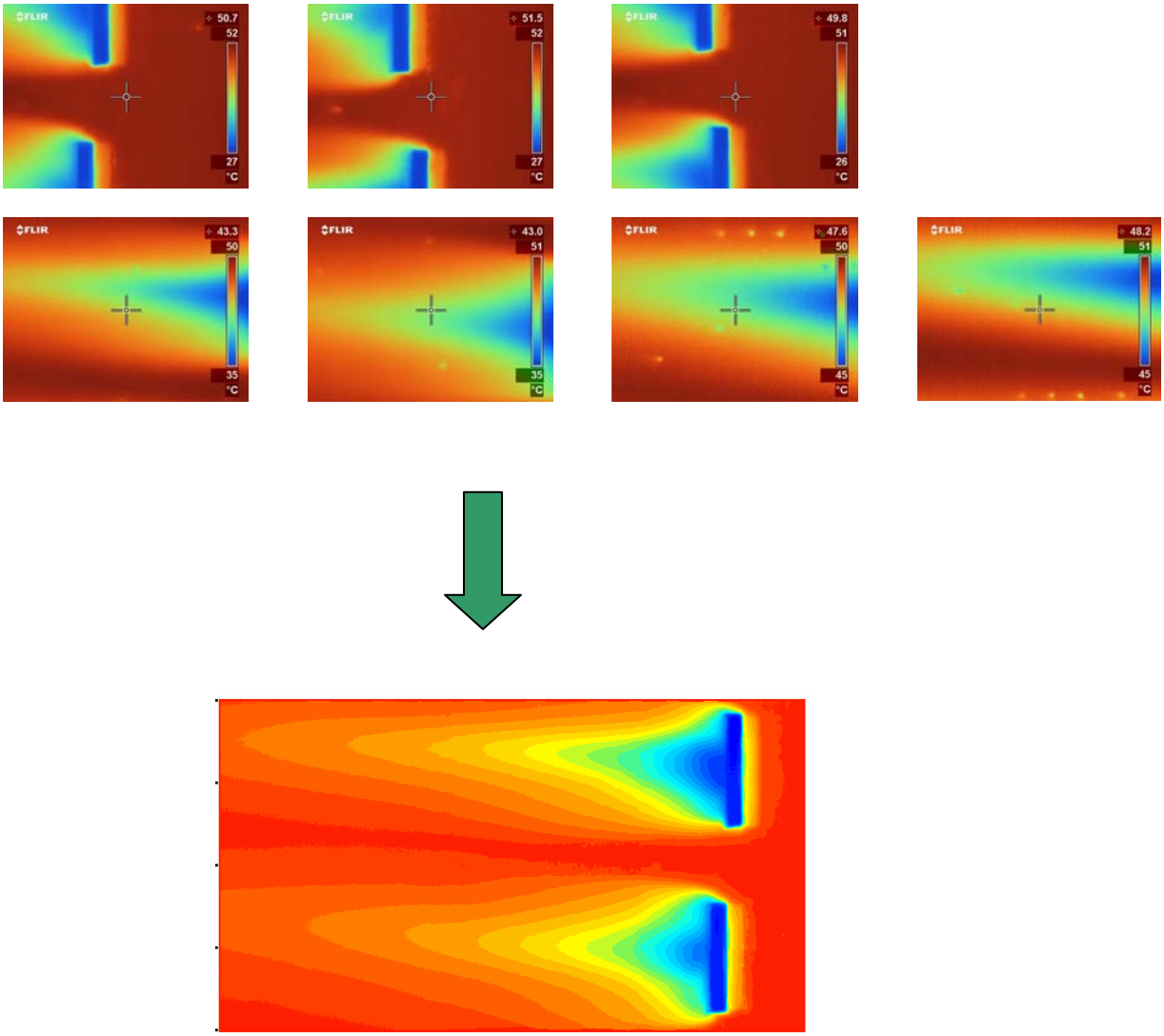

Figure 4-6. Individual IR images were compiled to obtain contours of eta for the middle two slots.

Chapter 5
Experimental Results

This chapter presents the comparative heat transfer and friction factor results for three microcircuit designs. Internal and external cooling are compared at different Reynolds numbers and blowing ratios for three microcircuit designs. The designs all result in similar cooling effectiveness externally, but considerable variation is seen among internal cooling in the microcircuit channels. The internal cooling is augmented most effectively for all geometries at the lowest Reynolds. Friction factor values for the three microcircuit designs vary significantly, with MC3 resulting in the best overall cooling augmentation to pressure loss ratio. This chapter will present these results in detail with internal heat transfer and friction factor data presented in section 5.1, friction factor results shown in section 5.2, and external adiabatic effectiveness measurements presented in section 5.3.

5.1 Internal Test Results

Internal heat transfer measurements are useful in pinpointing portions of the internal channel that are under-cooled. In this case the heat transfer measurements provide a means of comparing the heat transfer capabilities of differing designs. The heat transfer coefficients were non-dimensionalized to Nusselt numbers and these values were divided by the Nusselt number for an open channel at the same Reynolds number (as described in Chapter 4).

Comparison of three microcircuit designs. As was described in Chapter 3, the test design differed slightly for MC1 as compared to MC2 and MC3. MC1 pin fins were made of adiabatic foam to isolate convective cooling on the heater surface by eliminating the effects of conduction. Testing on MC2 and MC3 was completed using

copper pin fins. With copper features, fin effects become substantial since the walls of the copper fins are exposed to the convecting flow. The tests completed with copper features were closer to blade conditions than the adiabatic foam tests in MC1. The disadvantage of the change to copper features is that the copper pin fin features acted as heat sinks and the differences between the cooling in different areas of the microcircuit designs were obscured.

Figure 5-1 shows a spanwise average of the footprint of microcircuit features relative to the surface area of the channel walls. Values of one would occur if the area contained a fully blocked channel, and values of zero would occur if the duct was fully open with no pin fins. The resulting plot provides information on the ratio of $A_{blockage}$ to A_{total} along the microcircuit flowpath. In MC2 and MC3 this information is especially important to data analysis because of the pin effects in the conductive microcircuit features.

Figure 5-2 compares the contours of Nusselt number augmentation for all three microcircuit designs at a Reynolds number of 5300. The flow in these contours is moving from left to right. Due to the limitations of the data collection process, some data is missing from the MC1 contour. Nonetheless, it is evident that extensive impingement cooling is present at the MC1 inlet. The effect of the impingement varies among the designs with the most cooling visible near the inlets of MC1 and MC3. Figure 5-3 shows the spanwise averaged values of Nusselt number augmentation. In the cases with high impingement (MC1 and MC3), a significant decrease in the heat transfer is seen following the impingement region. The averaged values near the inlet of MC2 are artificially low because of the data that is missing from the high heat transfer areas.

Figure 5-4 compares the contours of Nusselt number augmentation at a Reynolds number of about 7500, and Figure 5-5 shows these same values averaged in the spanwise direction. Once again MC1 and MC3 see high cooling due to impingement at the inlets. The data near the inlet was collected for MC1 in this case making a comparison of inlet conditions possible. In the contours of MC1 the cooled area circumnavigates the first feature and then separates from the feature. In the MC3 contour, the jet cools the feature itself, and the feature absorbs heat by conduction. This difference is due to the change in feature material from adiabatic foam to thermally conductive copper.

The insulative pins in MC1 also eliminate pin effects in the downstream pins. In MC2 and MC3 the convective heat transfer surface area is higher than that in MC1 because the pins move heat into the convective flow. Therefore in MC2 and MC3 the cooling downstream of the impingement is contributed to by the pin effects of the thermally conductive pins. In MC1, conduction does not occur in the foam pedestals because the thermally insulative material serves to isolate the heat transfer to only convective heat transfer on the heated wall.

Figures 5-6 and 5-7 present the Nusselt number augmentation values at Reynolds numbers of around 10,000. The averaged values show that the impingement augmentation measured in MC1 has overtaken that measured in MC3. Figures 5-8 and 5-9 show the same trend for Reynolds numbers of around 15,000. Note the scale change in the contours for these two cases.

The metering area is the smallest location in the microcircuit flow path. The metering area occurs at the feature just upstream of the slot in all of the microcircuit designs. A comparison of the metering areas of the three microcircuits is shown in Table 3-1. The microcircuit designs in order of smallest to largest metering areas are as follows: MC2, MC3, and MC1. Notice that at the high values of Reynolds number the impingement effects follow the same trend with MC2 seeing the least impingement cooling and MC1 seeing the most. While other effects may contribute to the differences in impingement among the microcircuits, it is probable that a smaller metering area decreases the effects of impingement cooling, especially at high Reynolds numbers.

The spanwise averaged values of Nusselt number augmentation are shown along the streamwise direction in Figure 5-10 for all Reynolds number cases. A characteristic curve is discernible for each microcircuit. In other words, the cooling patterns in the cooling channel are a function of the feature shapes in the channel and scale with Reynolds number. MC2 is relatively constant across the flow path, while the values measured in MC1 and MC3 are more variable. MC1 and MC3 see high values of augmentation in the impingement region, but these values drop after the impingement region. Both MC1 and MC2 see slight increases in heat transfer near the microcircuit exits.

It is possible to directly compare the heat transfer measurements from MC2 and MC3 due to the fact that the features in both cases are made of copper. The feature coverage areas of MC2 and MC3 are 29% and 32% of the total channel areas, respectively. The features of the first three rows of these two designs are identical meaning that the difference in flow area is a function of the size of the blockage feature and the guide features (see Figure 5-11 for feature labels). The lack of cooling around the large blockage feature in MC3 shows that this feature with a large area, a relatively small wetted perimeter is serving as thermal mass. Heat is being added to the copper and has limited means of convecting to the mainstream flow. Without an effective means of convecting the heat, the copper temperature increases disproportionately to the other copper features. This large hot feature is decreasing the overall heat transferred to the flow near the exit of the microcircuit because this feature is absorbing a large portion of the heat and raising the surface temperature in this area. The blockage feature in MC2 is slightly smaller in area and also has a larger perimeter to area ratio aiding in the release of heat to the coolant flow by fin effects. These conditions mitigate the thermal mass effects in MC2.

The variations in cooling at the exits of the three microcircuit designs can be explained by the intensity and direction of the jets feeding the exit. The metering areas, the geometries of which are compared in Figure 5-12, form the exit jets. The final feature in MC1 diffuses the flow on one side while forming a jet on the opposite side. The final feature in MC2 causes the formation of two jets, and the final feature in MC3 diffuses the flow on both sides of the feature. In MC1 and MC2 the laterally directed flow produces an impingement point at the intersection of the two flow paths. Spanwise averaged results show that the intersecting flow paths increase the heat transfer due to the increase in turbulence seen at the intersection.

Reynolds number effects. The Nusselt number augmentation contours are presented for comparison at various Reynolds numbers in Figures 5-13, 5-14, and 5-15. Different scales are used for each of the three microcircuits to highlight the details in the heat transfer contours of each microcircuit.

A comparison of the spanwise averaged Nusselt number augmentation for MC1 at different Reynolds numbers is presented in Figure 5-16. The pin fin HM values, calculated using the method of Pratt and Whitney's pin fin program [Cunha, 2004], are shown in comparison to the data. The experimental HM values are calculated from the Nusselt number augmentation by multiplying by hydraulic diameter and dividing by pin diameter. A gray block is placed on the data outside the pin fin region of the microcircuit for easy comparison with the pin fin results, so the area shown in white only includes data from the first three rows in the microcircuit design. The data for MC2 and MC3 are presented similarly in Figures 5-17 and 5-18.

The results for all three microcircuit designs show a decrease in heat transfer augmentation with an increase in Reynolds number. It is important to keep in mind that augmentation is not a measure of the actual heat transfer value, but how much the features increased the heat transfer. In other words, if a blade designer was trying to achieve maximum cooling, the highest Reynolds numbers would promote the highest values of heat transfer. A summary of the area averaged Nusselt numbers, baseline Nusselt numbers, and augmentation values for each microcircuit are shown in Table 5-1, and these show that the Nusselt number magnitudes are higher at high values of Reynolds number. The calculated values for HM are drastically different in MC1 than in MC2 and MC3 due to the difference in thermal conductivity of the material. Because the pin fins are the same diameter in MC2 and MC3, the only difference in the calculated values for these two cases are due to slight changes in Reynolds numbers.

The comparison to the HM values from pin fin is not perfect because several differences exist between the calculated and actual conditions. A curved inlet channel causes entrance effects, there is no development region, impingement significantly changes the flow development, and the first row of microcircuit features are not circular pins. Metzger et al. [1984] tested oblong pin fins at various angle of approach of flow. The oblong pins were compared to pin fins with diameter D, and the oblong pins tested had a length of 2D along the major axis and a width of D along the minor axis. These results show that an oval oriented with the major axis perpendicular to the flow causes an increase in heat transfer and an increase in friction factor as compared to the round pin fins. While the first row of oval pin fins in the microcircuit is not perfectly symmetric,

one would expect these features to elicit a similar response in heat transfer and friction factor. Based on these results one would expect that the combination of impingement and the oval feature would cause the HM in this region to be larger than that predicted for a pin fin array. The heat transfer measurements are higher that those predicted by pin fin, except in MC2. In MC2, the effects of the large flow blockage on the flow have propagated upstream. This has caused a decrease in heat transfer throughout the microcircuit.

In Figure 5-18 the heat transfer augmentation measured at Reynolds numbers of 5360 and 7440 are very similar despite a Reynolds number increase of 2080. Between the Reynolds numbers 7440 and 10150 the flow sees a comparable Reynolds number increase of 2710, but the results are quite different. The heat transfer increases significantly, from 7440 and 10150. The transition to turbulence cannot be exactly be pinpointed, but these results indicate a similarity between the two lowest Reynolds number cases meaning that the flow is not fully turbulent. The jump in the heat transfer between the 7440 and 10150 suggests a fully turbulent flow.

Figure 5-19 presents the area-averaged values of HM as measured and calculated using the method from the pin fin program [Cunha, 2004]. The measured results are consistently higher than those predicted by pin fin. Similarly, Figure 5-20 shows the area averaged values of Nusselt number augmentation for each microcircuit. These augmentation values follow the same trend as the HM values and decrease with increasing Reynolds number. Based on these area averages, MC3 is the most effective at cooling the microcircuit, especially in the cases with low Reynolds numbers.

The averaging method used in calculating the spanwise and area averages included the data in the feature areas. The area directly above microcircuit features was cooled by both conduction and convection in MC2 and MC3. Internal convective cooling was the focus of the internal study and the convective cooling effects were artificially increased in these locations by the conduction effects. Removing the data in the feature areas eliminated the effects of the conduction. The contours that were averaged in the cases with and without features, as well as the resulting averaged values are shown in Figure 5-21. The results with and without feature areas are not significantly different.

For simplicity, the data in all locations, including feature areas, was averaged to calculate both the spanwise and the area averages.

The next step is to compare the microcircuit results to the results from literature for similar pin configurations. While data equivalent to that measured across the oblong shapes in the microcircuit was not available, results for round pin fin arrays are readily available. While the pin fin geometry is significantly different than the microcircuit configuration, this data can be used as a baseline for comparison.

The Nusselt number augmentation values for several design configurations are presented as a function of Reynolds number in Figure 5-22. The Bunker [2003] data presented was measured in a circular tube with concave dimples where f is a ratio of the area covered in dimples to the total area. d/D is a ratio of the concavity surface diameter to the smooth tube hydraulic diameter. Also presented on this graph are the results for a staggered array of cylindrical pin fins [Chyu, 1990] with H/D = 1 and S/D = X/D = 2.5, where H = pin fin height, D = pin fin diameter, S = pin fin spacing in spanwise direction, and X = pin fin spacing in streamwise direction. This comparison shows much higher values of Nusselt number augmentation in the current study. This result was to be expected due to the large amount of blockage in the microcircuit designs. While the large blockages tend to augment heat transfer, a large pressure penalty can be expected from these blockages.

A row-by-row comparison of the current data to the Chyu [1990] pin fin data is made in Figures 5-23, 5-24, and 5-25 at three Reynolds numbers. The augmentation values for the microcircuits are higher than those measured in a pin fin array in a row by row comparison, especially in the impingement region.

A comparison to Han et al. [1992] is made in Figure 5-26 in terms of heat transfer augmentation versus X/D_h. The Han data is in a channel with several rib configurations at a Reynolds number of 14,000. The Han configurations are (1) continuous ribs perpendicular to the flow, (2) parallel broken ribs perpendicular to the flow, (3) parallel broken ribs 45° from the flow direction, and (4) parallel broken ribs 60° from the flow direction. The results show higher values for MC1 and MC3 in the impingement region, but downstream, the broken ribs result in augmentation values higher than the microcircuit designs.

5.2 Internal Friction Factors

The applicability of these microcircuit designs is dependent upon having the ability to adequately compress air enough to drive the air through the intricate channels. The pressure of the air leaving the compressor must be higher than the pressure drop encountered across the microcircuit for the microcircuit design to be considered a viable cooling option.

Friction factor measurements were taken to characterize the pressure drop across the microcircuits. While the friction factor values were not adequately benchmarked due to the unique conditions inside a microcircuit, the measured data is useful for qualitative observations. The measurement locations for friction factor and FM are presented in Figure 5-27. The 1-4 region contains the first three rows, which are approximated as a pin fin array. The 4-5 region contains only the blockage and guide features as described in Figure 5-11. The 1-5 region contains all microcircuit features.

Figure 5-28 presents the friction factor augmentation data across the whole microcircuit (region 1-5). In general, smaller values of friction factor augmentation are desirable. The results do not show a strong Reynolds number dependence. The friction factor augmentation was significantly higher in MC2 than in MC1 or MC3. Note that the values of friction factor augmentation are not representative of the magnitude of friction factor, and that the friction values increase with increasing Reynolds number. The actual values of friction factor and friction factor baseline are presented in Table 5-2.

The method used for calculation of the Friction Multiplier (FM) of the pin fin arrays mimicked the method found in Cunha's [2004] pin fin program (see Chapter 4). The FM calculated is representative of friction factor augmentation in a channel of pin fins with the open flow velocity (U_{bulk}) used in the calculation of friction factor.

The FM was calculated across the first three rows of the microcircuit for direct comparison to calculations from the pin fin program because these conditions are relatively comparable as shown in Figure 5-29. The FM values were lower than expected for MC1 and MC2 and higher than expected for MC3. One large difference between the data and the calculated values is that the FM values across the microcircuit are affected by the impingement while this effect is not present in the values predicted by pin fin. In

the calculation of FM the pressure drop drives the change in the FM values for the three microcircuits, and the impingement effects seem to drive the differences in pressure drop. Note that the heat transfer impingment effects are similar in MC1 and MC3 and that the pressure values for these two designs are also similar.

Figure 5-30 presents the FM values that were measured across the final pedestal piece. These values quantify the pressure drop caused by the blockage and guide features. The metering areas for all three microcircuits fall between locations 4 and 5. Once again MC2 has drastically different values than those measured in MC1 and MC3. This is due to the very small metering area found in MC2.

Figure 5-31 presents the data for the whole microcircuit array. The effects of the final pedestal piece cause the FM values for MC2 to be higher than the other designs. The values measured for MC1 and MC3 are comparable across the range of Reynolds numbers tested. Figure 5-32 shows all values of FM, and it is obvious that the FM values for the MC2 blockage feature are drastically larger than the values measured at any other locations.

The Nusselt number values measured for the microcircuit designs were large in comparison to those measured in similar pin fin arrays, but the friction factor values were also higher than those measured in a pin fin array. Efficiency index provides a means of taking friction factor into consideration when selecting the best cooling scheme by normalizing the increase in heat transfer by the increase in friction factor penalty. The efficiency index values for the three microcircuits are shown in Figure 5-33. The values for efficiency index are taken across the whole microcircuit (region 1-5). The visible trend is a slight decrease in efficiency with an increase in Reynolds number for MC1 and MC3. MC1 and MC3 have comparable values of heat transfer for the corresponding friction factor penalty.

Figure 5-34 shows area averaged Nusselt number augmentation as a function of friction factor augmentation. The results show the highest augmentation at the lowest Reynolds numbers. The Nusselt augmentation values are comparable for the three designs. The results show, once again, that MC1 and MC3 use coolant air most efficiently. Figure 5-35 shows these results as compared to data for Han and Zhang [1992] and Bunker et al. [2003]. Han and Zhang report comparable heat transfer

augmentation with significantly lower friction factor augmentation for channels with broken ribs at 0°, 45°, and 60° to the flow. Bunker's pin fin array results show smaller values of heat transfer augmentation than those in the microcircuit designs. The friction factor penalties incurred by Bunker's pin fin arrays are also significantly smaller than those measured in the microcircuit designs.

Figure 5-36 compares Chyu [1990] results for various pin fin arrays to the efficiency index values for the microcircuit designs. The Chyu data has been multiplied by a conversion factor because it was originally calculated based on Umax and was calculated using a Fanning friction factor. The details of this calculation are presented in Appendix E. The results find MC1 and MC3 to be comparable to an inline straight cylinder array while MC2 is comparable to a staggered, filleted cylinder array.

5.3 External Test Results

External film cooling tests were completed on a slot-shaped geometry with air exiting the slot perpendicular to mainstream flow. Internal cooling features influence the external film cooling patterns, and this section documents the effects of these internal features as well as the effects of mass flux ratio on the external cooling effectiveness.

Contours of adiabatic effectiveness for all three designs are shown in Figures 5-37 through 5-39. The internal features are also shown as they feed the cooling slots. The contours for MC1 are shown in Figure 5-37. The asymmetric feature before the slot leads to an asymmetric coolant pattern of air leaving the slot. This asymmetric cooling pattern becomes less evident at high blowing ratios [Prausa, 2004].

Adiabatic effectiveness contours for MC2 are presented in Figure 5-38. Similar patterns are visible at all blowing ratios. A decrease in cooling is visible between the mass flux ratios of 0.50 and 0.71. The cooling contours for MC3, shown in Figure 5-39, are focused at the center of the slots because a symmetric feature lies just upstream of the slot.

A comparison of the contours for MC1, MC2, and MC3 at a blowing ratio of 0.50, shown in Figure 5-40, highlights the effects that the internal features have on the external cooling contours. The asymmetric feature before the slot exit in MC1 causes the

air to exit the slot asymmetrically. The final features in MC2 and MC3, visible in Figures 38 and 39, are symmetric with respect to the coolant slot, and as a result the air exits these slots fairly symmetrically. The contours for MC2 are spread more evenly along the slot than the contours for MC3. A small amount of lateral spreading is also visible in the contours for MC2.

Spanwise averaged values of η provide a more quantitative means of comparing the contours. One convention in the data is to non-dimensionalize length using a geometric parameter s. The parameter s is calculated using the following equation:

$$s = \frac{l \cdot w}{P} \tag{5.1}$$

where l is the length of the slot, w is the width of the slot, and P is the sum of the length of the slot and the distance between two adjacent slots. The measurements for the calculation of s are shown in Figure 5-41, and the resulting s = 0.548 cm. Dividing by the value s allows for a consistent comparison of different geometries by dividing by a coverage factor, thereby converting all results to those equivalent to a continuous cooling slot. After normalization, the measurable streamwise distance in X/s was around 60. A spanwise average was taken at each data collection location from X/s = 0 to X/s = 60 as shown in Figure 5-42.

Comparison of three microcircuit designs. A comparison of the external adiabatic effectiveness values of the three microcircuit designs was made at three blowing ratios. Figure 5-43 shows the spanwise averaged values at a mass flux ratio of 0.50. The trends for MC2 and MC3 were similar with the values for MC1 dropping off more rapidly, but remaining cool longer than the other two designs. The behavior of MC1 is inexplicable. This trend is common to the MC1 data at all mass flux ratios before and after reanalysis of the data using a revised data analysis method (detailed in Chapter 4). Figure 5-44 shows two sets of the MC1 data before and after reanalysis of the data. The data all lies within a small band, and while the change in the data analysis method

does cause a reversal of the data for the two mass flux ratios, the change in magnitudes is well within the uncertainty of the data (19% for values of η close to 0.2).

A comparison of film effectiveness for the three microcircuits at mass flux ratios of 0.75 and 0.71 is made in Figure 5-45. MC3 is most effective in the near slot region while MC2 is the most effective further downstream. The same results are observable at a mass flux ratio of 1, shown in Figure 5-46. In both cases MC1 is considerably lower in the near slot region, but it cools comparably to the other microcircuit designs further downstream.

Figure 5-47 compares the MC1 results at three different blowing ratios. Results show the most effective cooling at the lowest blowing ratios. This is counterintuitive because one would expect that increasing the amount of cool air would lower the temperature. The increase in cooling with a decrease in coolant can be explained by flow separation or liftoff. At the higher blowing ratios the air has more momentum into the mainstream as it leaves the slot, causing it to separate from the wall. At the lower blowing ratios the air remains attached to the wall, limiting the mixing with the heated mainstream. The attached air provides a more effective protective layer along the wall.

The same trend of increased cooling with decreased coolang was observable in the near slot region of MC2 as shown in Figure 5-48. In this case the lowest blowing ratio loses its effectiveness far downstream of the slot.

Figure 5-49 shows the different cooling effectiveness averages for MC3. No measurable change in cooling effectiveness was found based on blowing ratio for this microcircuit design.

A check of the magnitudes near the slots was made using the spanwise averages at the location X/s = 0 which lies at the downstream side of the downstream slot. The values in the slots and immediately after the slots were, in theory, perfectly cooled. As a result, values measured immediately after the slots should have resulted in an η of 1. The measured values of the wall upon which no coolant fell were theoretically 0. The slots were not aligned exactly, and an X/s of 0 was measured at 0.953 cm downstream of the upstream slot, so this estimate is not perfect because at this point some mixing of air from the upstream slot had already occurred. Based on these estimates, the average eta measured between the two slots should be roughly equal to the percentage of the

spanwise width occupied by the two slots. Based on this estimate, the maximum achievable value of cooling effectiveness at X/s = 0 is $\eta = 0.64$. This value is higher than the measured values seen in Figures 5-43 through 5-49 because the cooling from the upstream slot has already decreased slightly at this location. The fact that measurements are made downstream of the upstream slot drops the maximum average values to values between 0.45 and 0.55, which are lower than the predicted value of $\eta = 0.64$.

Area averaged values provide a means of easily comparing trends between microcircuits and cooling ratios. The area used in the calculations covered the entire span of the measurement data and went from an X/s of 0 to 35 as shown in Figure 5-50. This area was selected to focus on the higher values of eta, which have lower values of uncertainty. The results, shown in Figure 5-51, are plotted with respect to mass flux ratios. As observed in the spanwise averaged values, a distinct trend of decreasing cooling effectiveness with increasing mass flux ratio is observable. The same trend is observed in MC3, but to a lesser extent.

Cooling effectiveness curves are shown in Figure 5-52 on a log-log scale. The log scale plot focuses on the trends in the near slot region. In this plot, the data is grouped together by mass flux ratio. This indicates that all microcircuit designs cool similarly and that while internal features affect the cooling contour shape, the overall magnitudes of cooling effectiveness are comparable for all microcircuit designs. The feasibility of a microcircuit design is therefore more dependent on the internal cooling performance and the friction factor values for the design.

Curve fits for the film cooling effectiveness as a function of X/Ms are shown in Figures 5-53 through 5-55. The curve fits are calculated using the following equation:

$$\overline{\eta} = \frac{1}{\frac{P}{w} + C_1\left(\frac{X}{Ms}\right)^{C_2}} \tag{5.2}$$

where P is half of the pitch of the data collection area, w is the width of the slot, X/Ms retains the same definition, and C_1 and C_2 are constants based on the coefficients of power curve fits of the experimental effectiveness data for a given blowing ratio. The

values of C_1 and C_2 for all microcircuits and blowing ratios are presented in Table 5-3. The values of P and w used in the calculations were 9.91 cm and 6.35 cm, respectively.

To determine the feasibility of microcircuit designs, the measured values were compared to data from literature. The first comparison was made to data for a row of 14 film cooling holes inclined 35° from the horizontal [Drost et al., 1997]. The spanwise averaged effectiveness was measured at mass flux ratios of 0.5, 0.7, and 1.0 for these holes with a diameter of 1.8 mm. The testing was completed at a Mach number of 0.3. The Drost et al. [1997] data was presented as X/d initially, but was converted to X/s for comparison with the microcircuit data [Prausa, 2004]. The parameter s was calculated using Equation 5.1 where the numerator represents the hole area. The spanwise averaged cooling data for the cooling holes is more effective than the slot cooling at all blowing ratios as seen in Figures 5-56, 5-57, and 5-58. In the Drost data, the cooling holes are inclined, and inclination has consistently been shown to increase cooling effectiveness. Inclination decreases the momentum of the coolant into the mainstream flow, thereby decreasing the amount of mixing with the mainstream flow. Mixing increases the temperature of the coolant, and also attenuates the effectiveness of the jet as it loses its momentum along the direction of the flow.

Sinha et al. [1994] data is shown in Figure 5-59. The Sinha data was converted from X/d to X/s similarly to the Drost et al. [1997] data. The coolant injection holes in Sinha et al. [1994] data have a small L/D (length/diameter) ratio of 1.75. Small L/D holes generally result in larger injection angles leading to increased liftoff. Sinha et al. [1994] see much more variation in the cooling with a change in blowing ratio that the current data. The air leaving the coolant holes in the Sinha et al. [1994] data retains its momentum and does not mix with the flow at a blowing ratio, and cooling drops off considerably for the higher blowing ratio. This suggests that the features that the flow encounters before the slot exit seem to damp out any variations in cooling effectiveness in the VTExCCL data.

Figures 5-60 and 5-61 compare microcircuit slot cooling in MC2 and MC3 to cooling from an inclined continuous slot [Liburdy et al., 1997]. The results were similar for all microcircuits. The slot was inclined 35° from the horizontal direction and was 5 mm wide. The values measured by Liburdy et al. [1997] were higher than those

measured for the microcircuit design. The inclination increased the effectiveness of the cooling flow. The fact that the slot was continuous did not allow for as much mixing as occurred with the flow from discrete slots as seen in the microcircuits.

Centerline data is more comparable to Liburdy et al. [1997] as shown in Figure 5-62. This is because the uncooled portions between the slots lower the average values, while the centerline data extracts information only from the cooled portion of the microcircuit. The centerline is the location least affected by mixing at the edges of the slots. The Liburdy et al. [1997] data maintains its cooling effectiveness longer than the microcircuit data due to the inclination of the slot, but overall the data for the two configurations are in good agreement as shown in the comparison to MC3 data.

This chapter has presented heat transfer, adiabatic effectiveness, and friction factor results for three microcircuit designs. MC3 saw the highest overall cooling augmentation, especially at the lowest Reynolds numbers. MC1 and MC3 had comparable values of efficiency, cooling augmentation to pressure loss ratio. The efficiency index values measured for MC2 were much lower than those measured in the other two designs. The external adiabatic film-cooling results are similar for the three microcircuit designs according to spanwise averages of film cooling measurements, but the adiabatic effectiveness contours vary for the three microcircuit designs.

Table 5-1 Summary of Nusselt Number Augmentation calculations (Nusselt Number Measurements Taken Across First Three Rows)

MC1

Re	Nu	Nu_o	Nu/Nu_o	HM	Predicted HM
5380	70.6	17.34	4.07	5.02	2.12
6950	85.57	21	4.08	5.03	2.05
10500	114.4	28.57	4	4.93	1.9
15126	134.48	37.52	3.58	4.41	1.79

MC2

Re	Nu	Nu_o	Nu/Nu_o	HM	Predicted HM
5370	64.84	17.32	3.74	5.20	4.51
7640	80.12	22.53	3.56	4.95	4.25
10150	88.55	27.86	3.18	4.42	3.99
15280	110.9	37.81	2.93	4.08	3.8

MC3

Re	Nu	Nu_o	Nu/Nu_o	HM	Predicted HM
5400	83.49	17.39	4.8	6.68	4.38
7430	104.06	22.07	4.72	6.57	4.19
10150	112.73	27.86	4.05	5.64	4
14380	128.94	36.13	3.57	4.97	3.8

Table 5-2 Summary of Friction Factor Augmentation Calculations

MC1

Re	f	f_o	f/f_o
5270	3.35	0.0371	90.0
6950	2.77	0.0346	80.0
10500	3.31	0.3120	105.9
15130	2.76	0.0285	97.0

MC2

Re	f	f_o	f/f_o
5090	6.69	0.0375	178.5
6620	5.38	0.0351	153.4
10010	4.3	0.0315	136.3
14270	4.17	0.0289	143.9

MC3

Re	f	fo	f/fo
5090	2.75	0.0374	73.3
7610	3.57	0.0339	105.4
10200	3.34	0.0315	106.0
14710	3.1	0.0287	107.9

Table 5-3 Summary of Mass Flux Ratios and the Corresponding Microcircuit Reynolds Numbers

M	Corresponding Microcircuit Reynolds Number
0.5	3300
0.75	4860
1	6050
1.44	8810

Re	Corresponding External M
5000	0.89
7500	1.24
10,000	1.66
15,000	2.36

Table 5-3 Summary of Construction Curve Constants

MC1

Re	C_1	C_2
0.5	0.0217	1.3656
0.75	0.832	1.1071
1	0.0806	1.2504

MC2

Re	C_1	C_2
0.5	0.0163	1.3715
0.71	0.0868	1.09
1	0.3779	0.7287

MC3

Re	C_1	C_2
0.5	0.2983	0.6136
0.75	0.4368	0.66
1	0.6439	0.6968

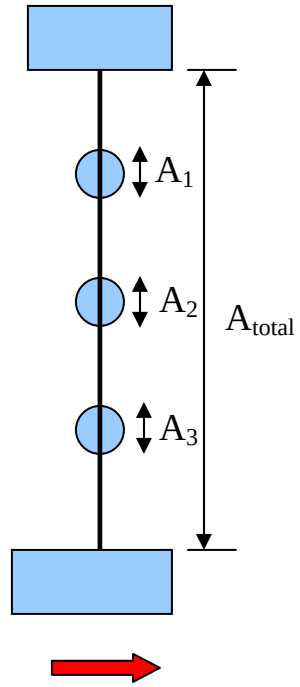

$$\frac{A_{blockage}}{A_{total}} = \frac{A_1+A_2+A_3}{A_{total}}$$

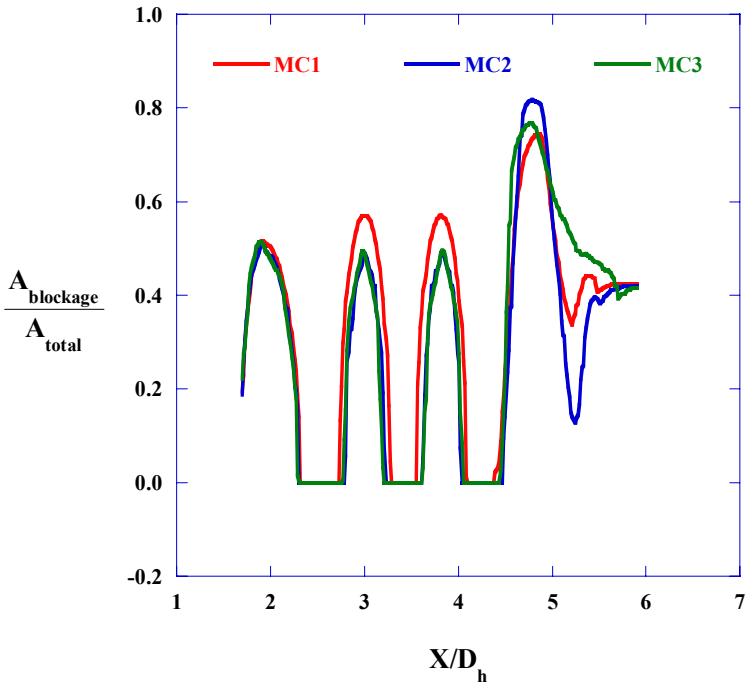

Figure 5-1. (a) Calculation of blockage parameter (b) Blockage along the length of the microcircuit.

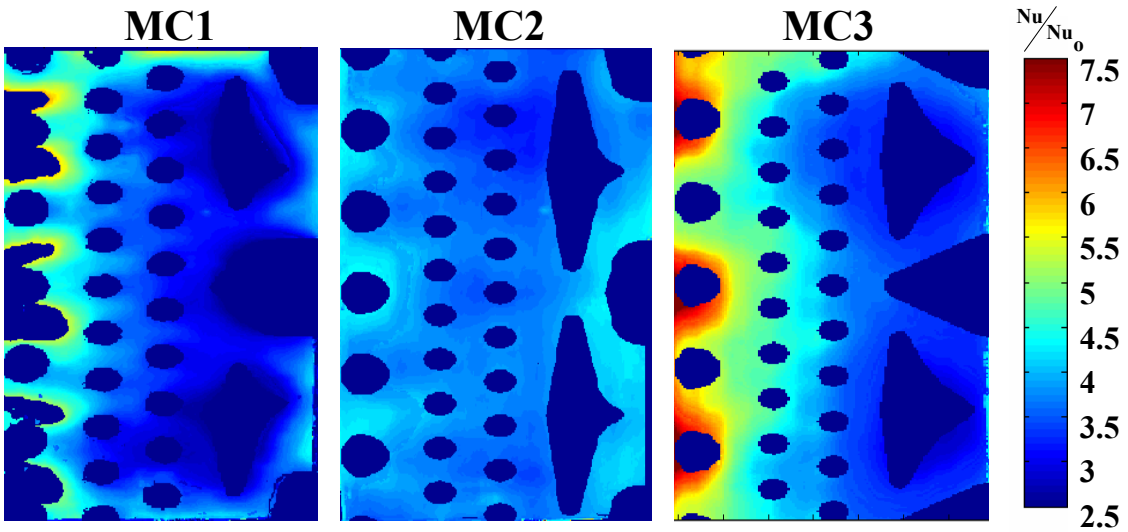

Figure 5-2. Comparison of contours for three microcircuit designs at Re ~ 5300 (Percentage of open flow area to total area: 66%, 71%, and 68%).

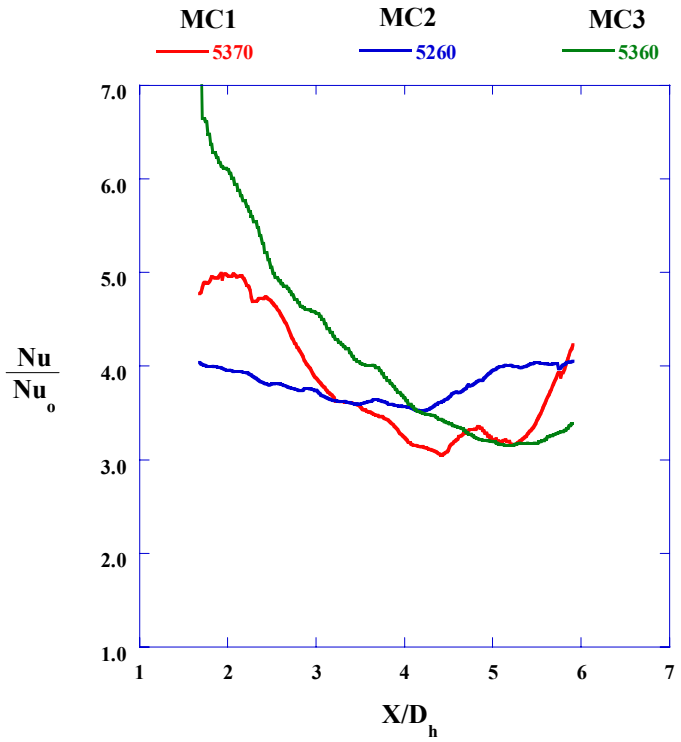

Figure 5-3. Spanwise averaged values for three microcircuit designs at Re ~ 5300.

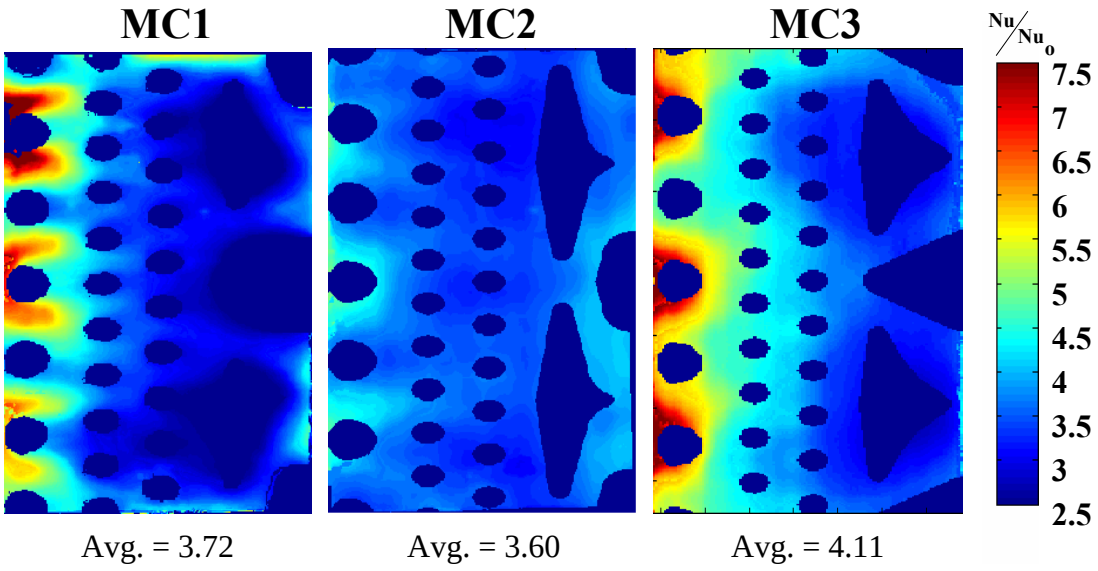

Figure 5-4. Comparison of contours for three microcircuit designs at Re ~ 7500 (Percentage of open flow area to total area: 66%, 71%, and 68%).

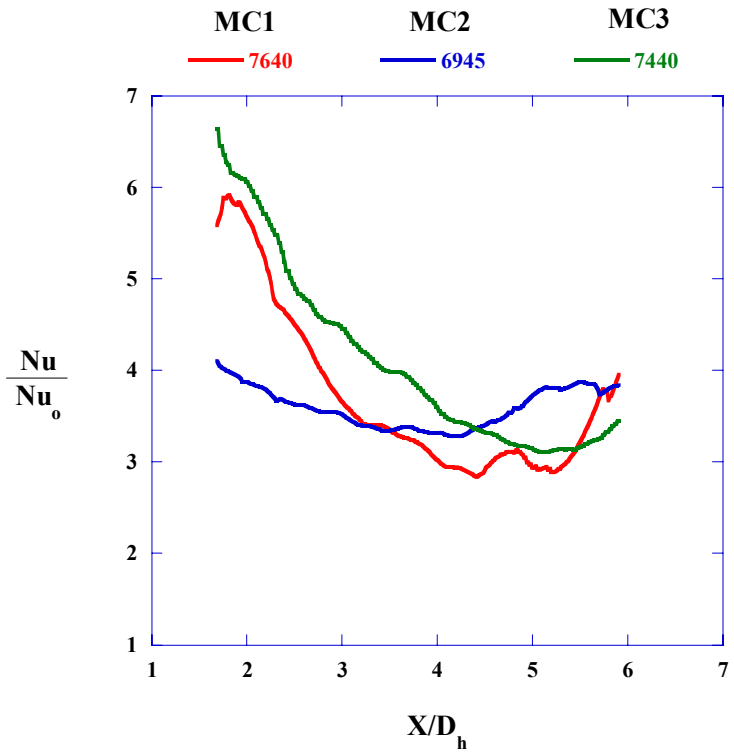

Figure 5-5. Spanwise averaged values for three microcircuit designs at Re ~ 7500.

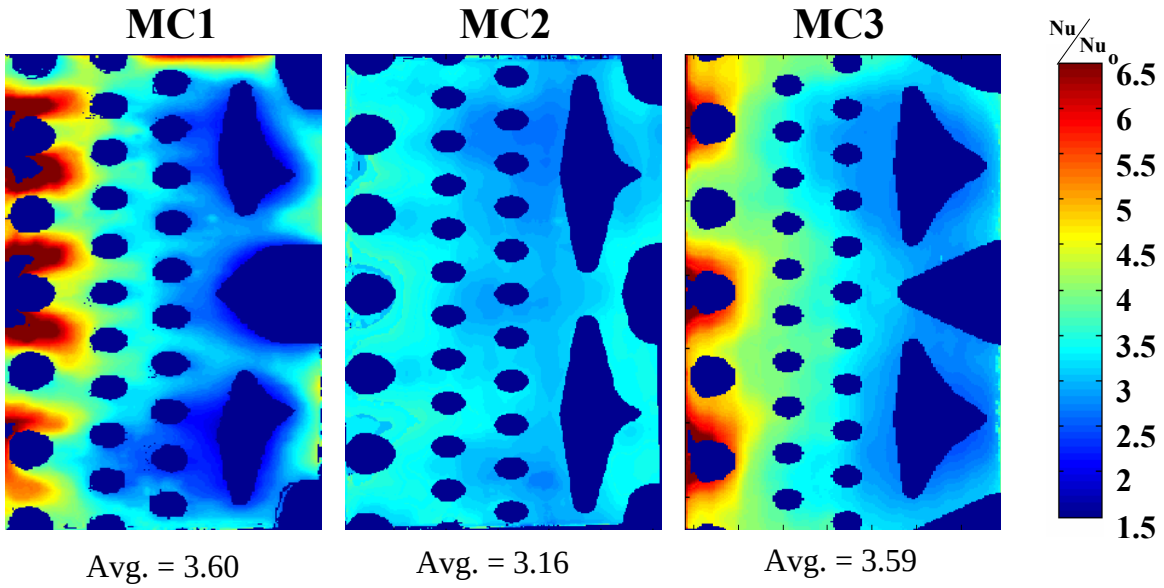

Figure 5-6. Comparison of contours for three microcircuit designs at Re ~ 10,200 (Percentage of open flow area to total area: 66%, 71%, and 68%). Note: change in scale.

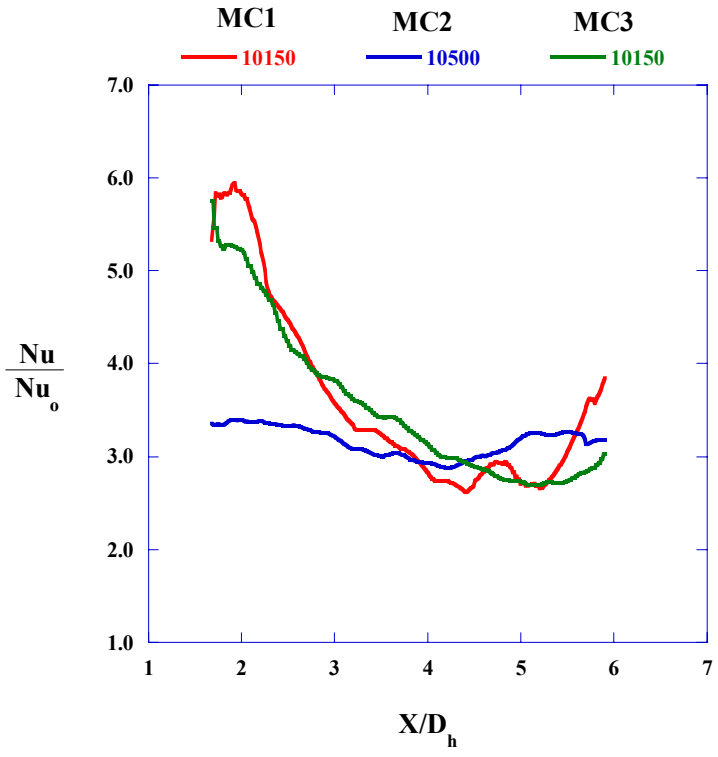

Figure 5-7. Spanwise averaged values for three microcircuit designs at Re ~ 10,200.

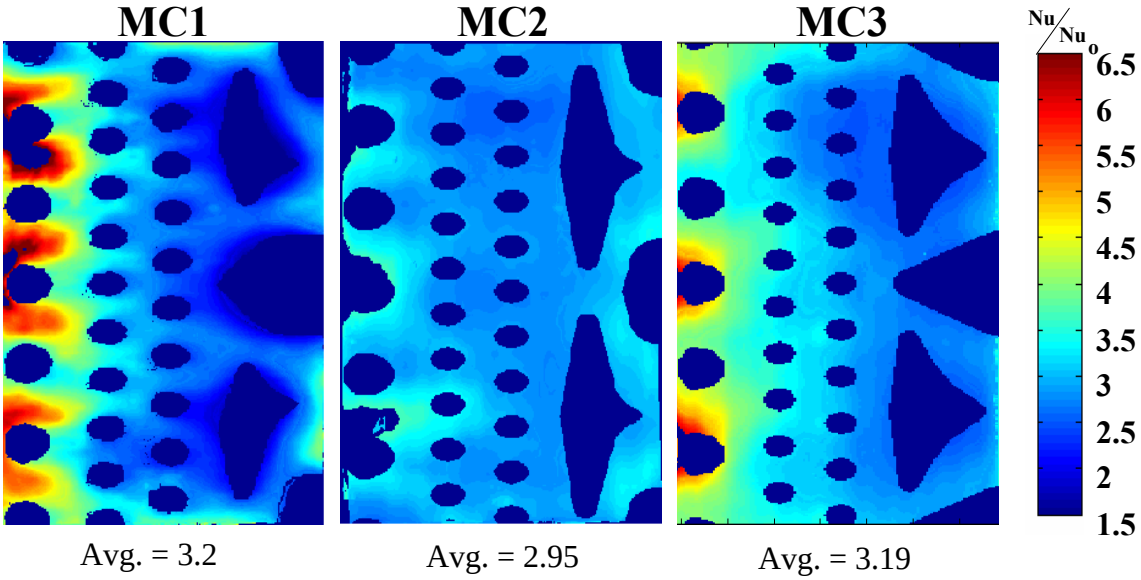

Figure 5-8. Comparison of contours for three microcircuit designs at Re ~ 15,000 (Percentage of open flow area to total area: 66%, 71%, and 68%).

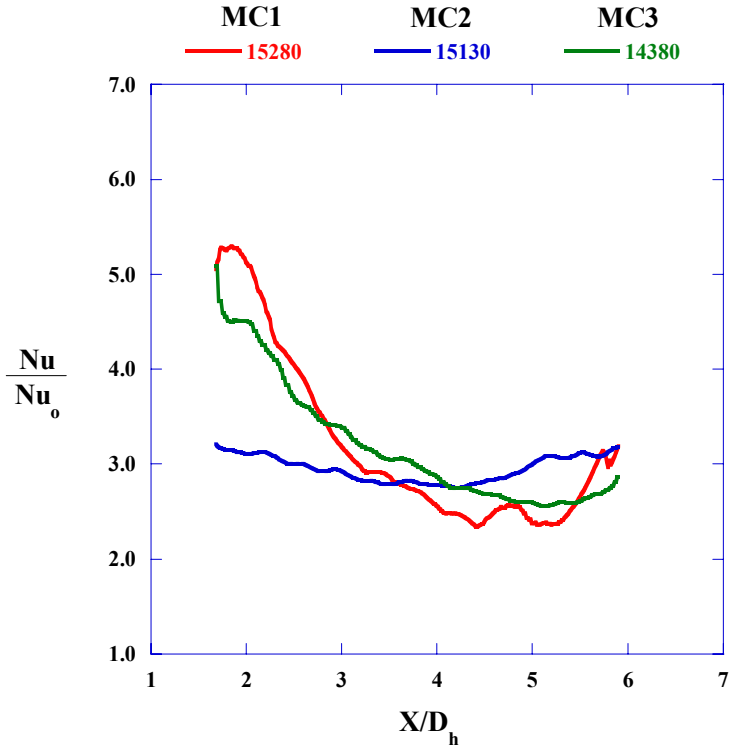

Figure 5-9. Spanwise averaged values for three microcircuit designs at Re ~ 15,000.

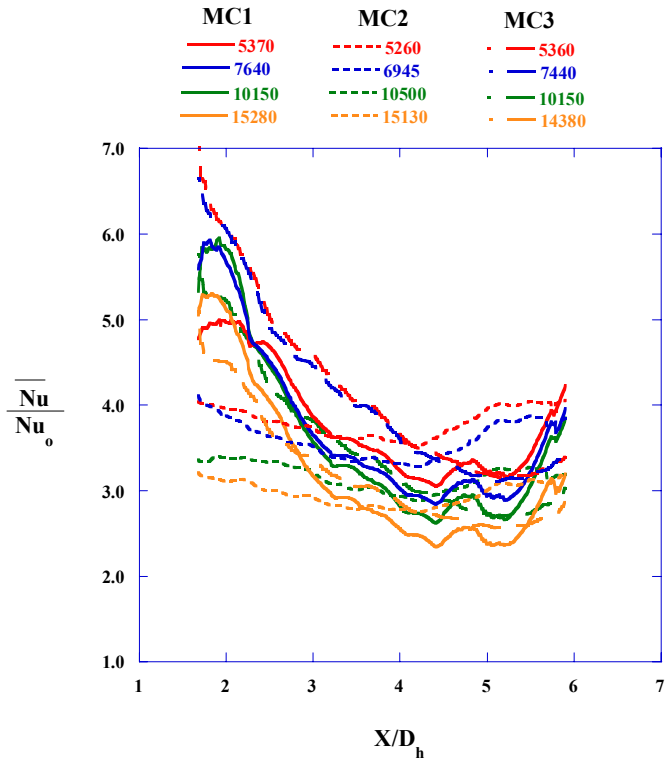

Figure 5-10. Averaged values of Nusselt number augmentation for three microcircuit designs at all Reynolds numbers.

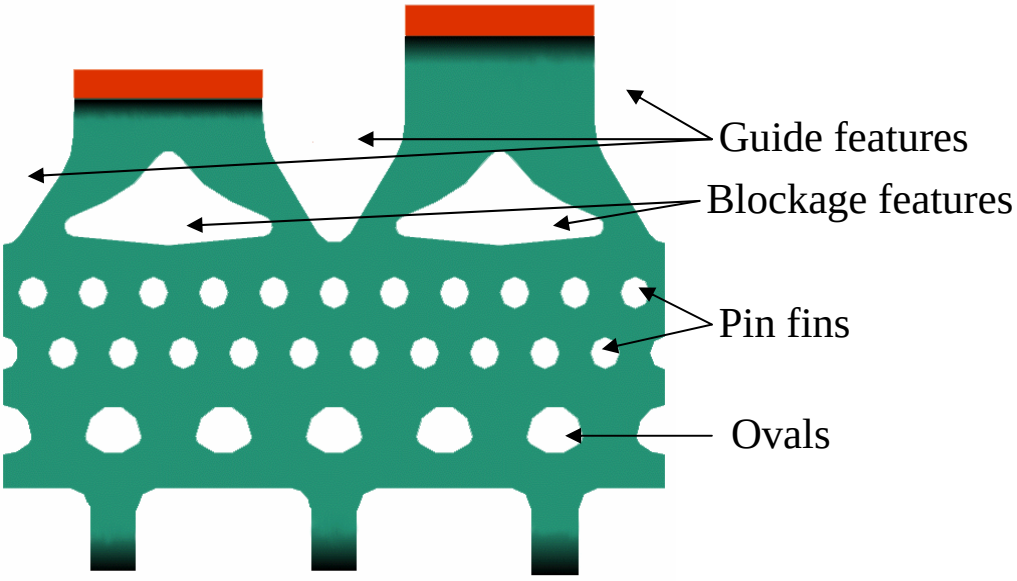

Figure 5-11. Feature names presented for reference (The green area is the flowpath, and the white areas are feature areas).

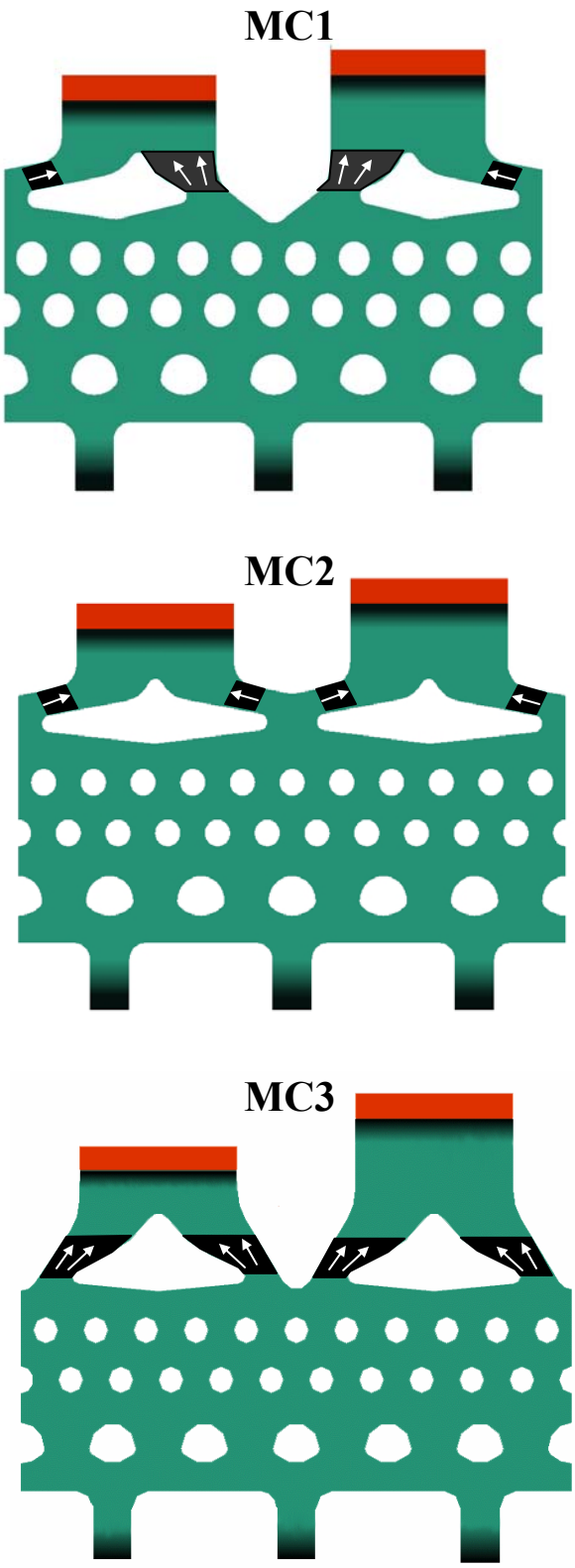

Figure 5-12. Directionality of exit feeds.

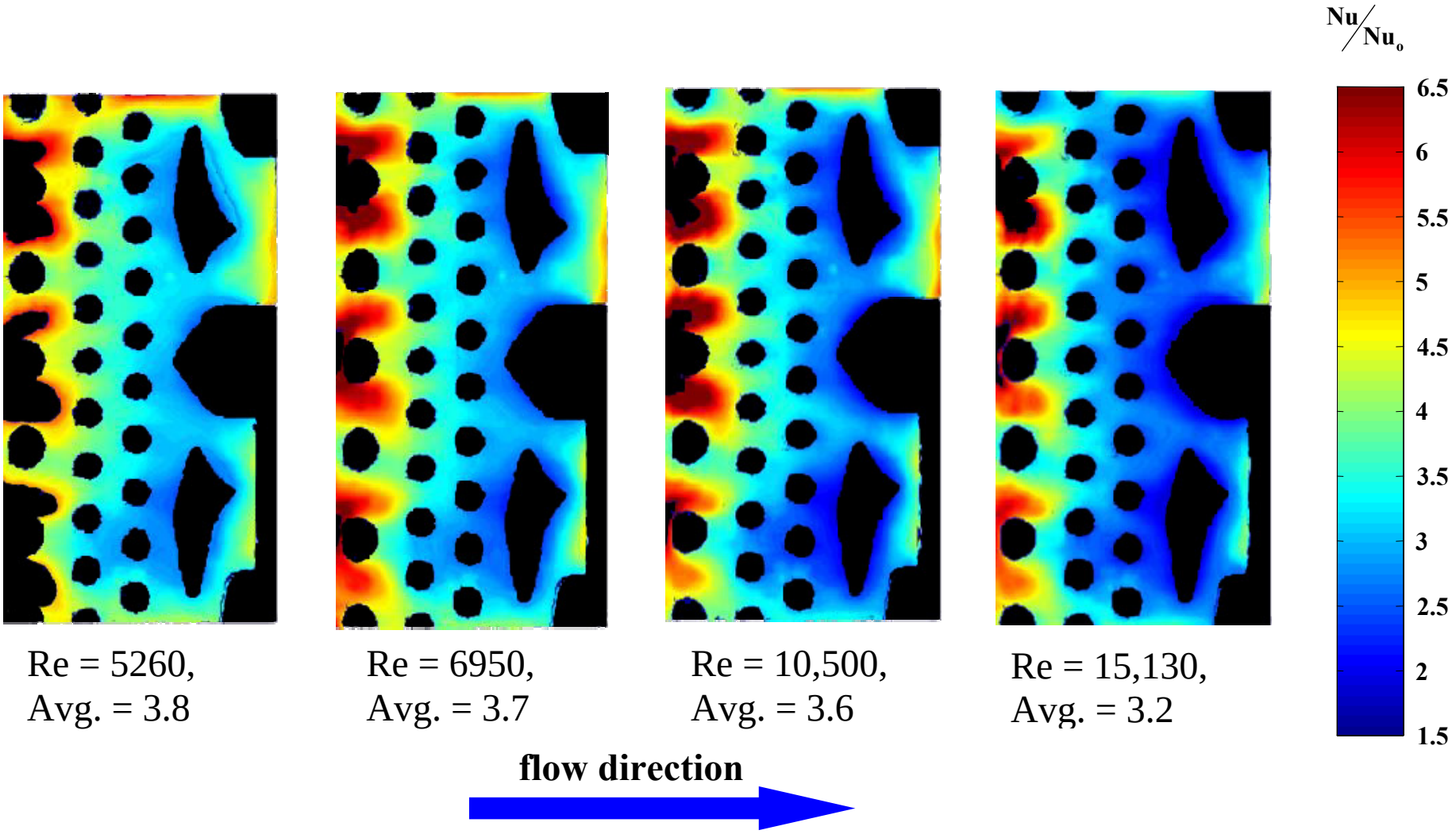

Figure 5-13. Nusselt number augmentation contours for MC1 (note: foam features).

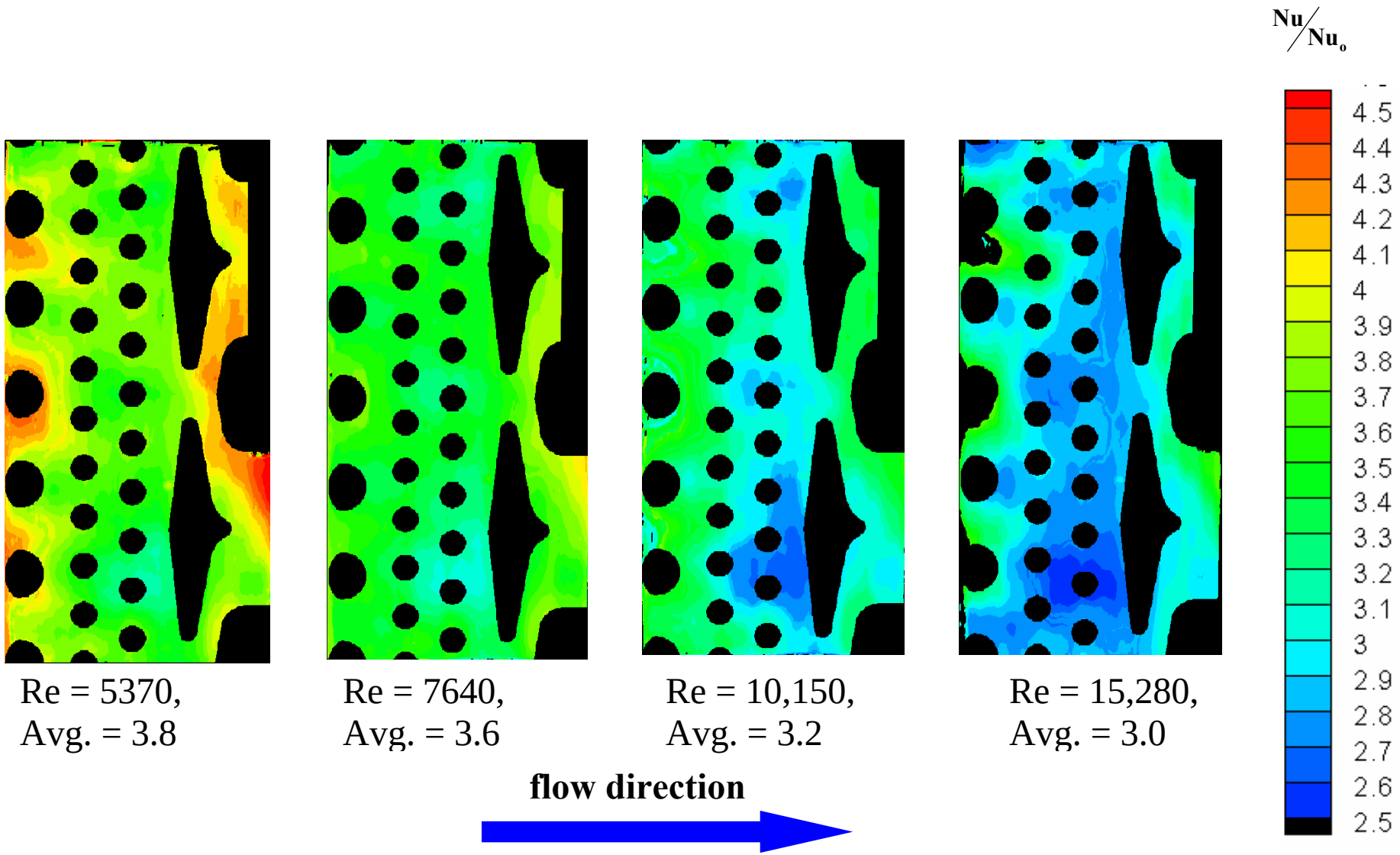

Figure 5-14. Nusselt number augmentation contours for MC2 (note: copper features and change in scale).

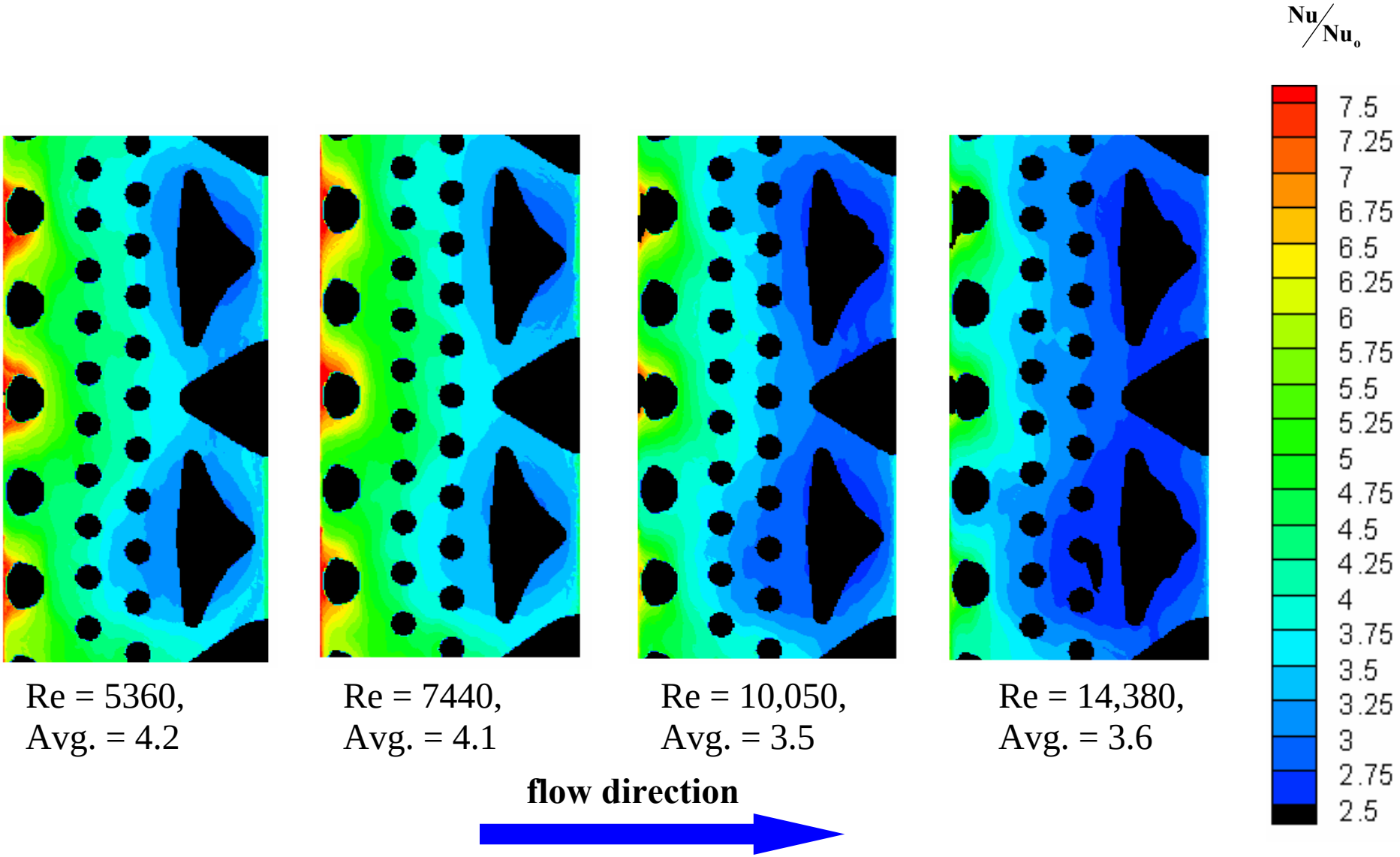

Figure 5-15. Nusselt number augmentation contours for MC3 (note: copper features and change in scale).

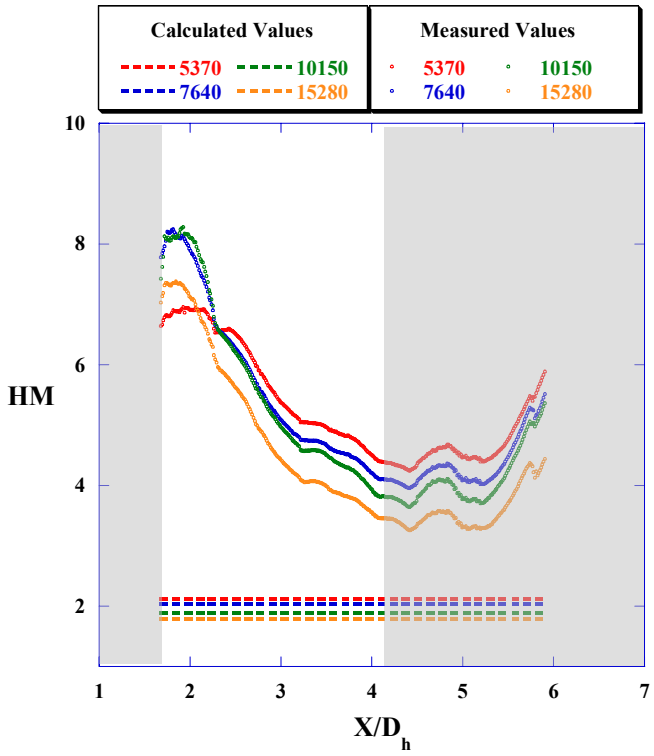

Figure 5-16. Measured HM values of MC1 compared to HM values calculated for a pin fin array at the same Reynolds numbers. The blocked out regions lie outside the pin fins.

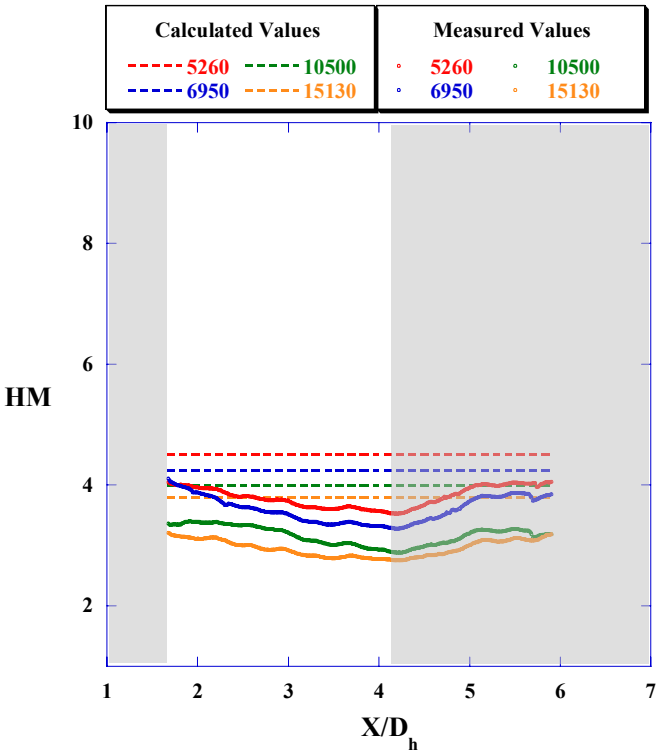

Figure 5-17. Measured HM values of MC2 compared to HM values calculated for a pin fin array at the same Reynolds numbers. The blocked out regions lie outside the pin fins.

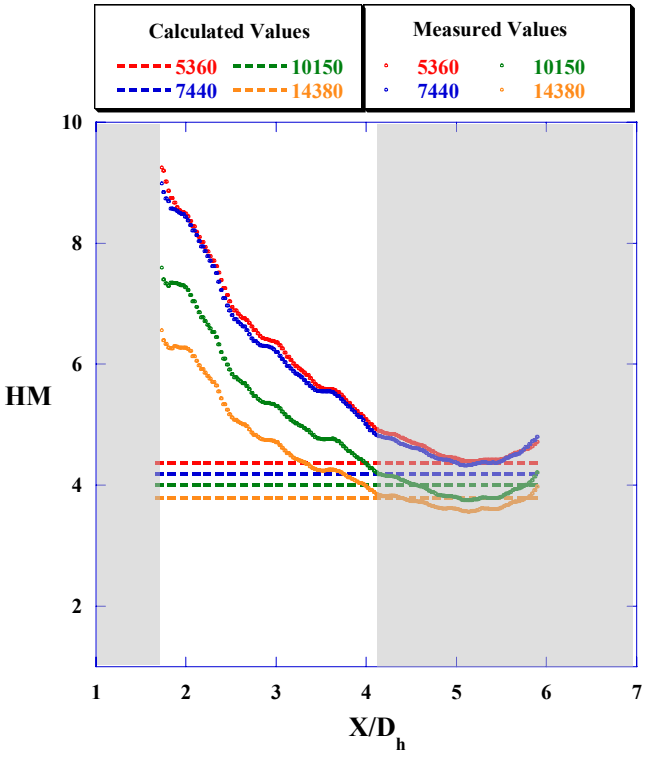

Figure 5-18. Measured HM values of MC3 compared to HM values calculated for a pin fin array at the same Reynolds numbers. The blocked out regions lie outside the pin fins.

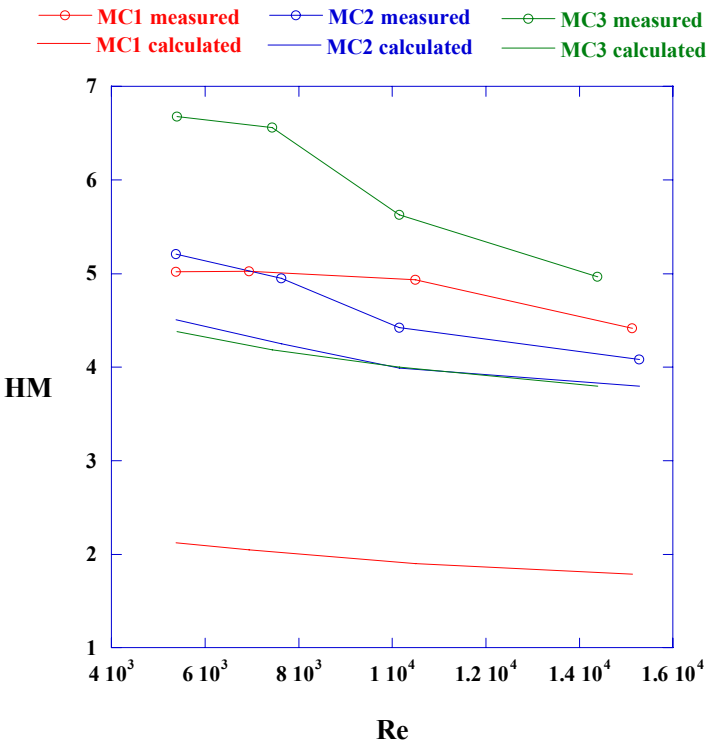

Figure 5-19. Area averaged values of HM compared to calculated values for a pin fin array at the same Reynolds number. Lower calculated values for MC1 are due to the low thermal conductivity of the pedestal features.

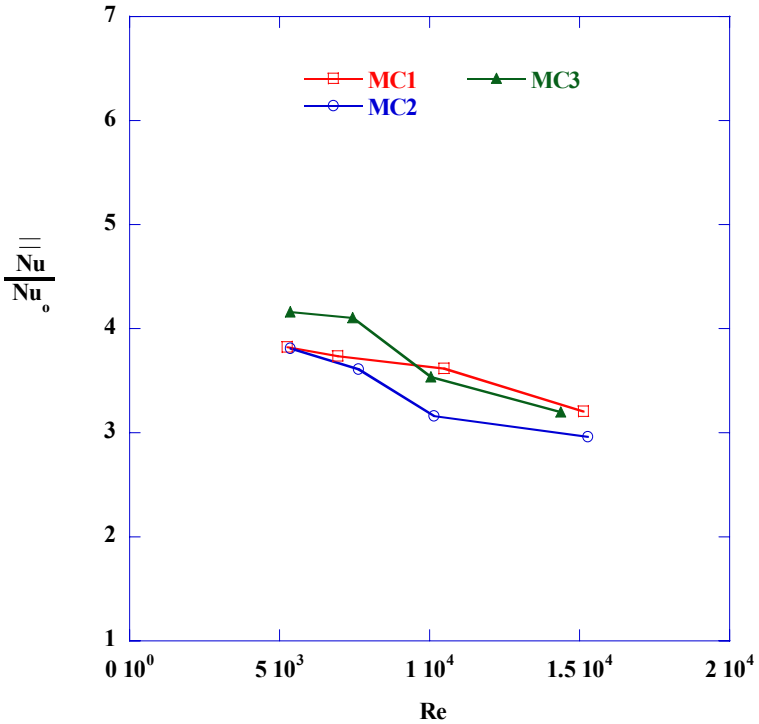

Figure 5-20. Area averaged Nusselt number augmentation.

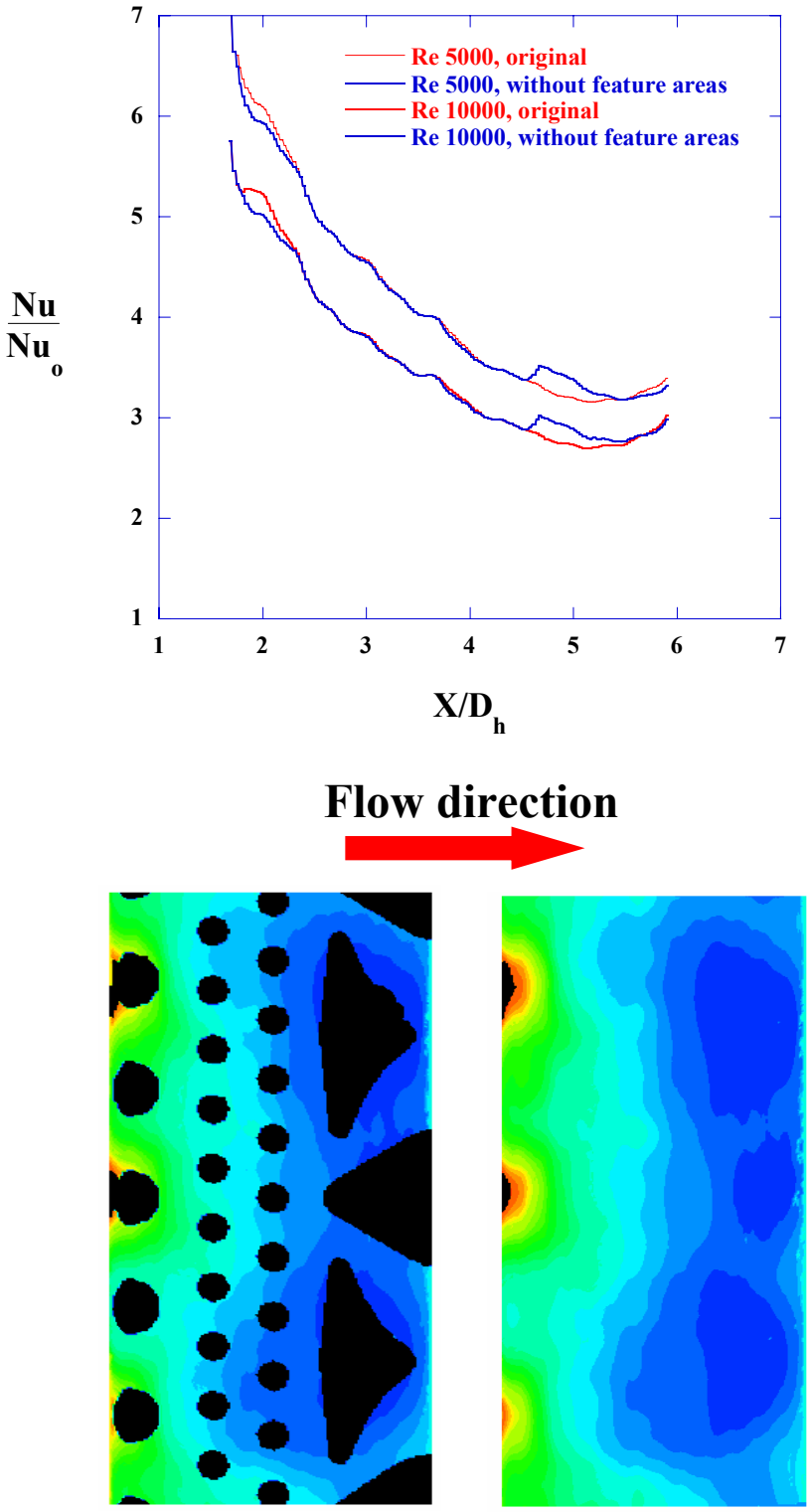

Figure 5-21. (a) Image averages taken with and without feature location data included (b) MC3 shown with and without feature data area.

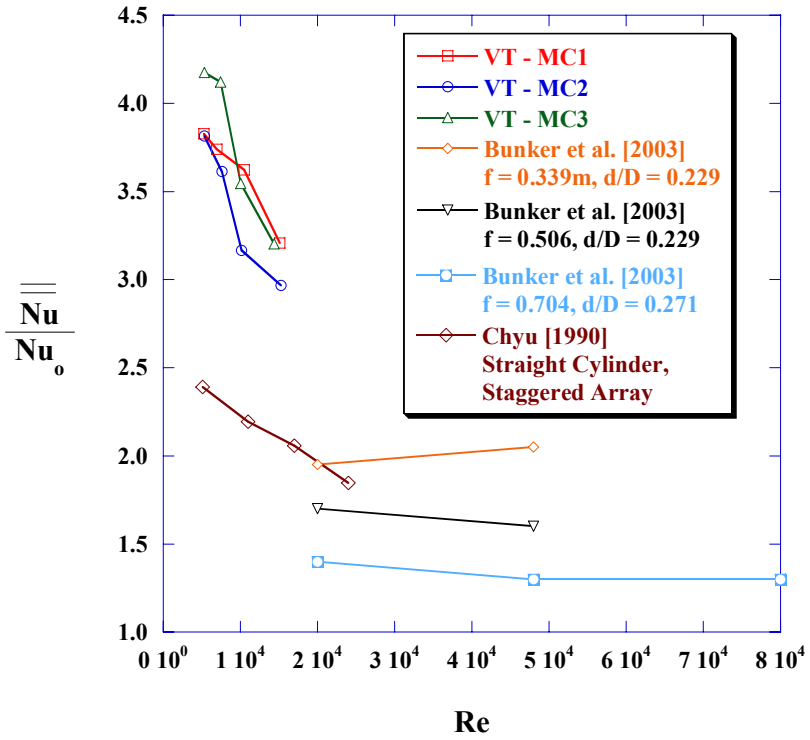

Figure 5-22. Virginia Tech heat transfer values compared to various pin fin arrays.

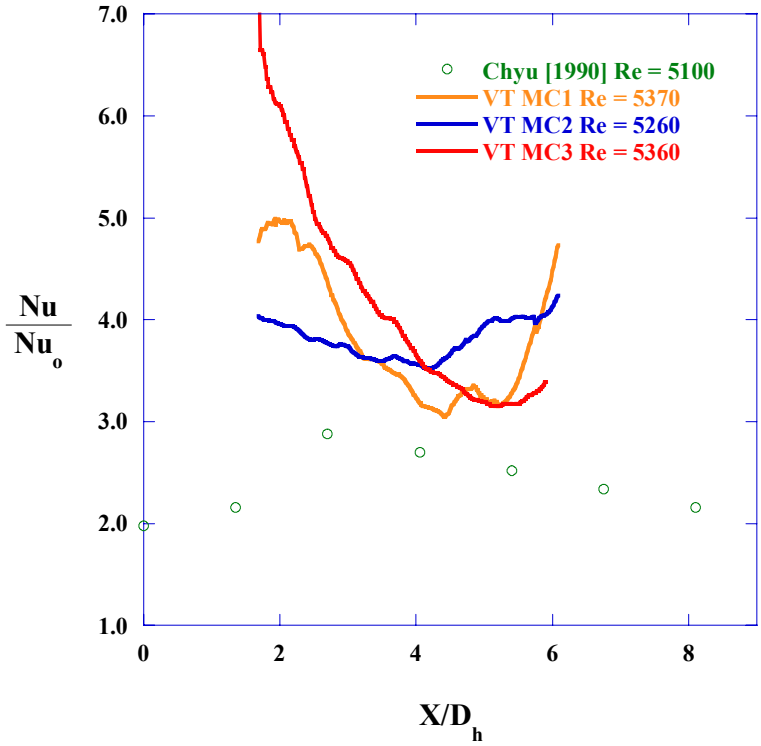

Figure 5-23. Row by row comparison to Chyu [1990], Re = 5000.

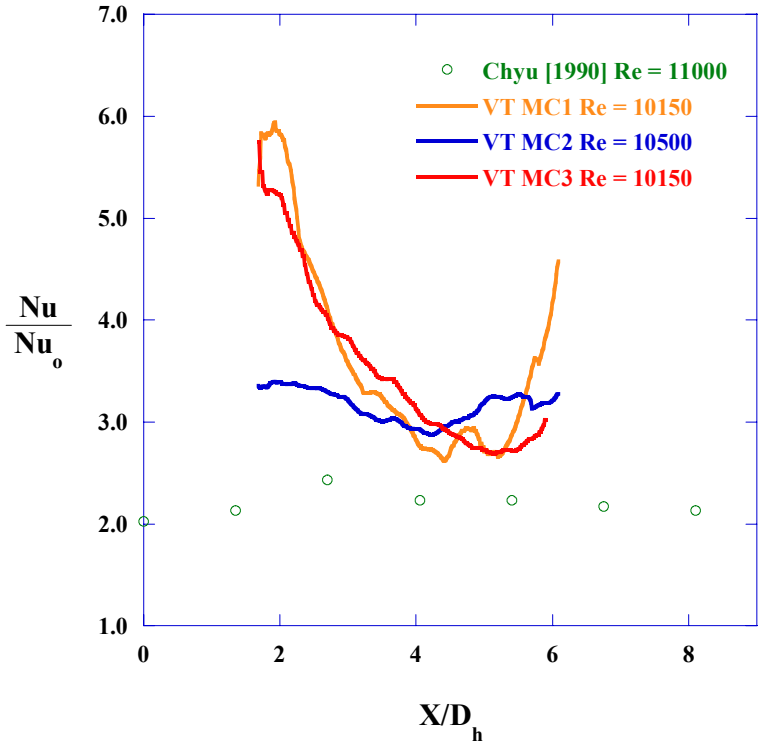

Figure 5-24. Row by row comparison to Chyu [1990], Re = 10,000.

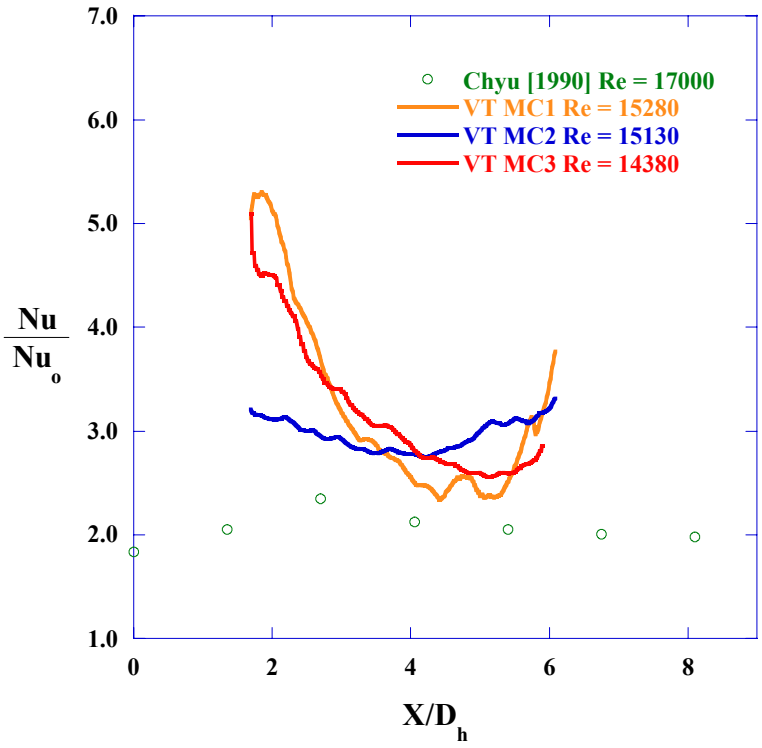

Figure 5-25. Row by row comparison to Chyu [1990], Re = 15,000.

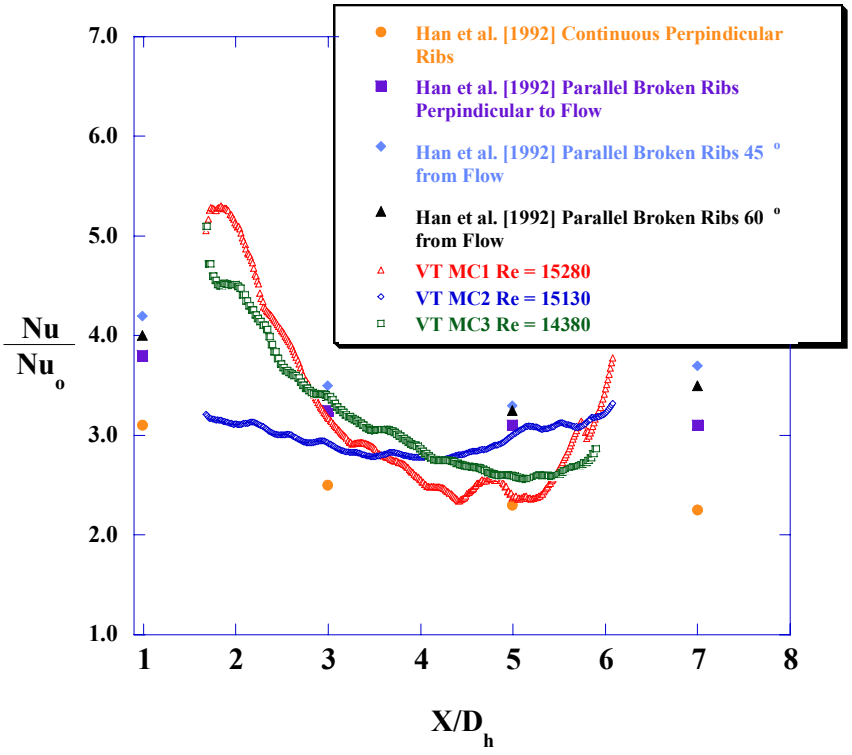

Figure 5-26. Spanwise averaged heat transfer augmentation compared to Han et al., [1992] ribbed channel data.

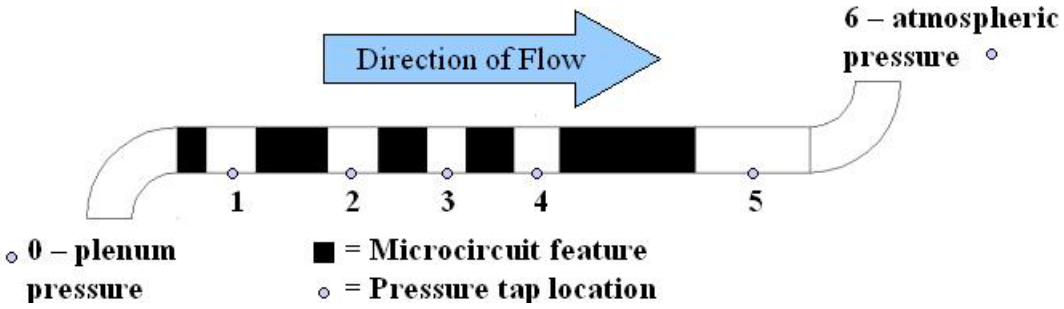

Figure 5-27. Pressure tap locations in streamwise direction.

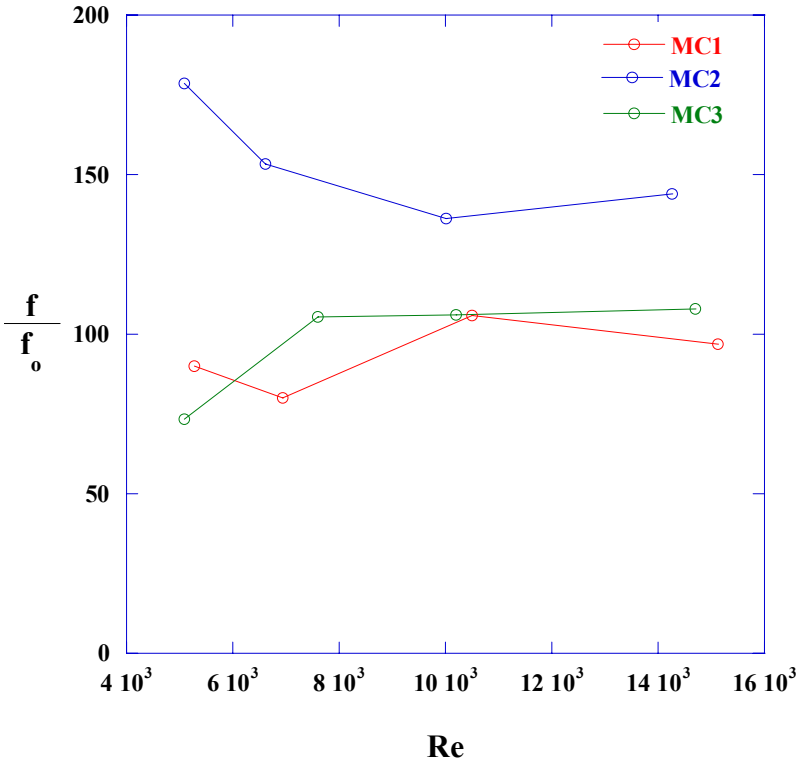

Figure 5-28. Friction factor values are considerably higher for MC2 than for the other two designs.

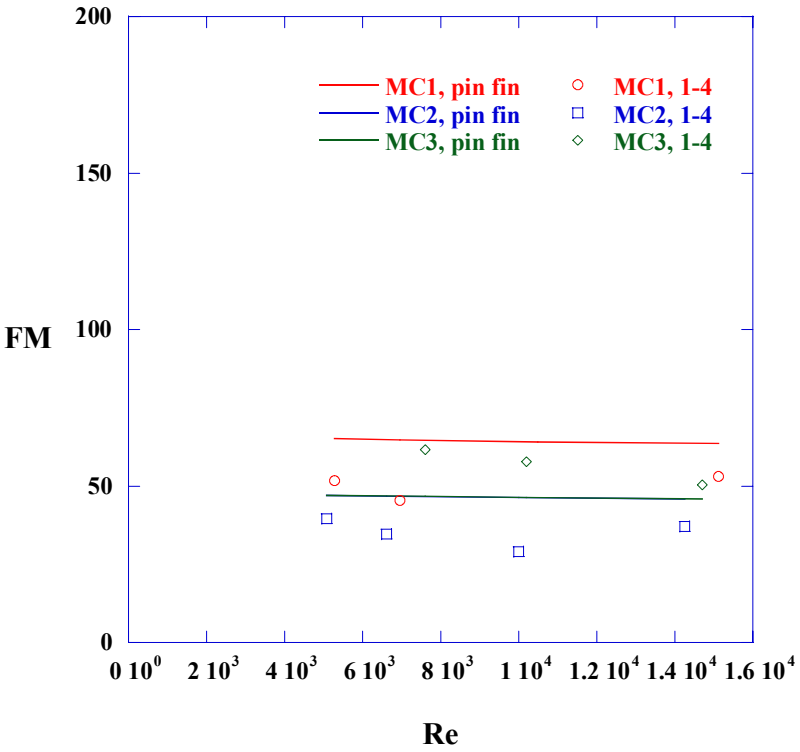

Figure 5-29. Pin fin predictions and values measured for first three rows microcircuit (see Figure 5-27 for locations 1 and 4).

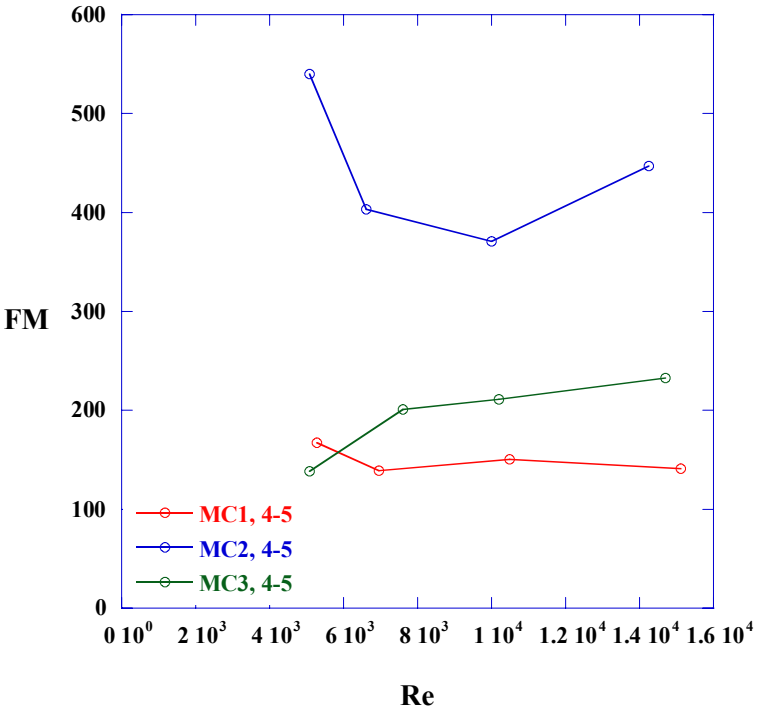

Figure 5-30. Friction multipliers measured only across last pedestal piece (see Figure 5-27 for locations 4 and 5).

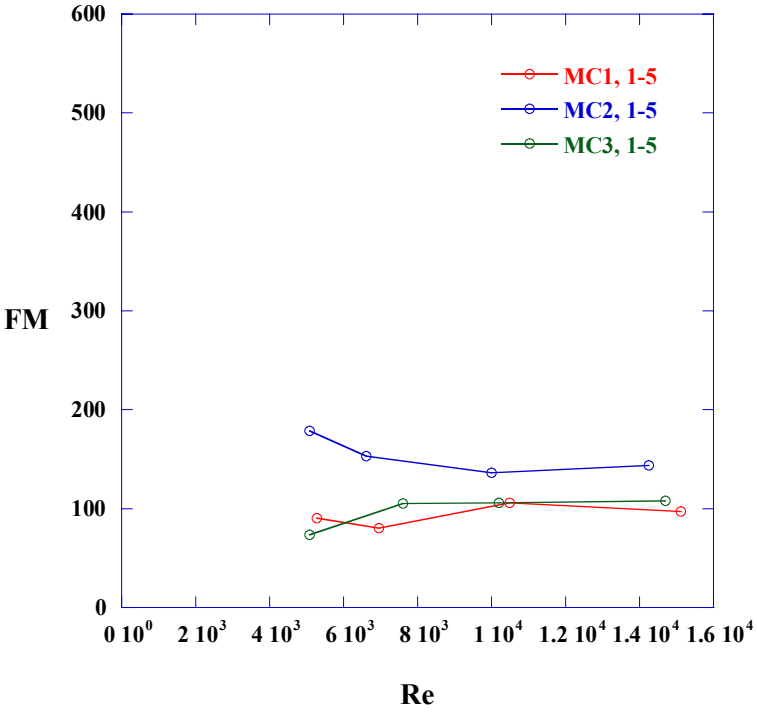

Figure 5-31. Friction multipliers measured across whole microcircuit (see Figure 5-27 for locations 1 and 5).

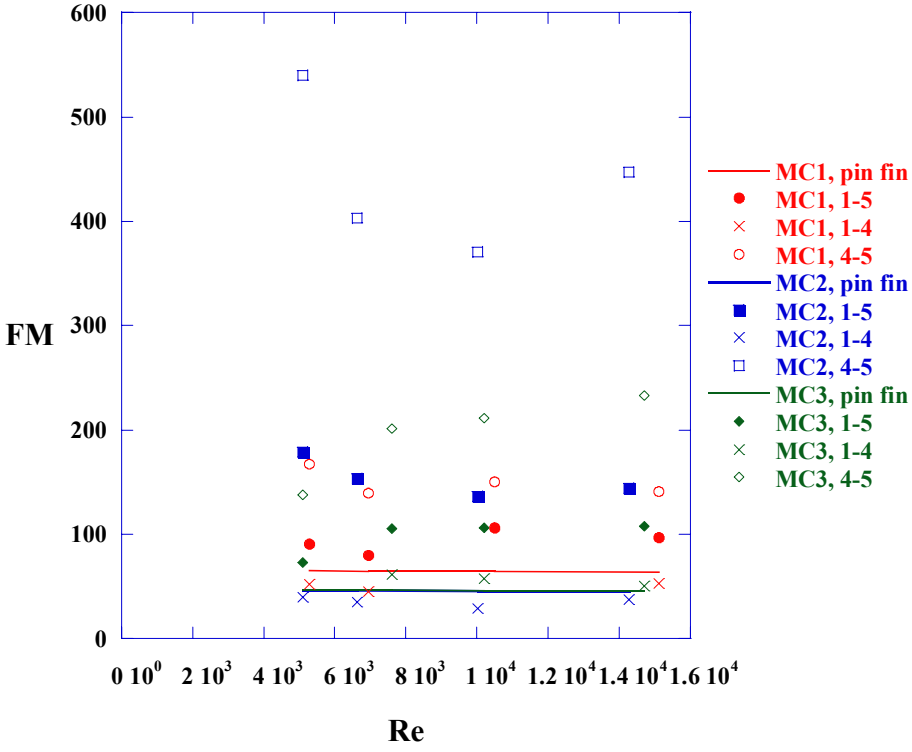

Figure 5-32. A comparison of friction multiplier values shows a wide range of values for the three microcircuit designs (note that MC2 and MC3 calculated FM lie along the same line).

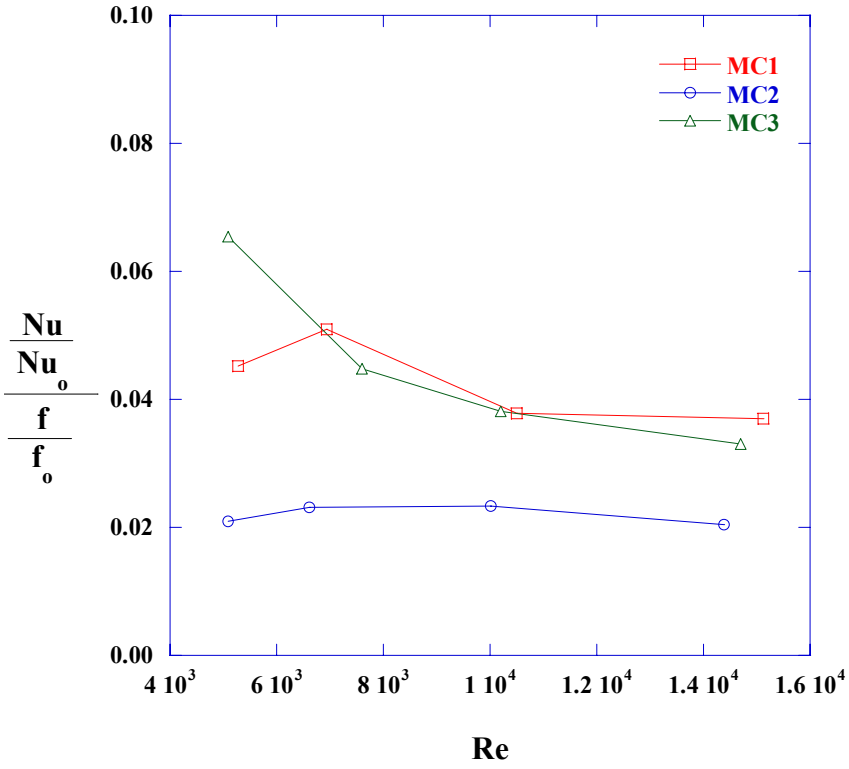

Figure 5-33. Efficiency index provides a measure of how well the design cools for the friction factor penalty incurred.

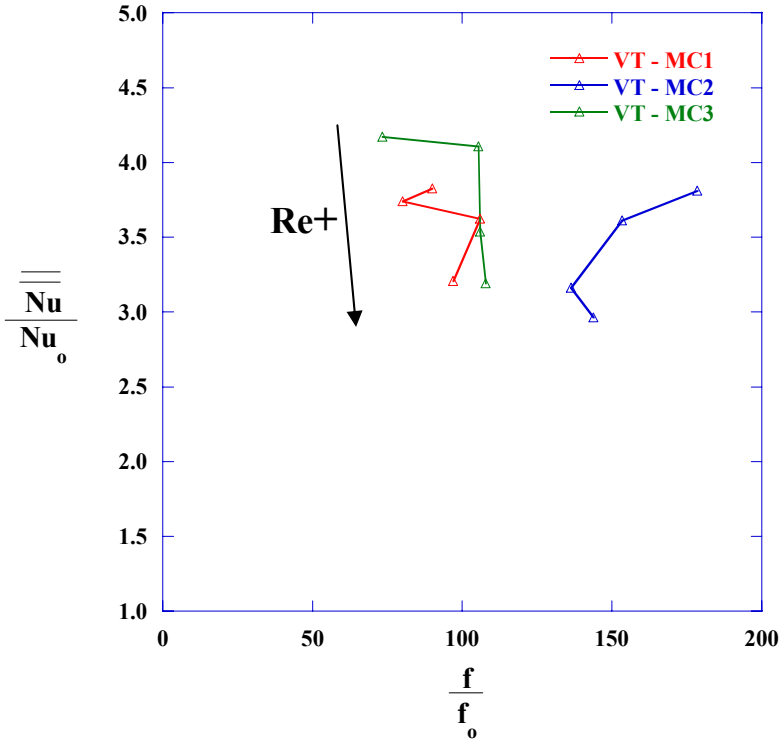

Figure 5-34. A comparison of heat transfer and friction factor augmentations of three microcircuit designs (arrows indicate increasing Reynolds number).

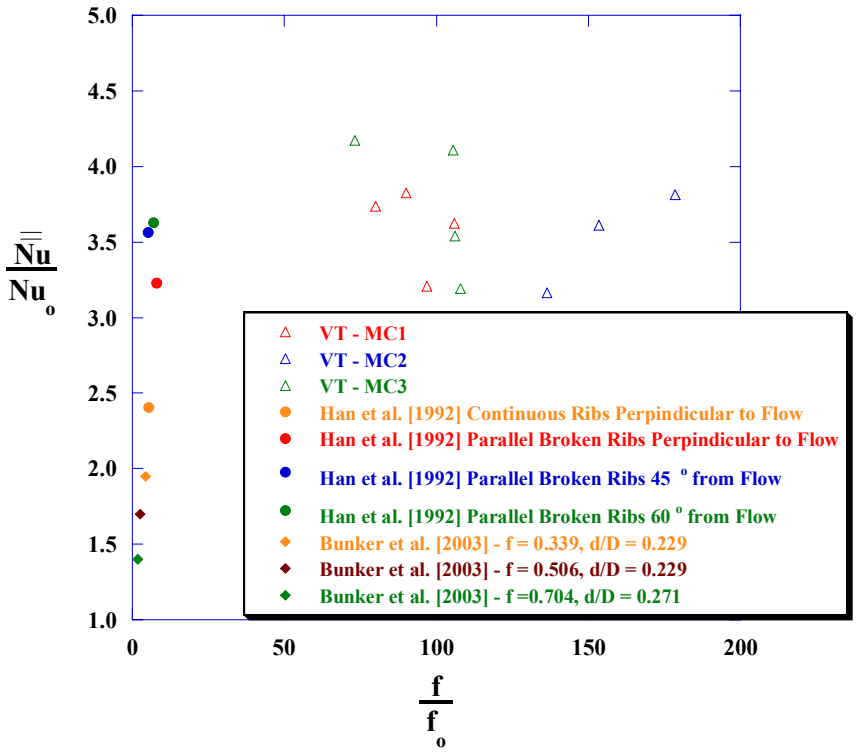

Figure 5-35. Heat transfer versus friction factor augmentation for microcircuit designs, Han [1992], and Chyu [2003] (Microcircuit friction factors are measured across entire microcircuit design).

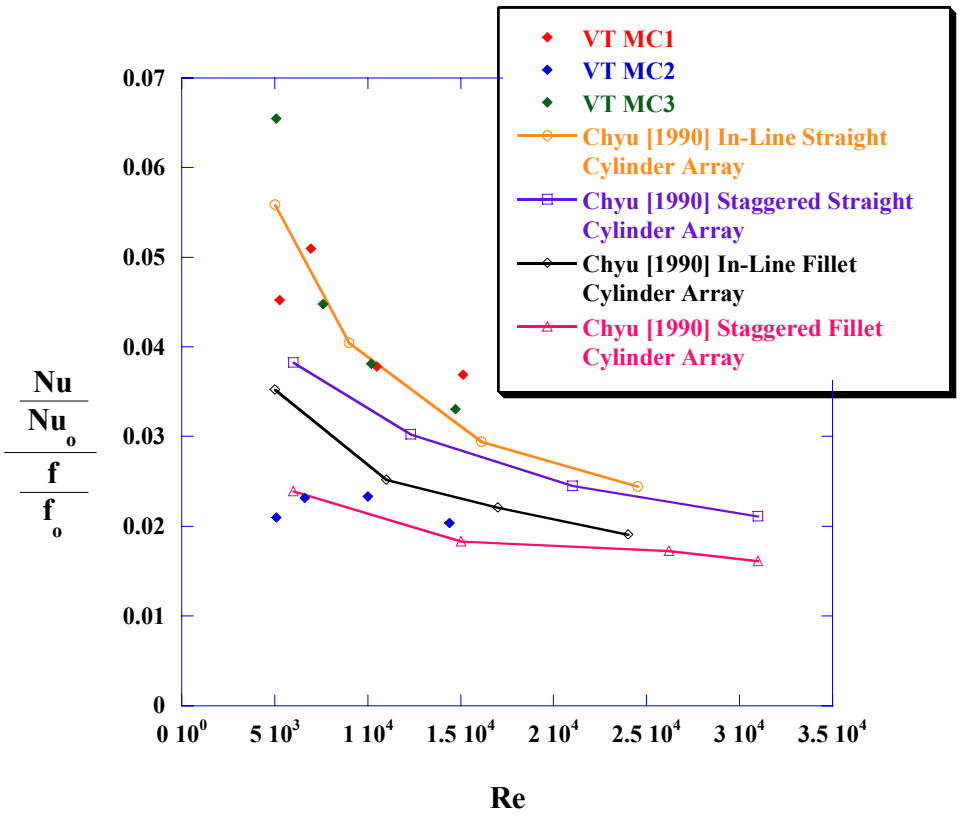

Figure 5-36. Comparison of efficiency index to Chyu [1990] results for filleted and non-filleted pin fin arrays.

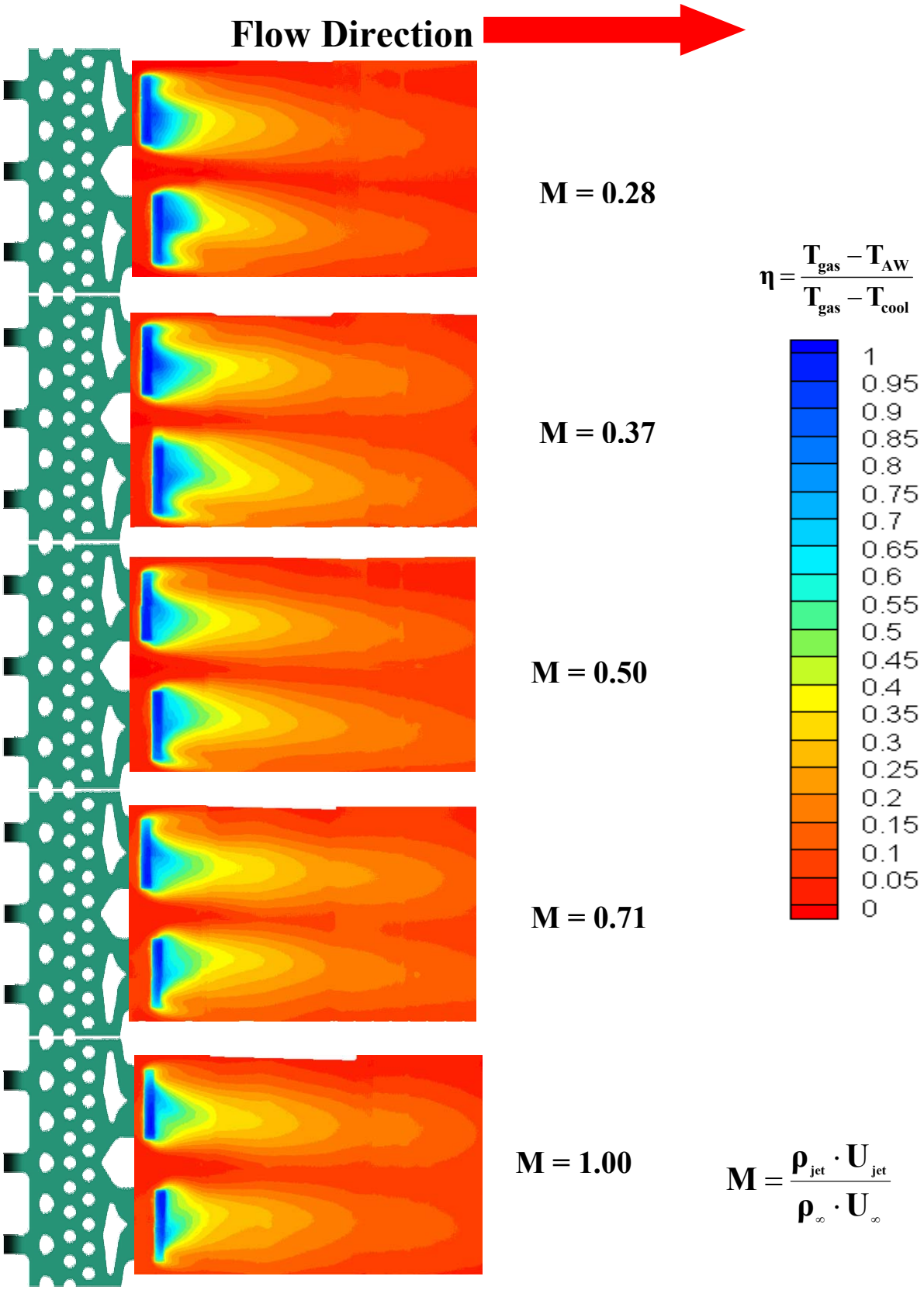

Figure 5-37. MC1 adiabatic film cooling contours

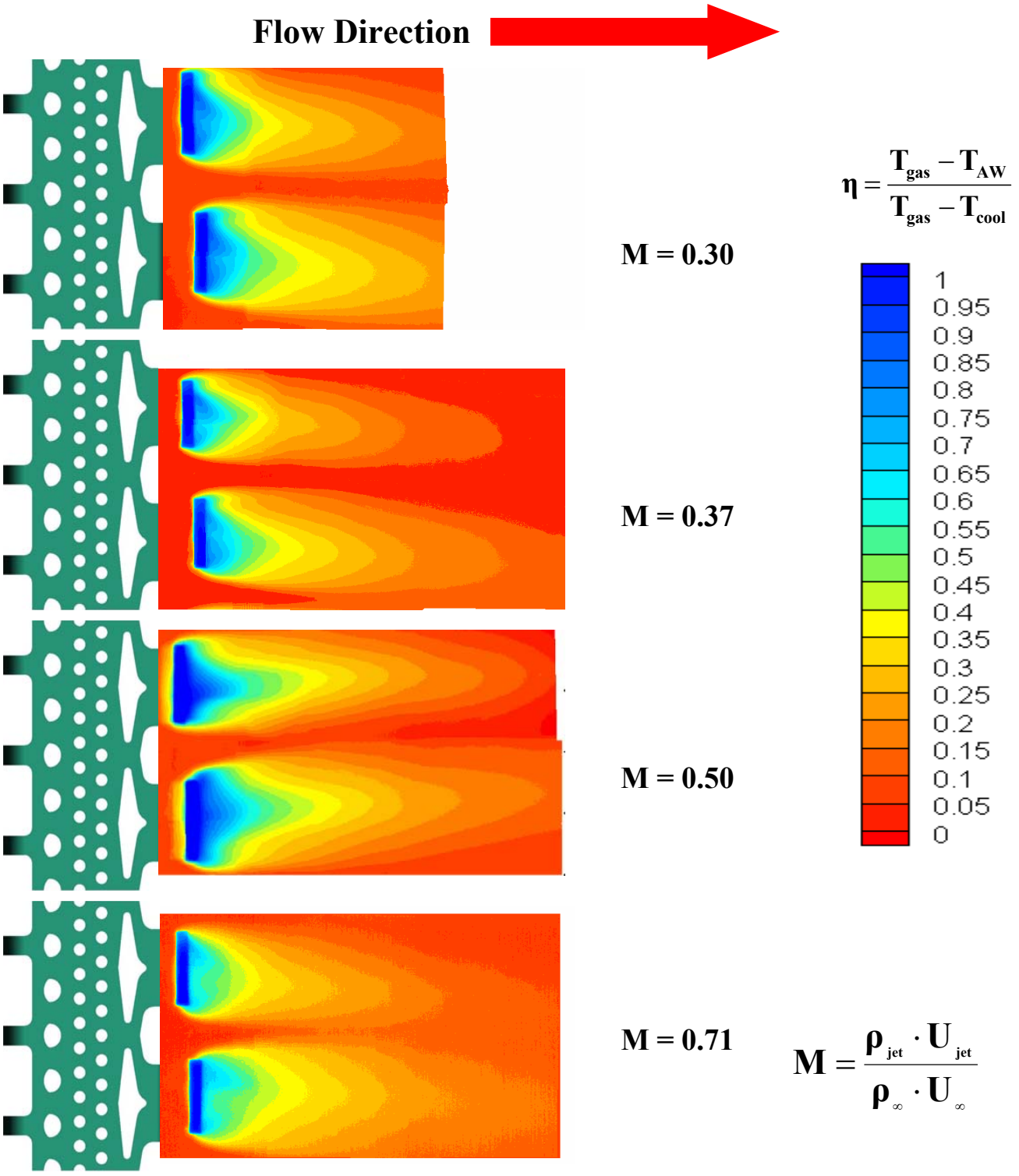

Figure 5-38. MC2 adiabatic film cooling contours.

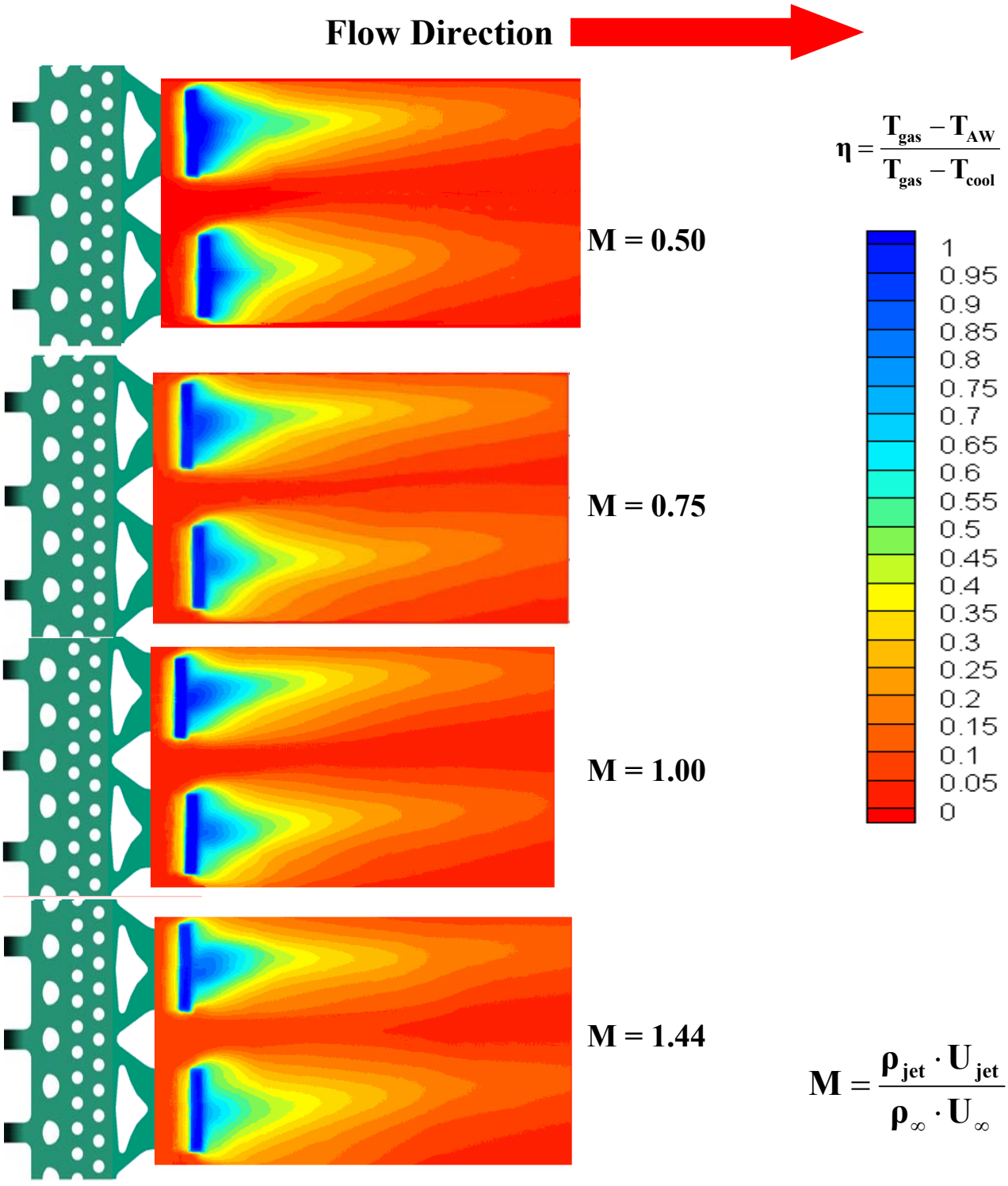

Figure 5-39. MC3 adiabatic film cooling contours.

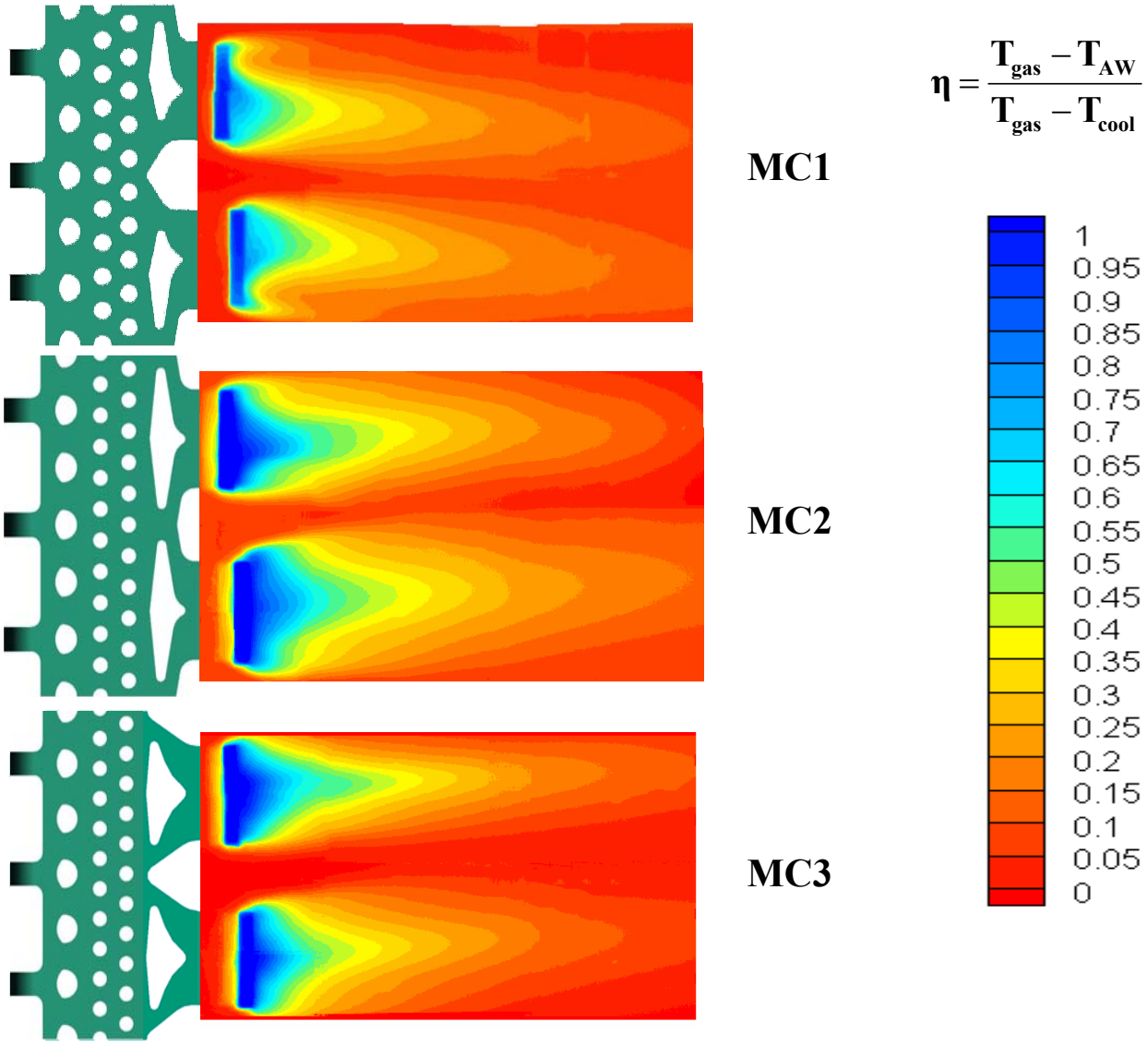

Figure 5-40. Comparison of contours for all microcircuit designs at a blowing ratio of 0.50.

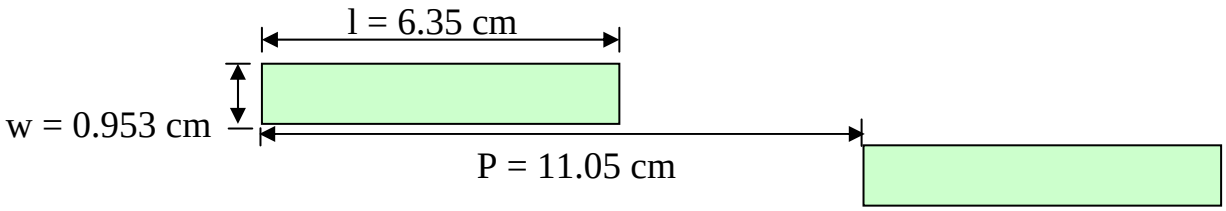

Figure 5-41. Calculation of the geometric parameter s.

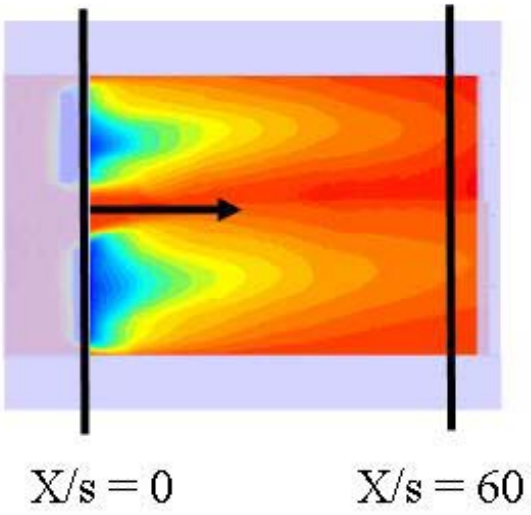

Figure 5-42. Range of data collection for X/s plots.

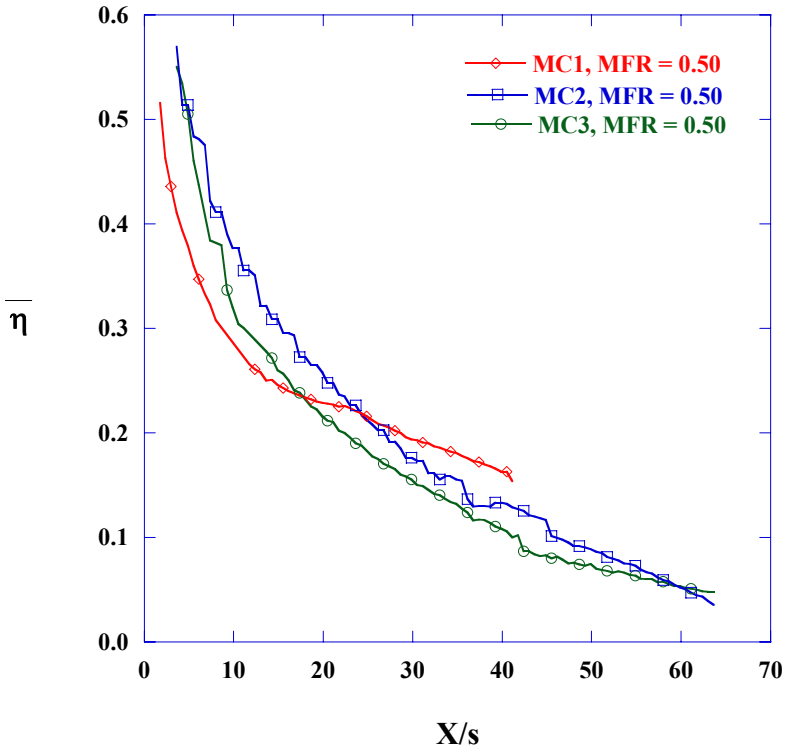

Figure 5-43. Spanwise average η at a blowing ratio of 0.50.

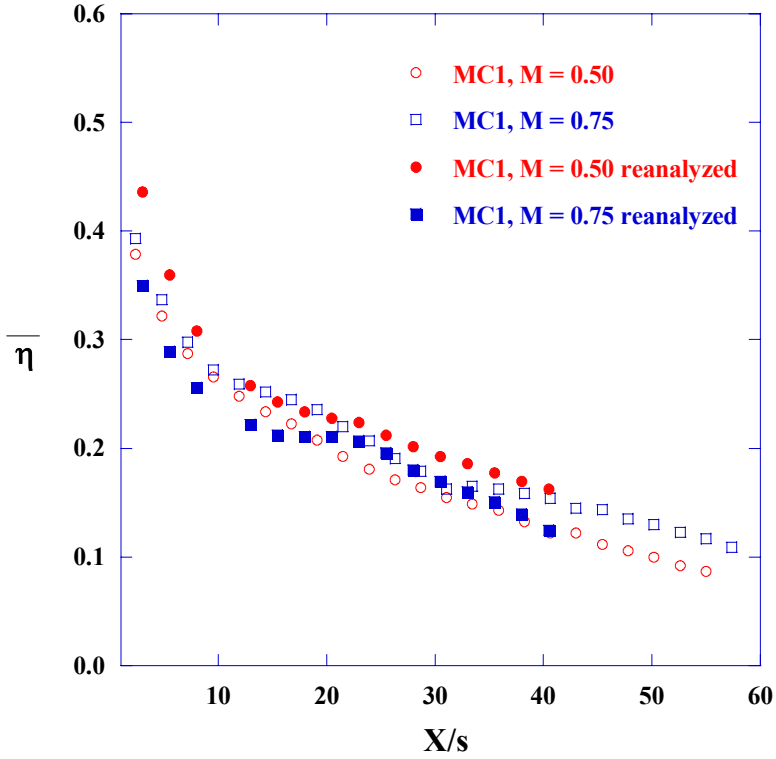

Figure 5-44. Spanwise average η of MC1 before and after data reanalysis.

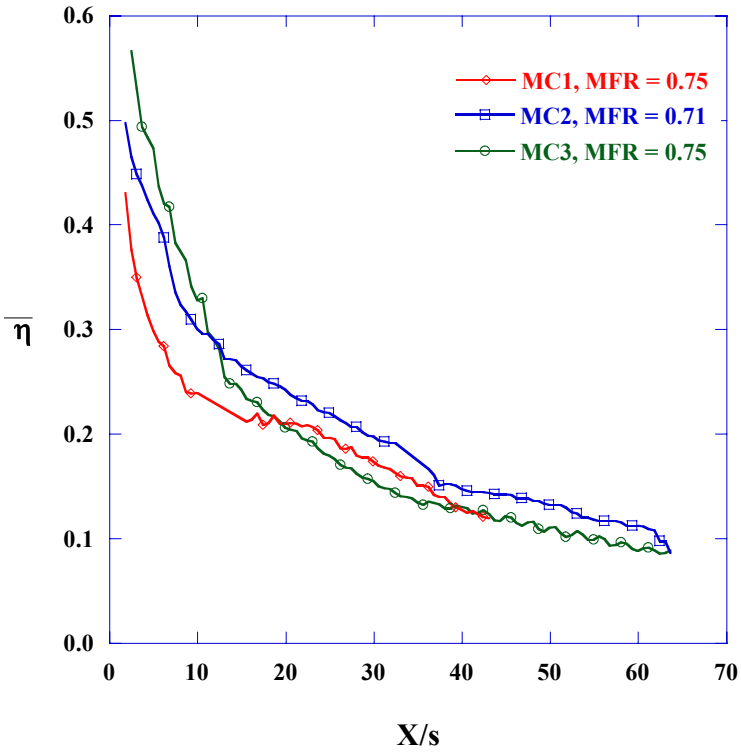

Figure 5-45. Spanwise average η at a blowing ratio of ~ 0.75.

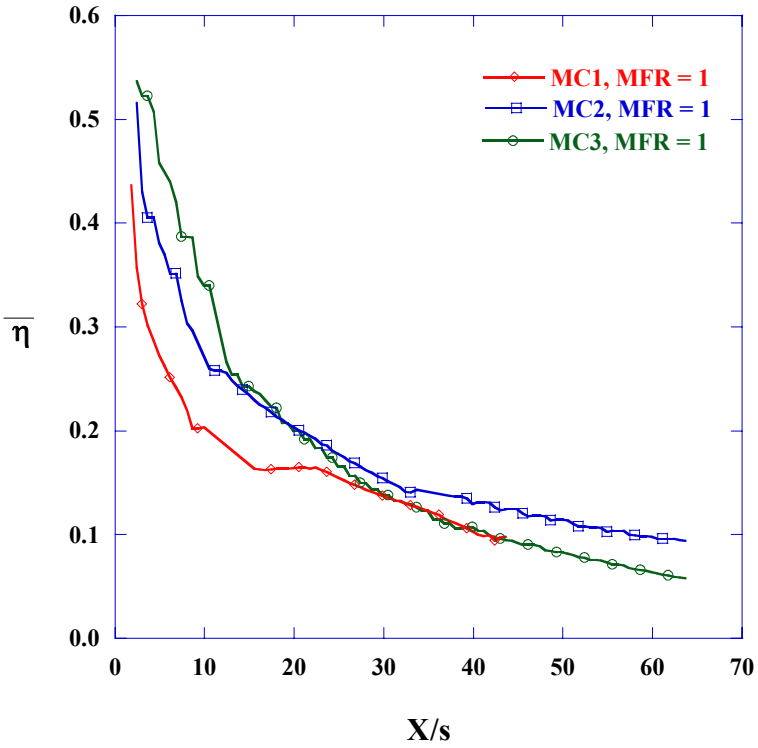

Figure 5-46. Spanwise average η at a blowing ratio of 1.0.

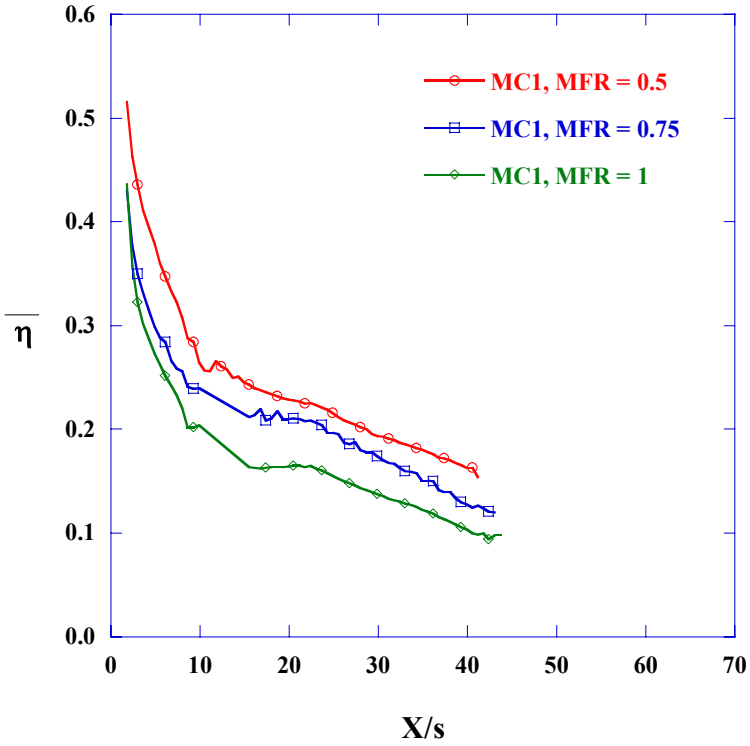

Figure 5-47. Spanwise average η for MC1.

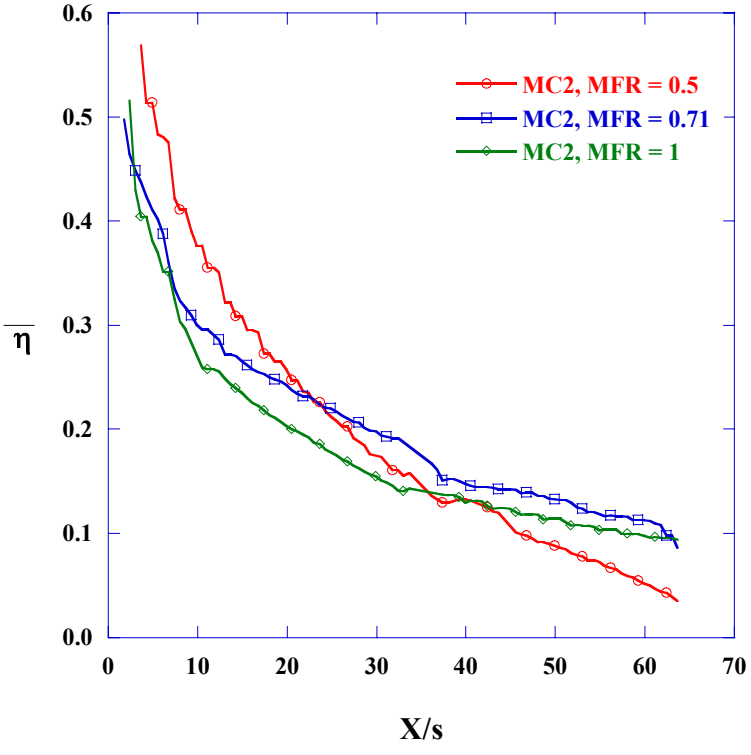

Figure 5-48. Spanwise average η for MC2.

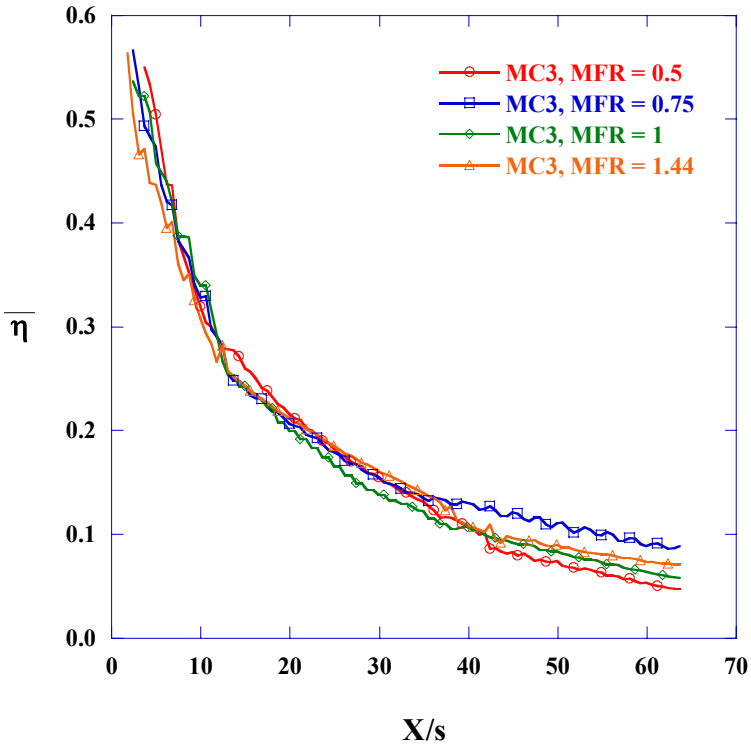

Figure 5-49. Spanwise average η for MC3.

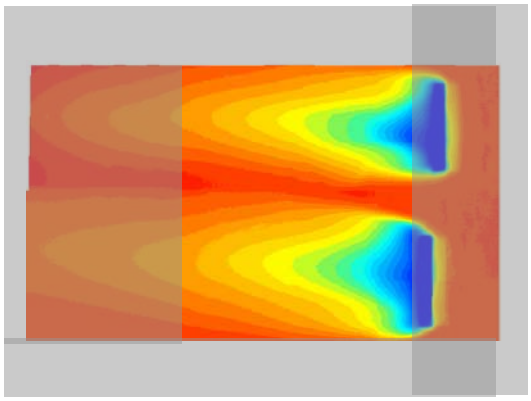

Figure 5-50. Area used to calculate η averages.

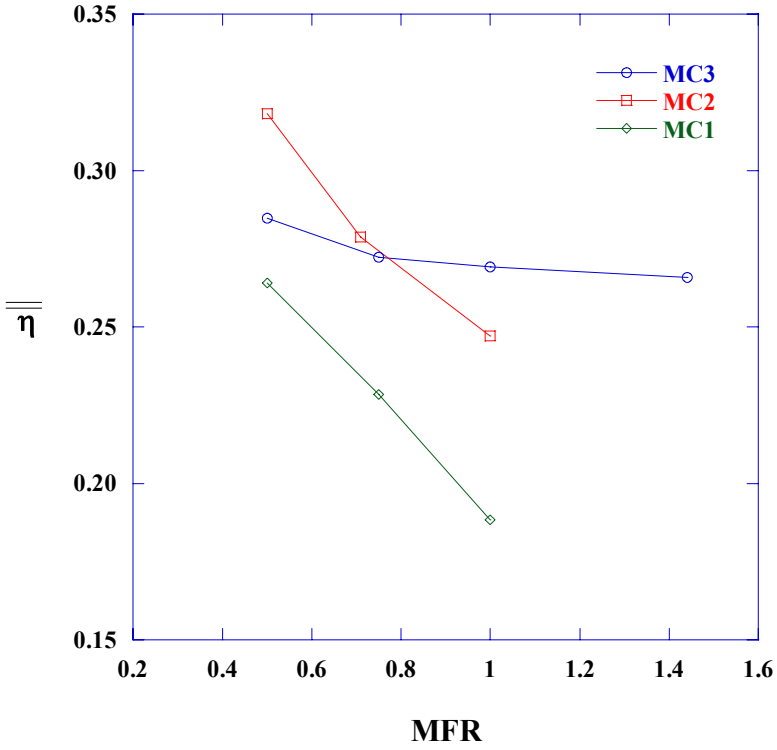

Figure 5-51. Area averaged values of η.

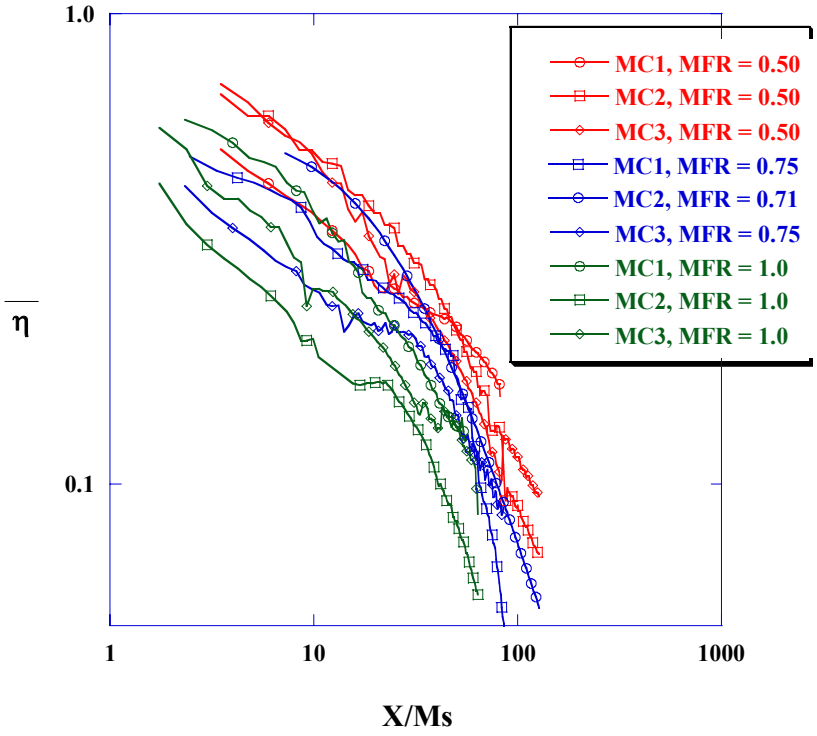

Figure 5-52. Spanwise averaged η values shows a downward trend with increasing MFR that is common to all microcircuit designs (log-log scale).

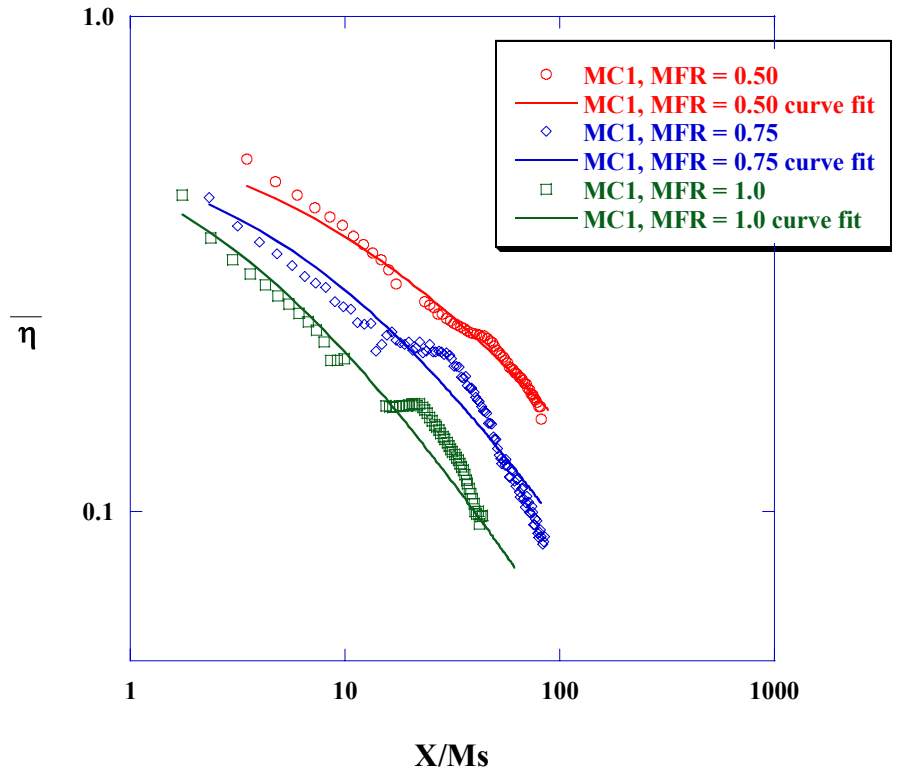

Figure 5-53. Pratt and Whitney construction curves for MC1.

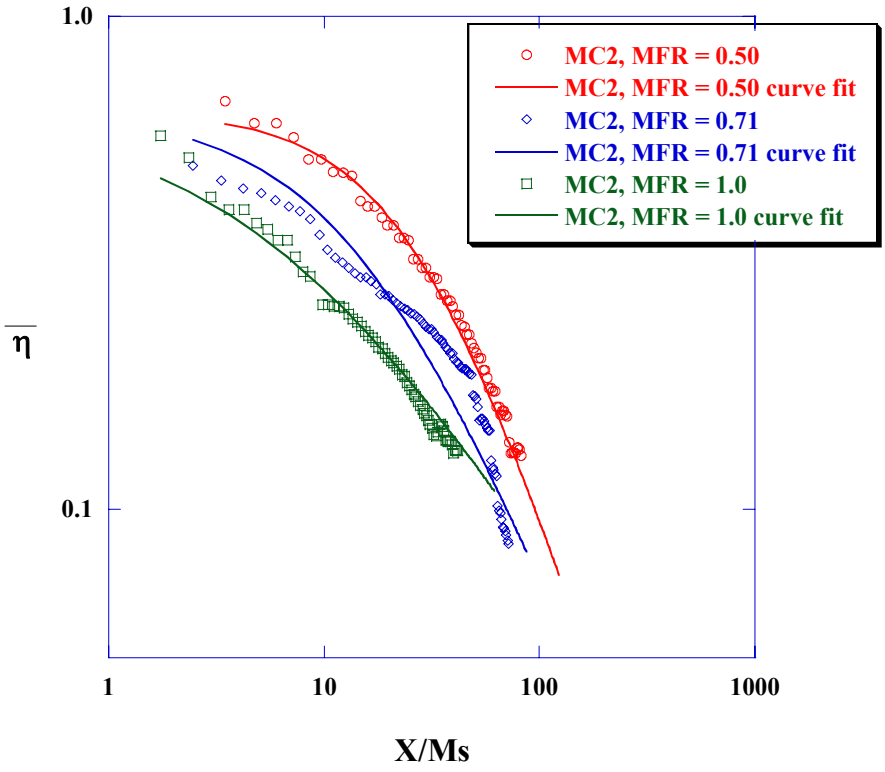

Figure 5-54. Pratt and Whitney construction curves for MC2.

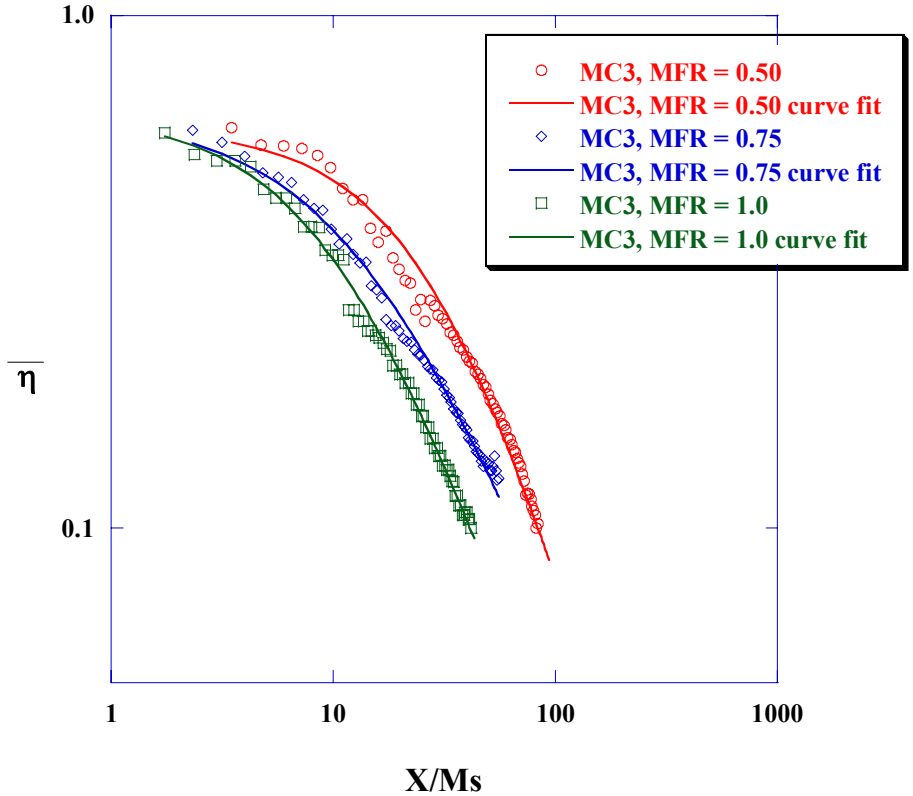

Figure 5-55. Pratt and Whitney construction curves for MC3.

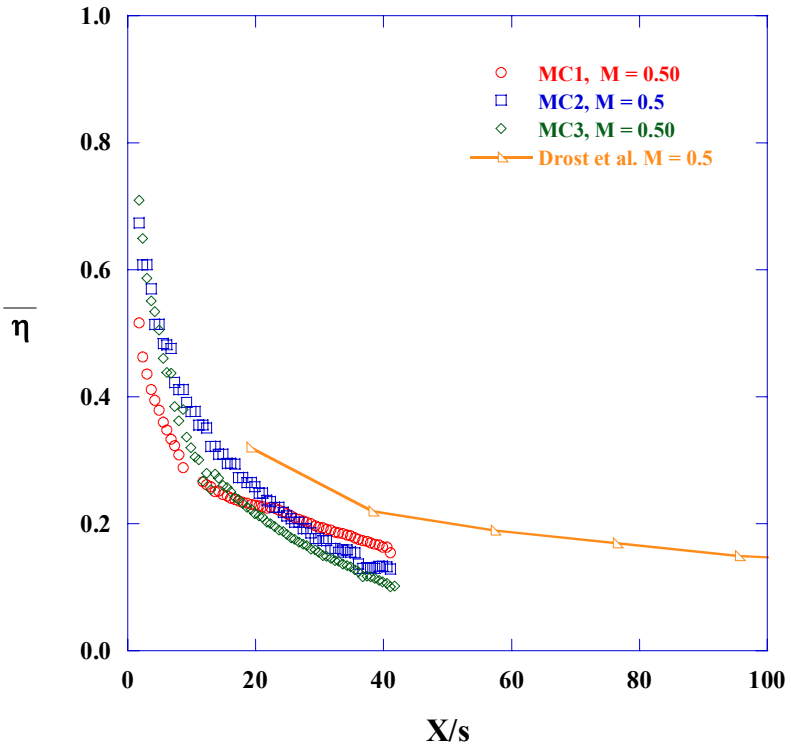

Figure 5-56. Spanwise averaged eta compared to Drost et al. [1997] at an MFR = 0.5.

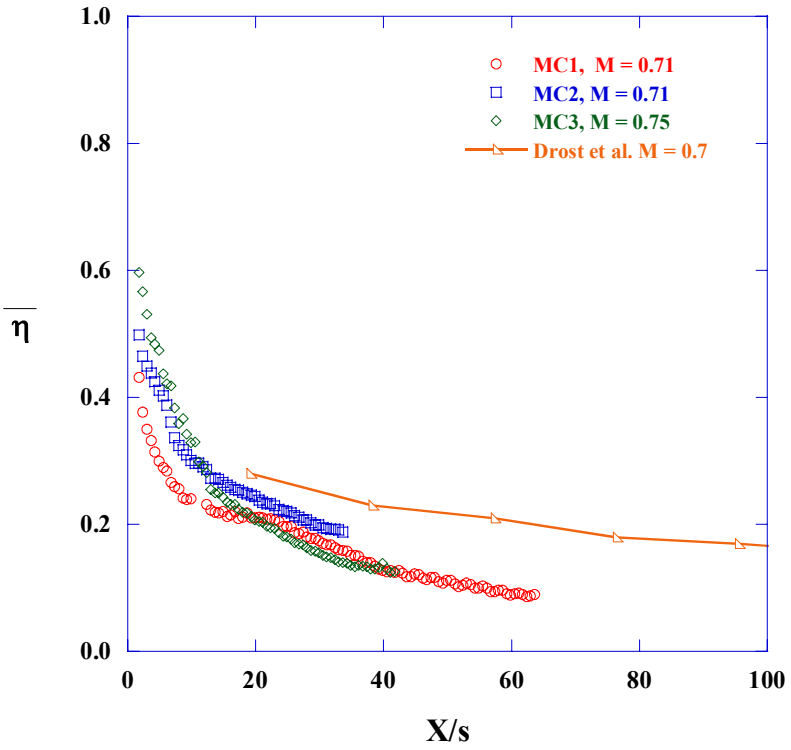

Figure 5-57. Spanwise averaged eta compared to Drost et al. [1997] at an MFR = 0.75.

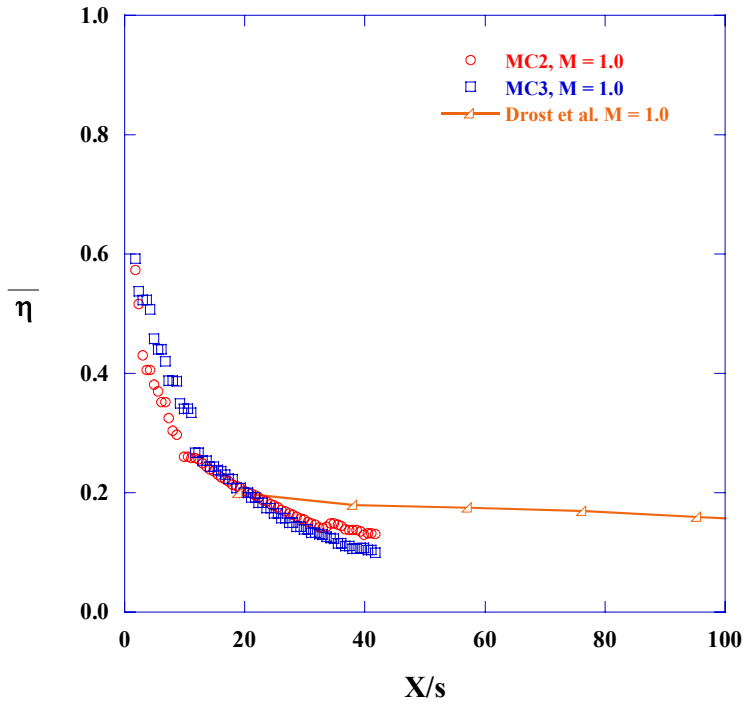

Figure 5-58. Spanwise averaged eta compared to Drost et al. [1997] at an MFR = 1.0.

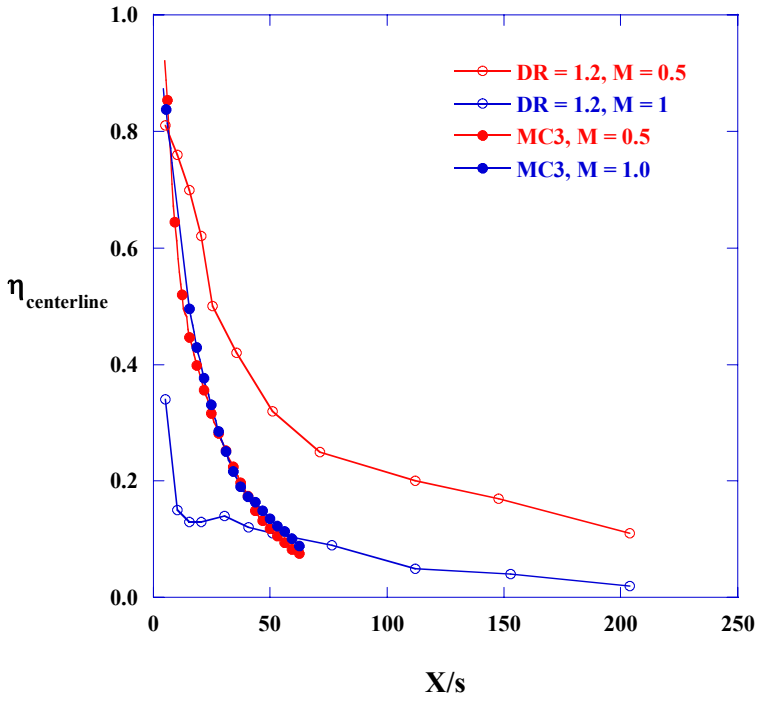

Figure 5-59. A comparison of centerline data to Sinha et al. [1994] shows that the microcircuit values fall between those for hole data at the two different mass flux ratios.

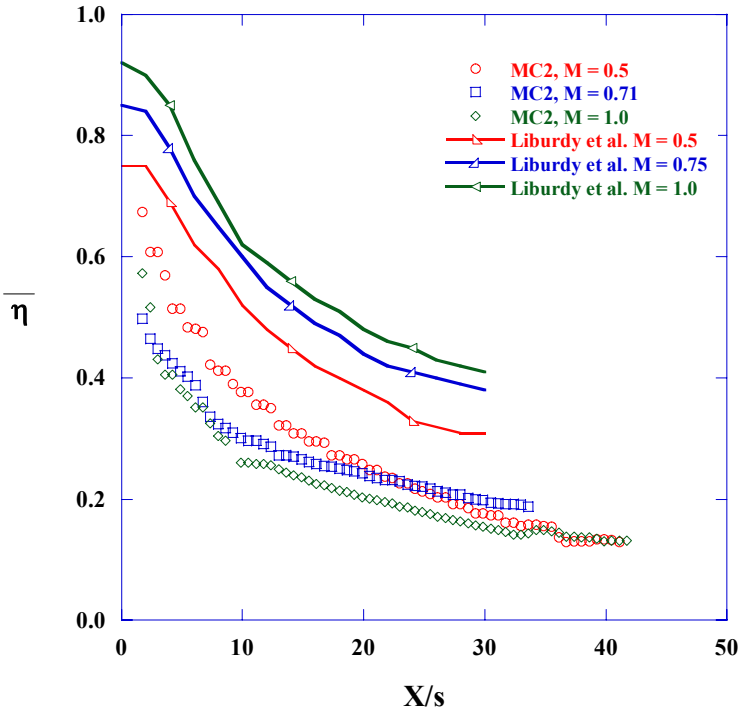

Figure 5-60. Spanwise averaged eta for MC2 compared to Liburdy et al. [1997] for a continuous inclined slot.

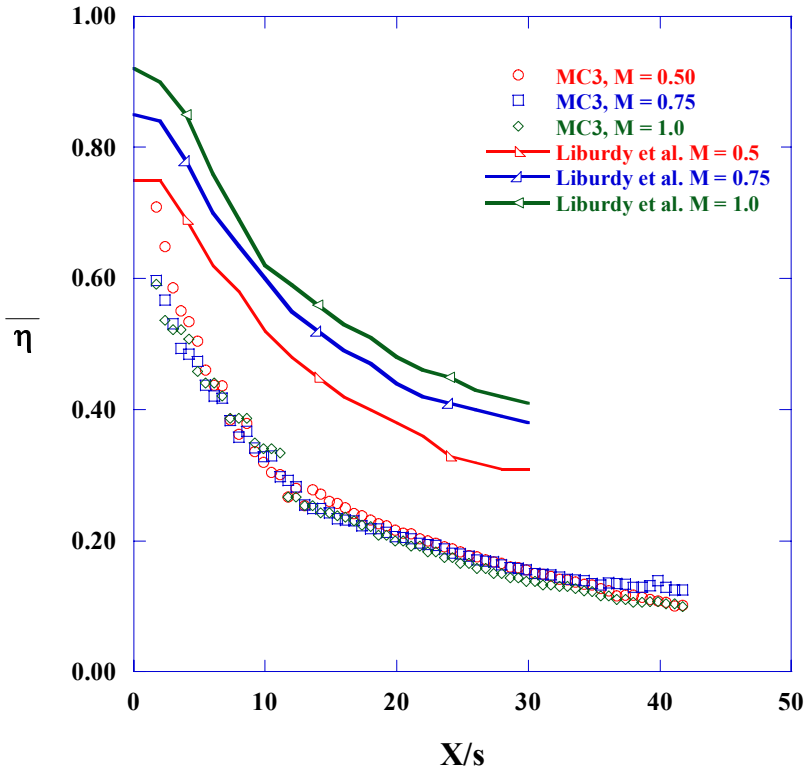

Figure 5-61. Spanwise averaged eta for MC3 comparison to Liburdy et al. [1997] for a continuous inclined slot.

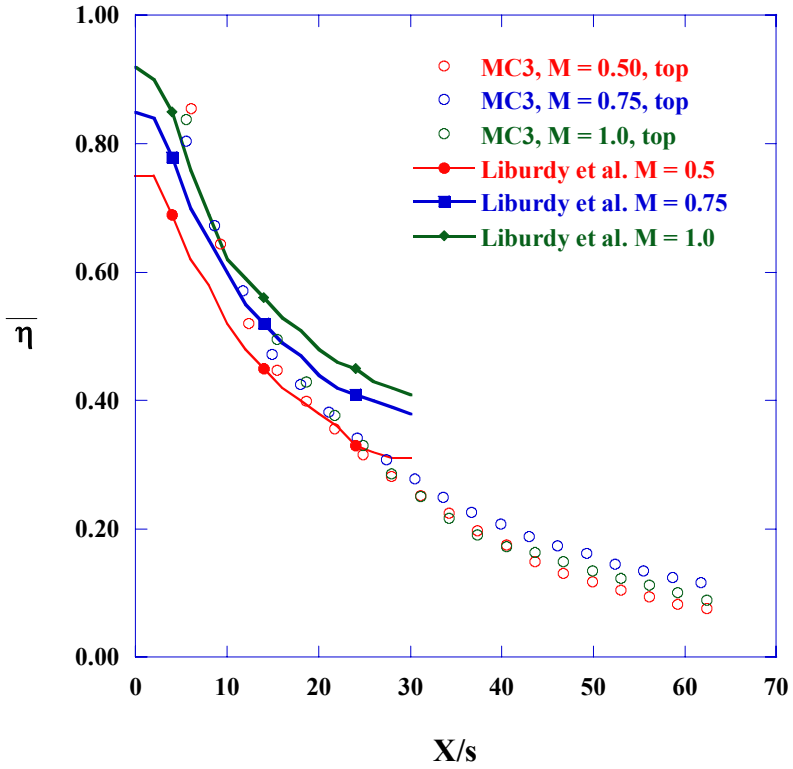

Figure 5-62. A comparison of centerline data to Liburdy et al. [1997] shows good agreement in the near slot region with divergence in the data at high values of X/s.

Chapter 6
Conclusions

Heat transfer and friction factor values have been measured for three innovative cooling designs for use in gas turbine engine blades and vanes. These cooling designs, called microcircuits, are designed for placement internal to blade and vane walls to increase convective cooling. A new test facility was designed and constructed for testing of individual microcircuit designs. The designs were evaluated based on internal convective cooling capabilities, internal friction factors, and external film-cooling effectiveness. The internal heat transfer and friction factors for the microcircuit designs were compared to measurements from pin fin arrays and ribbed or dimpled channels. Similar comparisons were made between film-cooling effectiveness in the current 90° slot case and angled slots and holes from the literature. These comparisons were made to test the viability of microcircuits as compared to more traditional cooling methods. Additionally, comparisons were made among the three microcircuits to provide insight into the design of future microcircuit geometries.

6.1 Overview of Results

The first three rows of the microcircuit designs were similar from design to design. The geometry of the fourth, exit row will be used to characterize each design. The first microcircuit, the asymmetric design, had an asymmetric feature at the exit; the second microcircuit, the small metering area design, had a symmetric exit feature and the smallest metering area; and the third microcircuit design, the diffusing design, had a symmetric feature at the exit that diffused the flow.

In internal heat transfer tests, the diffusing microcircuit enhanced the Nusselt numbers more than the other microcircuit designs, especially at low Reynolds numbers. The small metering area design saw considerably lower values of internal heat transfer

throughout the internal flowpath. The blockage in the small metering area design seems to be the cause of this decreased heat transfer capacity of this design. The diffusing design had the highest area averaged values of heat transfer. Spanwise averages show that at high Reynolds numbers, the asymmetric design followed trends similar to those seen in the diffusing design and even outperformed the diffusing design near the inlets. The directionality of the exit feeds as well as the size of the metering area affected the heat transfer near the exit of the microcircuit. Jets fed by small metering areas mixed more intensely than those that were diffused in the metering areas. An increase in jet mixing caused a corresponding increase in heat transfer near the exit slot.

Current databases that are used by the sponsor to predict heat transfer and frictional losses do not predict microcircuit behaviors. The differences are due to the interaction of the flow with upstream impingement and downstream blockages, in addition to the differences in geometry between a periodic pin fin array and the microcircuit geometry. A comparison of heat transfer augmentation by Reynolds number was also made for each microcircuit, and heat transfer data shows a decrease in heat transfer augmentation with increasing Reynolds number for all microcircuit designs.

The impingement at the microcircuit inlet plays a large role in the variations in heat transfer measurements among the microcircuits. An increase in impingement heat transfer is seen with an increase in the flow metering area. Therefore, the results suggest that decreasing the size of the metering area adversely affects the upstream impingement.

While the microcircuit designs perform quite well in terms of heat transfer, the friction factor values are considerably higher than those measured in other cooling configurations, such as a regular pin fin array and dimpled channels. Friction augmentation values from the first three rows of pin fins were generally lower than those values predicted by the sponsor's program. Values for the whole microcircuit are substantially higher, as would be expected due to the larger flow blockages. A comparison to other data from literature shows that the heat transfer augmentation is of similar magnitude to that measured in a channel with parallel broken ribs. The efficiency index, a measure of the heat transfer augmentation divided by the friction factor penalty incurred, is similar in two of the three microcircuit designs and is much lower in the microcircuit with the small metering area. In a comparison to filleted and non-filleted pin

fin arrays, two of the three microcircuits had efficiency values similar to those for a straight cylinder, in-line array. The efficiency values for the small metering area design are similar to those for a filleted cylinder, staggered array. The efficiency index values measured for the small metering area design are low due to the high values of friction factor augmentation.

In addition to internal heat transfer measurements, external adiabatic effectiveness measurements were made after the microcircuit exit slots. The shape of the film-cooling effectiveness contours varied as a function of the last feature encountered inside the microcircuit channel. The asymmetric design resulted in an asymmetric external cooling pattern, while the symmetric features in the small metering area design and the diffusing design resulted in symmetric cooling patterns. The cooling pattern for the small metering area design was spread more evenly across the exit slot than the cooling pattern for the diffusing design. The jet leaving the slot of the diffusing design was concentrated near the centerline of the slot.

Spanwise averages provide a means of comparing the three microcircuits, and the results show few discernible differences in the spanwise averages by microcircuit design. The spanwise averages do vary by mass flux ratio, especially in the asymmetric design and the small metering area design. These microcircuit designs show higher cooling effectiveness values for lower mass flux ratios. This decrease in cooling effectiveness with increasing mass flux ratio can be attributed to liftoff. Liftoff is the act of air with too much momentum mixing with the mainstream flow, limiting its cooling effectiveness. Previous studies have shown that the slot injection angle is a crucial factor in determining the amount of mixing between the injected coolant and the mainstream flow. The perpendicular direction of the microcircuit coolant, which is mandated by the manufacturing process, directs the coolant momentum directly into the mainstream flow aggravating the effects of mixing.

A comparison of microcircuit data with data from a row of inclined film cooling holes shows lower values for the microcircuit slot. This is attributed to the microcircuit slot flow entering at 90° to the mainstream. A comparison to a continuous, inclined slot finds the microcircuit slot averages to be considerably lower. When compared to

microcircuit centerline data, the data agrees well in the near slot region, but the inclined slot allows the coolant to maintain its effectiveness further downstream.

In conclusion, the results indicate that adiabatic effectiveness is similar for all microcircuit designs, and that while internal features affect the cooling contour shape, the spanwise averaged magnitudes of cooling effectiveness are comparable for all designs. The feasibility of a microcircuit design is therefore dependent on the internal cooling performance and the friction factor values rather than the adiabatic effectiveness.

6.2 Recommendations for Future Testing

One intriguing conclusion of this study is that a decrease in the size of the metering area downstream can adversely effect the upstream impingement cooling. The complicated microcircuit geometry that was tested did not allow for isolation of this effect. Further work to isolate this effect is needed to aid in the design of future generation microcircuits. It is necessary to determine if this impingement effect is a property of other components of the microcircuit design or a function of the metering area alone as these results suggest.

The internal features minimally impacted the external film cooling. Conducting internal tests alongside external tests was not necessary, and the test could be simplified by decoupling these two tests.

The microcircuit designs were very complicated, making it difficult to isolate the effects of the individual features on cooling and on friction factor values. The impingement added another complicating variable in the characterization of the microcircuit flow. The source of some results cannot be attributed to individual features or variables (i.e. impingement) because the behavior of flow around these individual features is unknown. As a consequence, the results of the current testing remain somewhat cryptic. It would be beneficial to further characterize the behavior of individual microcircuit features with and without impingement before continuing the testing of microcircuit designs.

References

Ames, F.E., L.A. Dvorak, M.J. Morrow, 2004, “Turbulent Augmentation of Internal Convection over Pins in Staggered Pin Fin Arrays,” ASME Paper GT2004-53889.

Armstrong, J., and Winstanley, D., 1988, "A Review of Staggered Array Pin Fin Heat Transfer for Turbine Cooling Applications," *Journal of Turbomachinery*, **vol. 110**, pp. 94–103.

Bunker, R.S., J.C. Bailey, C.P. Lee, C.W. Stevens, 2004, “In-Wall Network (Mesh) Cooling Augmentation of Gas Turbine Airfoils,” ASME Paper GT2004-54260.

Bunker, R.S., D.E. Metzger, 1990, “Local Heat Transfer in Internally Cooled Turbine Airfoil Leading Edge Regions: Part I-Impingement Cooling Without Film Coolant Extraction,” *Journal of Turbomachinery*, **vol. 112**, pp.451-458.

Camci, C., K.Kim, 1992, “A New Hue Capturing Technique for the Quantitative Interpretation of Liquid Crystal Images Used in Convective Heat Transfer Studies,” *Journal of Turbomachinery,* **vol. 114**, pg. 765-775.

Chyu, M.K., 1990, “Heat Transfer and Pressure Drop for Short Pin-Fin Arrays with Pin-Endwall Fillet,” Transactions of ASME, **vol. 112**, pp. 926-932.

Coleman, D.A., J. Fernsler, N. Chattham, M. Nakata, Y. Takanishi, E. Korblova, D.R. Link, R.F. Shao, W.G. Jang, J.E. Maclennan, O. Mondainn-Monval, C. Boyer, W. Weissflog, G. Pelzl, L.C. Chien, J. Zasadzinski, J. Watanabe, D.M. Walba, H. Takezoe, and N.A. Clark, 2003, “Polarization-modulated Smectic Liquid Crystal Phases,” *Science*, **vol. 301**, pg. 1204.

Couch, E.L., 2003, “Measurements of Cooling Effectiveness Along the Tip of a Turbine Blade,” Master’s Thesis, Department of Mechanical Engineering, Virginia Polytechnic Insitute and State University.

Cunha, F.J.,2004, “PinFin,” Matlab Code for Pin Fin Array Analysis.

Douglass, C.J., J.S. Kapat, E. Divo, A.J. Kassab, J. Tapley, M. Durham, 2003, “Steady Thermochromic Liquid Crystal Technique for Study of Conjugate Heat Transfer Problems,” ASME Paper GT2003-38587.

Downs, S.J., E.H. James, 1987, “Jet Impingement Heat Transfer – A Literature Survey,” ASME Paper 87-HT-35.

Drost, U., A. Bölcs, A. Hoffs, 1997, “Utilization of the Transiet Liquid Crystal Technique for Film Cooling Effectiveness and Heat Transfer Investigations on a Flat Plate and a Turbine Airfoil,” ASME Paper 97-GT-26.

Farmer, J.P., D.J. Seager, and J.A. Liburdy, 1997,"The Effect of Shaping Inclined Slots on Film Cooling Effectiveness and Heat Transfer Coefficient," ASME Paper 97-GT-339.

Favre-Marinet, M., S.L.Person, A.Bejan, 2004, "Maximum Heat Transfer Rate in Two-Dimensional Minichannels and Microchannels," *Microscale Thermophysical Engineering*, **vol. 8**, pg. 225-337.

Florschuetz, L.W., C.C. Su, 1987, "Effects of Crossflow Temperature on Heat Transfer Within and Array of Impinging Jets," *ASME Journal of Turbomachineray*, **vol. 120**, pg. 92-99.

Goldstein, 1971, "Film Cooling, Advances in Heat Transfer", **vol. 7**, pg. 343-351.

Gritsch, M, A.S. Schulz, S. Wittig, 2001, "Effect of Crossflows on the Discharge Coefficient of Film-Cooling Holes with Varying Angles of Inclination and Orientation," ASME Paper 2001-GT-0134.

Han, J.C., Y.M. Zhang, 1992, "High Performance Heat Transfer Ducts with Parallel, Broken, and V-Shaped Broken Ribs," International Journal of Heat and Mass Transfer, **vol. 35 no.2**, pp. 513-523.

Han, J.C., S. Dutta, S.V. Ekkad, 2000, "Gas Turbine Heat Transfer and Cooling Technology," New York, New York, Taylor & Francis.

Huang, Y., S.V. Ekkad, J.C. Han, 1998, "Detailed Heat Transfer Distributions Under an Array of Orthogonal Impinging Jets," *Journal of Thermophysics and Heat Transfer*, **vol. 12**, No. 1, pg. 73-79.

Ishida, K. and Hamabe, K., 1991, "Effect of Pin Fin Aspect ratio and Arrangement on Heat Transfer and Pressure Drop of Pin Fin Duct for Airfoil Internal Cooling Passage," 91-Yokohama-IGTC-26.

Kays, W.M., M.E. Crawford, 1980, "Convective Heat and Mass Transfer," New York, New York, McGraw-Hill.

Knost, D., 2003, "Film Cooling Predictions and Measurements of Film-Cooling on the Endwall of a First Stage Vane," Master's Thesis, Department of Mechanical Engineering, Virginia Polytechnic Insitute and State University.

Liburdy, J.A., J.P. Farmer, D.J. Seager, 1997, "The Effect of Shaping Inclined Slots on Film-Cooling Effectiveness and Heat Transfer Coefficient," ASME Paper 97-GT-339.

Mattingly, J.D., 1996, "Elements of Gas Turbine Propulsion," New York, New York, McGraw Hill, Inc.

Metzger, D.E., S.W. Haley, 1982, “Heat Transfer Experiments and Flow Visualization for Arrays of Short Pin Fins,” ASME Paper 82-GT-138.

Metzger, D.E., R.A. Berry, J.P. Bronson, 1982, “Developing Heat Transfer in Rectangular Ducts with Staggered Arrays of Short Pin Fins.” *ASME Journal of Heat Transfer*, **vol. 104**, pg. 700-706.

Metzger, D.E., C.S. Fan, S.W. Haley, 1984, “Effects of Pin Shape and Array Orientation on Heat Transfer and Pressure Loss in Pin Fin Arrays,” *Journal of Engineering for Gas Turbines and Power*, **vol. 106**, pp. 252-257.

Munson B.R., D.F. Young, T.H. Okishi, 1998, “Fundamentals of Fulid Mechanics,” 3rd Edition, New York, New York, John Wiley and Sons, Inc.

Obot, N.T., T.A. Trabold, 1987, “Impingement Heat Trasfer Within Arrays of Circular Jets. Part 1: Effects of Minimum, Intermediate, and Complete Crossflow for Small and Large Spacings,” *Journal of Heat Transfer*, **vol.109**, pp. 872-879.

Rhee, D.H., Y.S. Lee, H.H. Cho, 2002, “Film Cooling Effectiveness and Heat Transfer of Rectangular-Shaped Film Cooling Holes,” ASME Paper GT-2002-30168.

Seban, R.A., Chan, H.W., and S.Scesa, 1956, “Heat Transfer to a Turbulent Boundary Layer Downstream of a Slot,” ASME Paper 57-A-336.

Sen, B., D.L. Schmidt, D.G. Bogard, 1996, “Film Cooling with Compound Angle Holes: Heat Transfer,” *ASME Journal of Turbomachinery*, **vol. 118**, pg. 800-806.

Senn, S.M., D. Poulikakos, 2004, “Laminar Mixing, Heat Transfer, and Pressure Drop in Tree-like Mircochannel Nets and their Application for Thermal Management in Polymer Electrolyte Fuel Cells,” Journal of Power Sources, vol. 130, pp. 178-191.

Sinha, A.K., D.L. Schmidt, D.G. Bogard, 1994, “Film Cooling with Compound Angle Holes: Heat Transfer,” ASME Paper, International Gas Turbine Conference, The Hague, Netherlands.

Sinko, G.C., "Pedestal Trailing Edge Design Correlations", Nov, 1986.

Smith, A.C., J.H. Hatchett, A.C. Nix, W.F. Ng, K.A. Thole, 2004, “Effectiveness of Normal and Angled Slot Cooling,” ASME Paper GT2004-53248.

Su, Yao-xi, 1991, “Flow Analysis and Design of Three-Dimensional Wind Tunnel Contractions”, *AIAA Journal*, **vol. 29**, pg. 1912-1919.

Thole, K.A., M. Gritsch, A. Shulz, S. Wittig, 1996, “Transonic Film-Cooling Investigations: Effects of Hole Shapes and Orientations,” ASME Paper 96-GT-222.

Uzol, O., C. Camci, 2001, “Elliptical Pin Fins as an Alternative to Circular Pin Fins for Gas Turbine Blade Cooling Applications, Part 1: Endwall Heat Transfer and Total Pressure Loss Characteristics,” ASME Paper 2001-GT-0181.

VanFossen, G.J., 1982, “Heat-Transfer Coefficients for Staggered Arrays of Short Pin Fins,” *Journal of Engineering for Power*, **vol. 104**, pg.268-274.

Viskanta, R., 1993, “Heat Transfer to Impinging Isothermal Gas and Flame Jets,” *Experimental Thermal and Fluid Science*, **vol. 6**, pg. 111-134.

Wieghardt, K., 1946, “Hot Air Discharge for De-icing,” AAF Translation F-Ts 919-Re, August 1946, Wright Field. Original in Deutsche Luftfahrtforschung: Über das Ausblasen von Warmluft für Enteiser, Forschungsberict Nr. 1900, Zentrale für Wissenschaftliches Berichtswesen, 1943.

Yeh, J.J., M.K. Chyu, 1990, “Heat Transfer of Staggered Pin Fin Arrays.”

Zukauskas, 1972, Advances in heat transfer, **vol.8.**

Appendix A: Friction Multiplier Derivation

The following is a description of PinFin's friction calculation development. PinFin and the following derivation were provided by Cunha [2004].

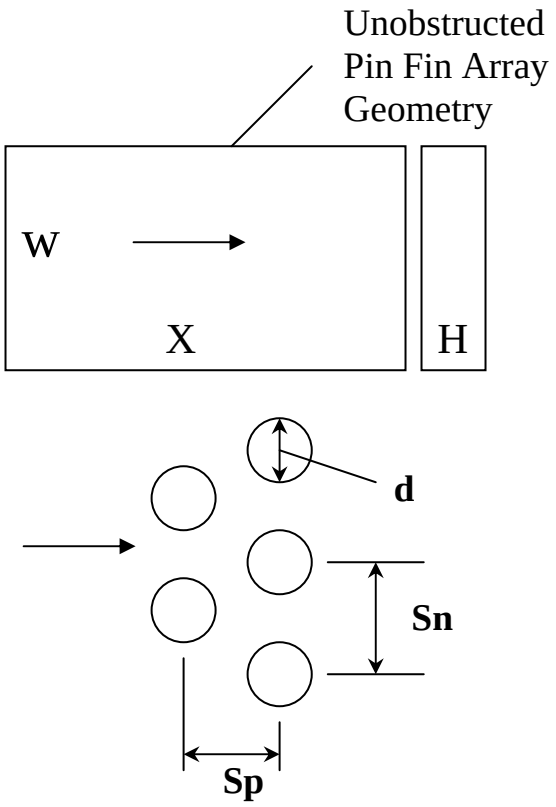

$$A_{min} = (W - N_T d)H \qquad U_{max} = U_{bulk}\frac{A_{bulk}}{A_{min}} \qquad Re_d = \frac{\rho d U_{max}}{\mu}$$

$$F\_per\_row = C_1 C_2 \frac{d}{H} + F_{pin}$$

$$\text{where}: C_1 = \frac{2.132}{Re_d^{0.261}},\ C_2 = \frac{1}{(4\frac{Sn}{d} - 1)},\ F_{pin} = \frac{0.872}{Re_d^{0.278}}$$

$$\Delta P_{per\_row} = 4F\_per\_row\left(\frac{\rho U_{max}^2}{2g}\right);\ \Delta P = N_L \Delta P_{per\_row}$$

$$F_M = \frac{(4F\_per\_row\ N_L)\left(\frac{D_h}{X}\right)\left(\frac{W}{W - N_T d}\right)}{f_o} \quad \text{where} \quad f_o = 0.316 \cdot Re^{-0.25}$$

and for the microcircuit array used in the current study:

$$4 \cdot F\_per\_row = \frac{\Delta P_{static}}{4_{rows}}\left(\frac{2}{\rho \cdot U_{max}^2}\right)$$

$$F_M = \frac{\left(\frac{\Delta P_{static}}{4} \cdot \frac{2}{\rho \cdot U_{max}^2} \cdot N_L\right)\left(\frac{D_h}{X}\right)\left(\frac{1}{1 - d/s_n}\right)^2}{f_o}$$

Appendix B: Heat Exchanger Design Specifications

Super Radiator Coils

Dry Water Coil

Customer:	Virginia Tech	Date:	8/5/2003
Job Ref.:	Air Heating	By:	Jeff Spaeth
Job Item:		Record:	

Dry Water Coil	**Units (Eng.)**	
AirSide:		
Air Flow	Lb/Hr Dry Air	18576
Required Capacity	BTUH	12300
Entering Air Temp.	°F	165.83
Required Air Temp.	°F	167
Airside Pressure	PSIA	14.696

Tubeside:		
Fluid ID		WATER
Fluid Flow Rate	GPM	16.39
Entering Fluid Temp.	°F	180

Coil Selection:		
Model Number		35x35-4R-12/120
Die Surface		1/2 - 1-1/4 x 1.083 Stag.(Corr-#16)
Die Number & Location		16 (All Plants)
Face Area	Ft^2	20.25 4.5ftx4.5ft
Face Velocity	Ft/Min.	244
Number of Circuits		14
Tube Velocity	Ft/Sec.	2
Configuration		Thermal Counterflow
Tube Material		CU
Tube Wall Thickness	In.	0.016
Fin Material		AL
Fin Thickness	In.	0.0055
Header Diam.	In.	1.125

Capacity:		
Rating	BTUH	239,611
Leaving Air Temp.	°F	149.2
Leaving Fluid Temp.	°F	150.1
Fluid Press. Drop	Ft. H2O	4.4
Air Friction	In. H2O	0.26

Figure B-1 Radiator coil specifications, quoted by Jeff Spaeth of Super Radiator Coils.

Appendix C: Contraction Geometry

Table C-1 Contraction Dimensions

Vertical Contraction		Horizontal Contraction	
S_v (cm)	Y_v (cm)	S_h (cm)	Z_h (cm)
0.0	76.5	0.0	76.5
2.5	76.5	2.5	76.5
5.1	76.5	5.1	76.5
7.6	76.5	7.6	76.5
8.9	76.5	8.9	76.5
10.2	76.5	10.2	76.4
11.4	76.4	11.4	76.4
12.7	76.4	12.7	76.3
14.0	76.3	14.0	76.1
15.3	76.2	15.2	75.9
16.6	76.1	16.5	75.6
17.9	75.8	17.8	75.2
19.3	75.6	19.1	74.6
20.8	75.2	20.4	73.9
22.3	74.8	21.8	73.0
24.0	74.2	23.2	71.8
26.0	73.5	24.6	70.4
28.1	72.6	26.2	68.6
30.7	71.5	27.8	66.4
33.6	70.2	29.7	63.8
36.7	68.8	31.6	61.0
39.7	67.5	33.4	58.3
42.5	66.2	35.2	55.7
45.3	65.0	37.0	53.3
48.0	63.8	38.7	50.9
50.5	62.7	40.4	48.7
53.0	61.7	42.0	46.6
55.4	60.6	43.6	44.5
57.7	59.7	45.2	42.6
59.9	58.8	46.8	40.8
62.1	57.9	48.3	39.1
64.2	57.1	49.8	37.4
66.2	56.3	51.3	35.8
68.1	55.6	52.8	34.4
70.0	54.9	54.2	33.0
71.9	54.2	55.7	31.6
73.6	53.6	57.1	30.4
75.4	53.0	58.5	29.2
77.1	52.5	59.9	28.1
78.7	51.9	61.2	27.0

Vertical Contraction		Horizontal Contraction	
S_v (cm)	Y_v (cm)	S_h (cm)	Z_h (cm)
80.3	51.4	62.6	26.0
81.9	51.0	64.0	25.1
83.5	50.5	65.3	24.2
85.0	50.1	66.6	23.3
86.5	49.7	68.0	22.6
88.0	49.4	69.3	21.8
89.4	49.0	70.6	21.1
90.8	48.7	71.9	20.5
92.2	48.4	73.2	19.9
93.6	48.1	74.5	19.3
96.4	47.6	77.1	18.3
99.0	47.2	79.7	17.4
101.7	46.8	82.3	16.7
104.3	46.5	84.8	16.0
106.9	46.2	87.4	15.5
109.5	46.0	89.9	15.0
112.1	45.8	92.5	14.6
114.6	45.6	95.0	14.3
117.2	45.5	97.6	14.0
119.7	45.4	100.1	13.8
122.3	45.3	102.6	13.6
124.8	45.2	105.2	13.4
127.4	45.2	107.7	13.3
129.9	45.1	110.3	13.2
132.5	45.1	112.8	13.2
135.0	45.1	115.3	13.1
137.5	45.0	117.9	13.1
140.1	45.0	120.4	13.0
142.6	45.0	123.0	13.0
145.2	45.0	125.5	13.0
147.7	45.0	128.0	13.0
150.2	45.0	130.6	13.0
152.8	45.0	133.1	13.0
155.3	45.0	135.7	13.0
157.9	45.0	138.2	13.0
160.4	45.0	140.7	13.0
162.9	45.0	143.3	13.0
165.5	45.0	145.8	13.0
168.0	45.0	148.4	13.0

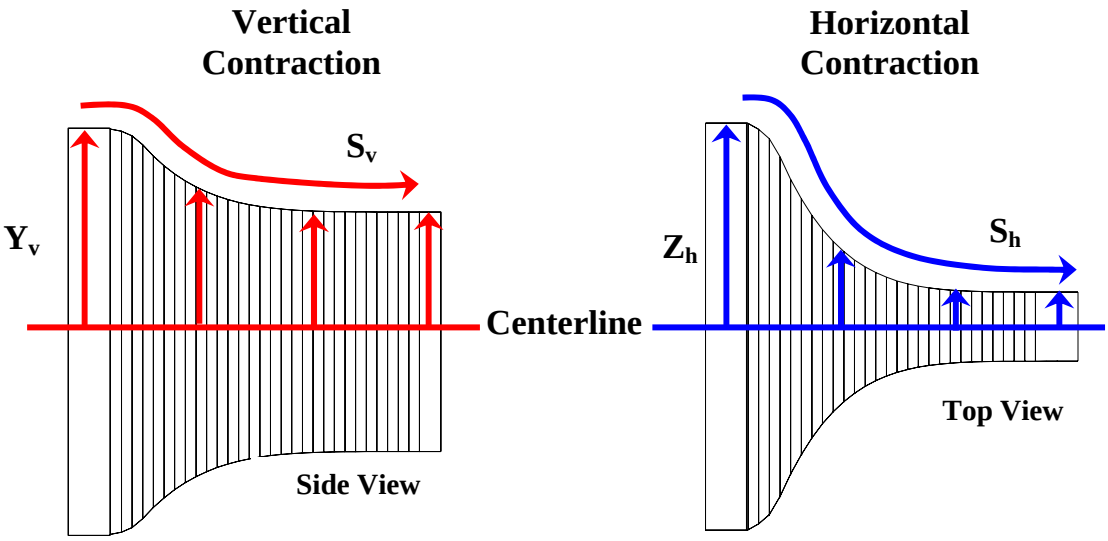

Figure C-1 Contraction dimension specifics

Appendix D: Experimental Uncertainty Calculations

This appendix presents the uncertainty analysis for Nu, f, and η.

Uncertainty for Nusselt Number, Nu

$$Nu = \frac{h \cdot D_H}{k} = \frac{q_{conv} \cdot D_H}{A_H \cdot k(T_{wall} - T_m)}$$

$$q_{conv} = q_{total} - q_{cond} = \frac{V^2 \cdot R}{R_R^2 \cdot A_H} - \frac{T_{wall} - T_{amb}}{\frac{1}{h_{free}} + \frac{t_{glass}}{k_{glass}}}$$

$$u_{q_{conv}} = \sqrt{\left(\frac{\partial q_{conv}}{\partial V} \cdot u_V\right)^2 + \left(\frac{\partial q_{conv}}{\partial R_H} \cdot u_{R_H}\right)^2 + \left(\frac{\partial q_{conv}}{\partial R_r} \cdot u_{R_r}\right)^2 + \left(\frac{\partial q_{conv}}{\partial A_H} \cdot u_{A_H}\right)^2 + \cdots + \left(\frac{\partial q_{conv}}{\partial T_{wall}} \cdot u_{T_{wall}}\right)^2 + \left(\frac{\partial q_{conv}}{\partial T_{amb}} \cdot u_{T_{amb}}\right)^2}$$

$$u_{Nu_{conv}} = \sqrt{\left(\frac{\partial Nu}{\partial q_{conv}} \cdot u_{q_{conv}}\right)^2 + \left(\frac{\partial Nu}{\partial D_H} \cdot u_{D_H}\right)^2 + \left(\frac{\partial Nu}{\partial A_H} \cdot u_{A_H}\right)^2 + \left(\frac{\partial Nu}{\partial T_{wall}} \cdot u_{T_{wall}}\right)^2 + \left(\frac{\partial Nu}{\partial T_m} \cdot u_{T_m}\right)^2 + \cdots + \left(\frac{\partial Nu}{\partial D_H} \cdot u_{D_H}\right)^2 + \left(\frac{\partial Nu}{\partial k} \cdot u_k\right)^2}$$

High Re, High Nu

Variable	Value	Precision Uncertainty	Bias Uncertainty	Total Uncertainty
Nu	160	-	-	3.43 (2.1%)
q_{conv}	1797	-	-	37
D_h	0.01906	-	-	5.E-05
A_h	0.0774	-	-	5.E-05
T_{meas}	34.1	0.063	0.33	0.337
T_{fluid}	25.8	0.3	0.2	0.36
k	0.026	-	-	5.E-04

High Re, Low Nu

Variable	Value	Precision Uncertainty	Bias Uncertainty	Total Uncertainty
Nu	88.4	-	-	2.94 (3.3%)
q_{conv}	1222	-	-	24
D_h	0.01906	-	-	5.E-05
A_h	0.0774	-	-	5.E-05
T_{meas}	34.2	0.063	0.33	0.337
T_{fluid}	24.04	0.3	0.36	0.36
k	0.026	-	-	5.E-04

Low Re, High Nu

Variable	Value	Precision Uncertainty	Bias Uncertainty	Total Uncertainty
Nu	128.3	-	-	4.04 (3.1%)
q_{conv}	1322	-	-	43.5
D_h	0.01906	-	-	5.E-05
A_h	0.0774	-	-	5.E-05
T_{meas}	33.24	0.063	0.33	0.337
T_{fluid}	26.1	0.3	0.36	0.36
k	0.026	-	-	5.E-04

Low Re, Low Nu

Variable	Value	Precision Uncertainty	Bias Uncertainty	Total Uncertainty
Nu	65	-	-	3.24 (4.9%)
q_{conv}	791.1	-	-	21.8
D_h	0.01906	-	-	5.E-05
A_h	0.0774	-	-	5.E-05
T_{meas}	33.69	0.063	0.33	0.337
T_{fluid}	23.15	0.3	0.36	0.36
k	0.026	-	-	5.E-04

Uncertainty for friction factor, f

$$f = \left(\frac{\Delta P_{static}}{\rho_{bulk}} + \frac{U_{bulk}^2 - U_{out}^2}{2} \right) \cdot \left(\frac{D_h}{X} \right) \cdot \left(\frac{2}{U_{bulk}^2} \right)$$

$$u_f = \sqrt{\left(\frac{\partial f}{\partial \Delta P_{static}} \cdot u_{\Delta P_{static}} \right)^2 + \left(\frac{\partial f}{\partial \rho_{bulk}} \cdot u_{\rho_{bulk}} \right)^2 + \left(\frac{\partial f}{\partial U_{bulk}} \cdot u_{U_{bulk}} \right)^2 + \ldots \ldots + \left(\frac{\partial f}{\partial U_{max}} \cdot u_{U_{max}} \right)^2 + \left(\frac{\partial f}{\partial \left(L/D_h \right)} \cdot u_{\left(L/D_h \right)} \right)^2}$$

High Re case

Variable	Value	Precision Uncertainty	Bias Uncertainty	Total Uncertainty
f	0.971	-	-	0.018 (1.9%)
ΔP_{static} (Pa)	304.7	1.77	0.174	1.78
ρ_{bulk} (kg/m3)	1.132	-	-	0.006
U_{bulk} (m/s)	12.85	-	-	0.316
U_{max} (m/s)	26.13	-	-	1.27
L/D_h	5.61	0.0005	-	0.0005

Low Re case

Variable	Value	Precision Uncertainty	Bias Uncertainty	Total Uncertainty
f	1.029	-	-	0.0007 (1.9%)
ΔP_{static} (Pa)	44.187	0.124	0.62	0.634
ρ_{bulk} (kg/m3)	1.125	-	-	0.0009
U_{bulk} (m/s)	4.5	-	-	0.108
U_{max} (m/s)	9.1	-	-	0.439
L/D_h	5.61	0.0005	-	0.0005

Uncertainty for eta, η

$$\eta = \frac{T_\infty - T_{AW}}{T_\infty - T_C}$$

$$u_\eta = \sqrt{\left(\frac{\partial \eta}{\partial T_\infty} \cdot u_{T_\infty}\right)^2 + \left(\frac{\partial \eta}{\partial T_{AW}} \cdot u_{T_{AW}}\right)^2 + \left(\frac{\partial \eta}{\partial T_C} \cdot u_{T_C}\right)^2}$$

$$\frac{\partial \eta}{\partial T_{AW}} = \frac{1}{T_\infty - T_C}$$

$$\frac{\partial \eta}{\partial T_\infty} = \frac{T_{AW} - T_\infty}{(T_\infty - T_C)^2} + \frac{1}{T_\infty - T_C}$$

$$\frac{\partial \eta}{\partial T_\infty} = \frac{T_\infty - T_{AW}}{(T_\infty - T_C)^2}$$

Low value of η

Variable	Value	Precision Uncertainty	Bias Uncertainty	Total Uncertainty
η	0.22	-	-	0.041 (19%)
T_{AW}	48.44	0.465	0.969	1.074
T_{inf}	54.68	0.63	0.2	0.658
T_c	25.75	0.121	0.2	0.234

High value of η

Variable	Value	Precision Uncertainty	Bias Uncertainty	Total Uncertainty
η	0.9	-	-	0.337 (3.7%)
T_{AW}	28.58	0.595	0.572	0.825
T_{inf}	54.68	0.63	0.2	0.658
T_c	25.75	0.121	0.2	0.234

Appendix E: Calculation of theoretical TAW

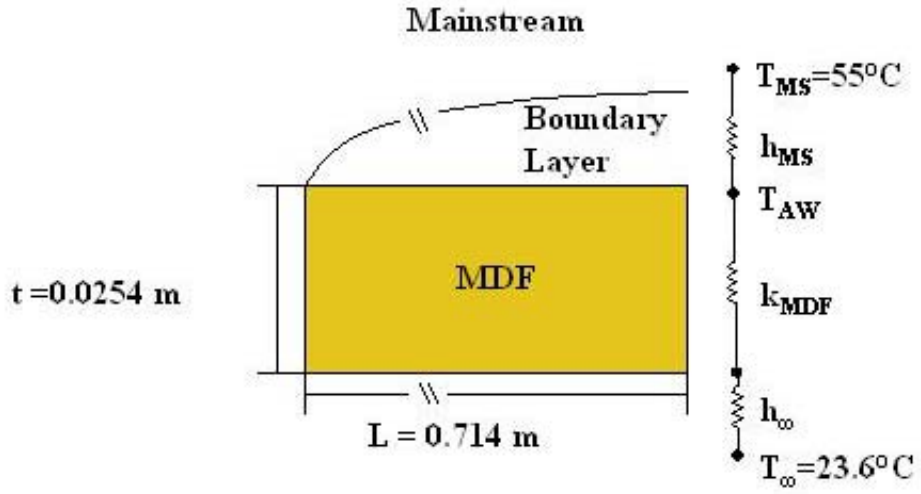

$h_\infty = 5$ W/K
$k_{MDF} = 0.4$ W/mK
$k_{air} = 0.6$ W/mK

$$Nu_x = 0.332 \cdot Re_x^{1/2} \cdot Pr^{1/3}$$

$$Nu_x = \frac{h_{MS} \cdot L}{k_{air}}$$

$h_{MS} = 159$ W/K

$$q'' = \frac{T_{MS} - T_\infty}{\left(\frac{1}{h_\infty} + \frac{t}{k_{MDF}} + \frac{1}{h_{MS}}\right)}$$

$q'' = 116$ W

The heat flux can be used to calculate T_{AW} for use in eta calculations.

$$q'' = \frac{T_{AW} - T_\infty}{\left(\frac{t}{k_{MDF}} + \frac{1}{h_\infty}\right)}$$

Appendix F: Conversion of Chyu [1990] data for comparison with VTExCCL Data

Chyu's [1990] data was originally presented with D'arcy friction factor on top, while a Fanning baseline friction factor was used as the normalization factor. Another inconsistency between the Chyu [1990] data and VTExCCL data is that Chyu used U_{max} (the velocity between pin fins) as the velocity while by definition this value should be U_{bulk} (the velocity of the open channel flow). To compare the two data sets, the following conversion was applied to the Chyu [1990] data to make the data sets comparable.

Definitions:

$$f_{VT} = \left(\frac{\Delta P}{\rho}\right)\cdot\left(\frac{2\cdot D_h}{L\cdot U_{bulk}^2}\right)$$

$$f_{Chyu} = \left(\frac{\Delta P}{\rho}\right)\cdot\left(\frac{2}{U_{max}^2}\right)\left(\frac{1}{N}\right)$$

The friction factor definition does not match the baseline friction factor, and for comparison to VT data these two much match. The D'arcy friction factor on top was multiplied by 0.25 to convert to Fanning friction factor. VT used D'arcy friction factor for data and for the baseline values.

The Chyu data must also be multiplied by the following conversion factor: $N\left(\frac{D_h}{L}\right)$

where N = 7, D_h = 23.5 mm, and L = 222.25 mm.

The Chyu [1990] friction factors were normalized with U_{max} while the VTExCCL data was normalized using U_{bulk}. The volumetric flow is constant in the pin fin and bulk regions of the microcircuit, and as a result the velocities are inversely proportional to the flow areas. The ratio of the areas was calculated based on the total width of the channel (W), the number of pin fins in the transverse direction (N_T), and the diameter of the pin fins (D). The depth of the channels is the same in both cases, so the ratio of the spanwise lengths is equivalent to the ratio of the areas.

$$\frac{A_{bulk}}{A_{max}} = \left[\frac{W}{W - N_T\cdot D}\right]$$

$$\frac{U_{max}^2}{U_{bulk}^2} = \left[\frac{W}{W - N_T\cdot D}\right]^2$$

For Chyu's pin fin array N_T = 5. In all cases the pin fin diameters were 12.7 mm, and the total channel width was 159 mm. The following conversion factors can be reached.

$$\frac{U_{max}^2}{U_{bulk}^2} = \left[\frac{159}{159 - 5 \cdot 12.7}\right]^2 = 2.77$$

Combing the Fanning friction factor conversion, the $N\left(\frac{D_h}{L}\right)$ conversion, and the velocity conversion, the overall conversion factor becomes:

$$f_{Chyu,converted} = f_{Chyu}(0.25)(7)(0.1057)(2.77) = f_{Chyu}(0.5124)$$

Vita

Erin Nicole Elder was born on April 23, 1979 to Darryl and Nancy Elder in Rome, Georgia. Erin graduated from Rome High School in May of 1997, where she was selected as the sole recipient of the Superintendent's Award for leadership and academic excellence. The following fall she began pursuing her undergraduate degree at Georgia Tech. After her freshman year she studied at Oxford University in England through a Georgia Tech study abroad program. Erin completed five work terms at Kennedy Space Center as a co-op student where she had the opportunity to work in the shuttle operations, design engineering, and cryogenics departments. Erin participated in the National Science Foundation's Research Experience Undergraduate (REU) program in Dalian, China during the summer of 2001 where she worked to develop a theory to explain self-excited vibration in off-shore structures. During her senior year at Georgia Tech she completed undergraduate research in the Parker H. Petit Institute for Bioengineering and Bioscience testing the mechanical properties of cell constructs after vitrification as compared to more traditional cryopreservation methods. Upon graduation, Erin continued her education at Virginia Tech, pursuing a Masters in Mechanical Engineering with a focus on thermal and fluid sciences. During this time she worked as a Graduate Research Assistant in the Virginia Tech Experimental and Computational Convection Lab (VTExCCL) building a test facility to determine the cooling characteristics exhibited by a novel turbine blade cooling technology. After completion of her Masters of Science degree at Virginia Tech, Erin will be joining the Peace Corps, and is slated to leave for Kazakhstan in June of 2005.

Address: 6 Mtn. Chase Rd.
Rome, Ga 30165